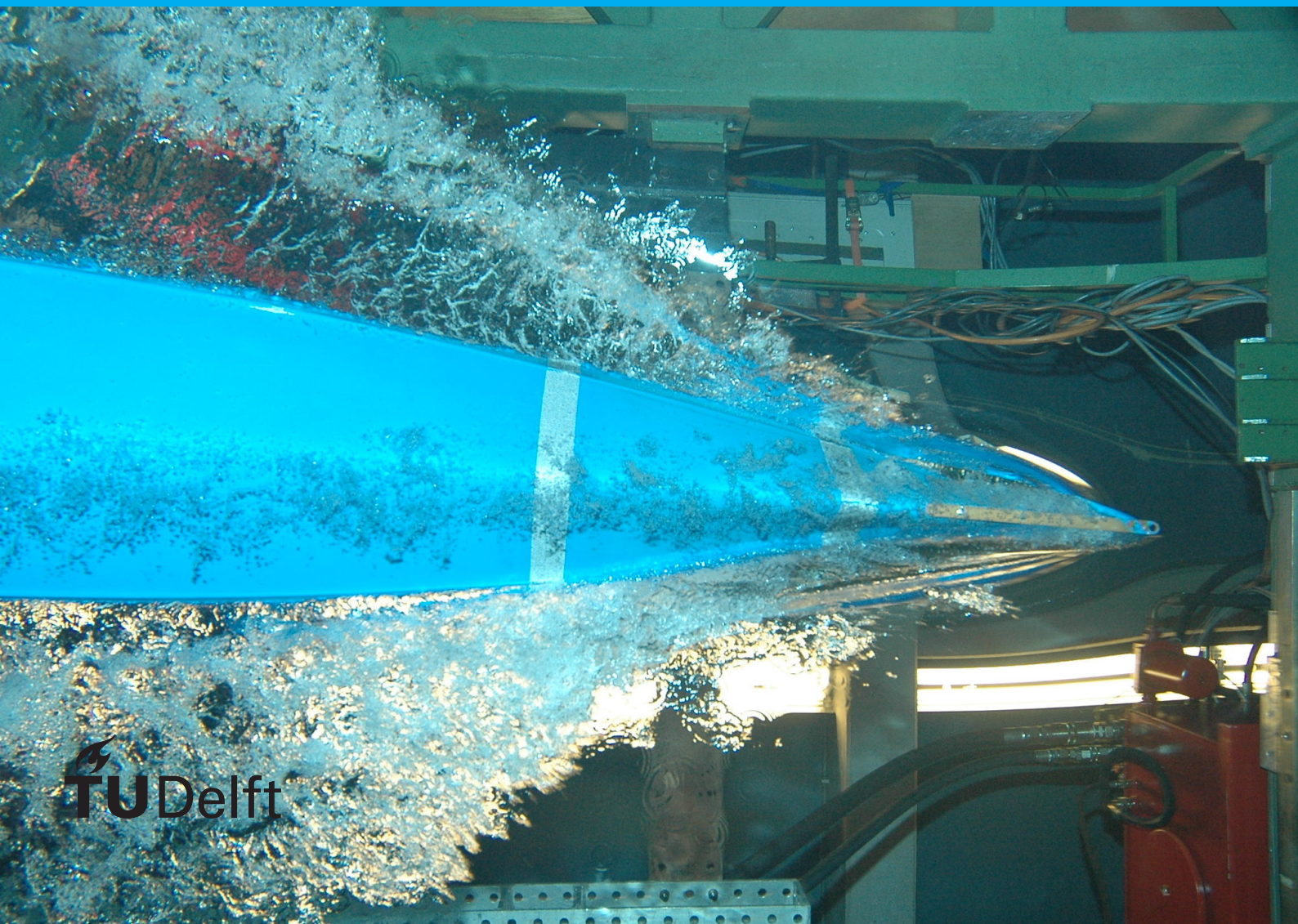


Master Thesis

Modelling and Simulation of Energy Storage System for Frequency Stability Studies

Chenrui Zhang

Technische Universiteit Delft



Master Thesis

Modelling and Simulation of Energy Storage System for Frequency Stability Studies

by

Chenrui Zhang

in partial fulfillment of the requirements for the degree of

Master of Science
in Power Engineering

at the Delft University of Technology,
to be defended publicly on August 31, 2020 at 10:00 AM.

Supervisor:	Dr.ir. Jose Rueda Torres, Dr.ir. Elyas Rakhshani, Nidarshan Veera Kumar,	TU Delft TU Delft, Hitachi ABB Power Grid Spain TU Delft
Thesis committee:	Prof.dr. Peter Palensky, Dr.ir. Jose Rueda Torres, Dr.ir. Zian Qin,	TU Delft, IEPG Group TU Delft, IEPG Group TU Delft, DCES Group

This thesis is confidential and cannot be made public until July 31, 2022.

An electronic version of this thesis is available at <http://repository.tudelft.nl/>.

Abstract

Renewable energy sources are current trend to increase power capacity considering sustainability. Wind power generator is a dominant form of renewable energy sources, However, the generation of wind power generators are stochastic, which limits the power reserve in ancillary services, like frequency regulation. Besides, power electronic interfaces are often used to connect renewable energy sources with main grid, which decouples the natural inertia of generators. The high penetration of power electronic interfaced renewable energy sources leads to a low-inertia power system, which is more vulnerable to withstand frequency disturbance.

This paper investigate the enhancement of fully decoupled wind generators by implementing ultracapacitor energy storage systems. The wind power generation can be assume constant during frequency disturbance, because wind power generators are fully decoupled by power electronic interfaces. Then, extra power supply is required to support frequency regulation. Ultracapacitors have high power density and fast reacting speed, and they can operate in server situations including fast voltage changing and a wide range of temperatures. Hence, ultracapacitors are very suitable to support fast active power-frequency responses. In order to simulate the dynamics of fast active power-frequency control in milliseconds, a detailed UC model is represented in real-time simulations. Different types of ultracapacitor models are compared to find the most suitable one to describe the fast dynamics.

Comparing with UCs, batteries have higher energy density and lower price. Hence, a battery and UC combined hybrid energy storage system is formed to complement their characteristics. Power allocation strategies are studied to achieve a fast UC power output and slower battery power output, which gives a fast active power response and protects batteries' lifetime.

Droop and derivative control and virtual synchronous power are selected strategies to control power system frequency stability. In order to find their optimal performance and fairly compare them, the best frequency performance trading off with HESS cost is found by solving an optimization problem of HESS size and controller parameters. A mean-variance mapping optimization is used to solve this non-convex, mixed-integer optimization problem. The optimization result gives the best frequency performance with minimized hybrid energy storage system cost. The power output of UCs shows how the fast active power-frequency response is enhanced by the fast UC power injection. It also explains virtual synchronous power is faster than derivative control due to lack of frequency measurements.

Contents

List of Figures	vii
List of Tables	ix
1 Introduction	1
1.1 Research Background	1
1.2 Motivation	2
1.3 Overall Objective and Research Questions	3
1.4 Literature review	4
1.5 Thesis Timetable	6
1.6 Thesis Outline	6
2 Frequency Stability Control Strategies on FDWGs	9
2.1 Objectives of Frequency Stability Control	9
2.2 Droop and Derivative Control based on Wind Turbines	11
2.3 Droop and Derivative Control based on ESS	12
2.4 Virtual Synchronous Power	12
2.5 Summary of Frequency Stability Control Strategies	14
3 UC Modelling and Implementation in RSCAD Environment	15
3.1 Dynamic Properties of UC	15
3.2 UC Modelling Methods	18
3.2.1 Equivalent electric circuit models	19
3.2.2 Fractional-order model	24
3.2.3 Summary of UC modeling methods	25
3.3 Implementing UC Model in RSCAD Environment.	27
3.4 Summary for UC Modelling and RSCAD Implementation	32
4 Application of HESS in Frequency Stability Control	33
4.1 Setting for FDWG Implemented 9 Bus IEEE System.	33
4.2 Comparison between UC and battery	35
4.2.1 Performance testament design	35
4.2.2 Comparison result between UC and battery	36
4.3 Topology of HESS	39
4.4 Power Allocation Between UC and Battery	40
4.5 Energy Storage Sizing	41
4.5.1 Power Requirements of frequency stability control	41
4.5.2 Calculation of HESS power output.	43
4.5.3 Influence of energy storage sizing.	45

4.6	Summary for Power Allocation and HESS Sizing	47
5	Mean-variance Mapping Optimization of Droop and Derivative Control and VSP	49
5.1	Formulation of the Optimization Problem	49
5.2	Mean-variance Mapping Optimization	53
5.3	Communication between MATLAB and RSCAD	57
5.4	Experimental Settings for MVMO	58
5.5	Results of MVMO for Droop and Derivative Control and VSP	61
5.6	Comparison between Optimized Droop and Derivative Control and VSP	68
6	Conclusions and Future Work	71
6.1	Conclusions for Research Questions	71
6.2	Suggestions for Future Work.	73
A	Control Loops in RSCAD	75
A.1	Droop and Derivative Controllers in RSCAD	75
A.2	VSP Controllers in RSCAD	77
A.3	RSCAD Embedded Li-ion Battery Model	77
	Bibliography	79

List of Figures

1.1	Time schedule and milestones	6
2.1	The configuration of fully decoupled wind power generator	9
2.2	Diagram of droop and derivative control	11
2.3	Diagram of droop and derivative control and cascaded controllers	12
2.4	Control diagram of virtual synchronous power	13
2.5	Diagram of phase locked loop [1]	13
3.1	Porous structure of an Ultracapacitor(inspired by [2])	16
3.2	Simple RC represented UC model	17
3.3	(a) Comparison of the terminal voltage between UC and simple RC model; (b) Charging and discharging current for testing	18
3.4	RC ladder model	19
3.5	Nyquist plot of UC impedance from EIS[2]	20
3.6	RC series-parallel model	22
3.7	RC parallel branch model	23
3.8	Fractional-order UC model	25
3.9	Four steps to create a component model in RSCAD c-builder	28
3.10	User interface of RSCAD c-builder	28
3.11	Structure of the UC storage system	29
3.12	Tab of C file associations	29
3.13	(a) RC branch circuit, (b) Norton equivalent circuit	30
3.14	Test of RC parallel model in RTDS	31
4.1	IEEE 9 bus system with 52% wind generations [3]	34
4.2	Fully decoupled wind generator with ESS connected on the DC-link	35
4.3	Frequency regulated by battery and UC under 60MW load increase	37
4.4	(a)Frequency regulated by battery under 84MW load increase, (b) Frequency regulated by UC under 84MW load increase.	37
4.5	UC SOC during frequency regulation	38
4.6	(a)UC inner voltages during frequency regulation, (b) UC inner voltages in long term.	38
4.7	(a)Passive topology, (b) semi-active topology, and (c) fully-active topology of HESS.	39
4.8	Power allocation of droop and derivative control	40
4.9	Power allocation of VSP	41
4.10	Buck-boost converter connecting HESS with DC-link	43
4.11	Maximum output power of UC changing with duty cycles (Continuous mode)	45

4.12 (a) Maximum output power, (b) duty cycle at the maximum power point and (c) efficiency at the maximum power point changing with the size of UC.	45
4.13 (a) Maximum output power, (b) duty cycle at the maximum power point and (c) efficiency at the maximum power point changing with the size of UC, when efficiency is required higher than 90%.	46
5.1 (a) Battery current, (b) frequency component analysis of battery current.	52
5.2 The flowchart for the MVMO algorithm procedures	54
5.3 Flowchart for optimization between MATLAB and RTDS	57
5.4 Normalized fitness value and objective function value of droop and derivative control	61
5.5 Normalized optimization variables of droop and derivative control	62
5.7 Normalized optimization variables of VSP	62
5.6 Normalized fitness value and objective function value of VSP	63
5.8 Comparison of frequency performance of droop and derivative control before and after optimization	63
5.9 Comparison of power output of droop and derivative control before and after optimization	65
5.10 Comparison of frequency performance of VSP before and after optimization	66
5.11 Comparison of power output of VSP before and after optimization	66
5.12 (a) Battery current of VSP before optimization, (b) frequency component analysis of corresponding battery current.	67
5.13 (a) Battery current of VSP after optimization, (b) frequency component analysis of corresponding battery current.	68
5.14 Comparison between optimized frequency performance of droop and derivative control and VSP	69
5.15 Total power output of droop and derivative control and VSP	69
5.16 Battery and UC power output of droop and derivative control and VSP	70
A.1 (a) Droop and derivative controller, (b) Outer power controller, (c) Inner current controller.	76
A.2 VSP controllers in RSCAD	77
A.3 RSCAD embedded Li-ion battery model [4]	77

List of Tables

2.1	The summary of frequency control methods	14
3.1	Qualitative comparison between UC models	26
3.2	Estimated parameters of RC parallel branch model	31
4.1	Power flows in IEEE 9 bus system	34
4.2	Size selection of battery and UC	36
4.3	Result of battery and UC comparison	37
4.4	Inertia of the modified IEEE 9 bus system without frequency control	42
5.1	MVMO parameter values	60
5.2	Upper and lower limits of optimization variables (droop and derivative control)	60
5.3	Upper and lower limits of optimization variables (VSP)	60
5.4	Optimal solution (droop and derivative control)	62
5.5	Optimal solution (VSP)	63
5.6	Comparison of droop and derivative control results	64
5.7	Comparison of VSP control results	65

List of Abbreviations

CPE	Constant Phase Element
DFIG	Doubly Fed Induction Generator
EIS	Electrical Impedance Spectroscopy
EMT	Electromagnetic Transient
ESR	Equivalent Series Resistance
ESS	Energy Storage System
FDWG	Fully Decoupled Wind Power Generator
GSC	Grid Side Converter
HESS	Hybrid Energy Storage System
HVDC	High Voltage Direct Current
LF	Loop Filter
LMSR	Least Mean Square Error
PD	Phase Detector
PLL	Phase Locked Loop
RES	Renewable Energy Source
RMSE	Root Mean Square Error
ROCOF	Rate of Change of Frequency
RSC	Rotor Side Converter
RTDS	Real-time Digital Simulation
UC	Ultracapacitor
VCO	Voltage-controlled Oscillator
VSC	Voltage-source Converters
VSP	Virtual Synchronous Power
WTG	Wind Turbine Generator

Introduction

1.1. Research Background

Power system stability, security and reliability is significantly affected by its frequency. Traditionally, frequency stability of power system is supported by the inertia response of conventional synchronous generators. In the time scale of power system frequency stability, system inertia reacts immediately by releasing the reserved kinetic energy in rotating masses, which mitigates the rate of frequency variation. Primary frequency control balances the active power of loads by automatically regulating the valves of prime mover or increasing the generation of electrical energy sources. The secondary control is activated afterwards to recover the system frequency to nominal value. The tertiary control regains the reserve of generators and economic dispatch. Insufficient active power-frequency response will result in unstable conditions and harm the security operation of power system.

Nowadays, considering the sustainability and increasing electrical demands, the constitution of energy sources in power system is changing with a trend of more renewable energy sources (RES) including solar panels, wind turbine generators(WTG), etc. Solar panels are stationary thus no inertia is available. WTGs are rotating machines but the available inertia is quite limited due to the unpredictable wind speed and the control strategy of maximum power extraction. In addition, power electronic interfaces can decouple the synchronous sources with main grid. Because of these facts, the natural inertia of energy sources is reduced in power system, leading to a low frequency stability against disturbance[5]. When a generation outage or a large load connection happens in power system, the system frequency will drop due to the imbalance between supplies and demands. At this time, frequency stability controllers should operate to balance the power demand and restore the nominal frequency. However, the reduction of system inertia will cause severer frequency drops which may exceed the frequency limits, and the frequency settling time may be longer. Therefore, additional methodologies are required to overcome these emerging challenges on frequency stability.

1.2. Motivation

In this thesis, a power system with fully decoupled wind power generators (FDWG) is considered, which means no direct connection exists between WTG and power grid, and no inertia from WTG is available to support system frequency. In this configuration, control algorithms can be applied on the power electronic converters of a wind turbine to extract extra kinetic energy to the grid by slowing down its rotating speed. However, excessive extraction may impose severe threat to the WTG leading to a rotor speed lower than the operational limits or even stall[6]. Besides, during normal operations, a WTG is often tuned to generate a maximum amount of power considering economic effect, so the kinetic reserve is trivial to regulate the system frequency[7]. The kinetic inertia of WTG is also determined by the intermittent wind speed. As a conclusion, WTGs are insufficient and uneconomic to support power system inertia.

Considering the fact that FDWGs are suffering from the lack of power reserve, a better objective to apply virtual inertia is energy storage systems (ESS). Currently, ESS has applications in power shift, supplying capacity, voltage support, electric vehicles, etc[8]. The categories of ESS can be selected depending on the power and energy demand of applications. When a frequency disturbance happens, the systems inertia first release the dynamic energy of rotating mass in seconds. Afterwards, the primary frequency control starts to restore the power equilibrium. The secondary control will recover the frequency to the nominal value in minutes. As a result, if ESS is adopted as a solution for frequency control, it should be able to quickly release a peak amplitude of power in a few second, and provide a bulk amount of energy subsequently.

According to the explained requirements for ESS in frequency control, batteries are frequently used as flexible energy sources. Batteries have enough energy capacity to accomplish missions like charging plan rescheduling, and also have an acceptable speed to regulate power wave forms. On the other hand, ultracapacitors (UC) have complementary properties to batteries. It can withstand a broader temperature range and more frequent charging/discharging. Moreover, an UC has a relatively higher power rate comparing with other types of storage devices, thus it can achieve a fast active power-frequency response and mitigate the rate of frequency variation. Although its significant capacitance can contain more electrical energy than normal capacitors, the fully discharging of UC is still too fast for the whole process of frequency regulation. Consequently, a hybrid energy storage system (HESS) combined with UCs and batteries is proposed in this thesis as the energy sources for frequency control. In order to evaluate the improvement with HESS, the performance will be compared with active-power frequency response based on WTG and only batteries.

Considering the different time scales of frequency stability control, virtual inertia and other advanced frequency control methods should be selected to fit the characteristic of HESS. The target of frequency controller is the power electronic interface of HESS. The frequency controllers can manipulate these DC/AC converters to response to the frequency deviations or rate of change of frequencies (ROCOF). Therefore, the ROCOF, frequency nadir and settling time can be improved to satisfy the restriction of power system. Although the frequency stability of the power system can be controlled as our expectation, the detailed information inside a HESS is still not known.

The methods for improving system inertia and frequency controllers have been well studied in previous references [1, 5–7, 9–13], including derivative and droop control, fuzzy control, model predictive control, etc. However, the scope of these researches is concentrate on performance of frequency controllers and gives a compromise on the fidelity of models, where the HESS is assumed as a simple

energy source or ideal circuit elements. For instance, the dynamic performance of UC is nonlinear due to its physical structure[2], but the UC is often assumed as a simple RC series circuit to simplify calculations. These assumptions are acceptable to explain the principle of frequency control, but the ignored phenomenons of HESS can be inaccurate in dynamic behaviour and long-term storage. The low resolution model will finally decrease the fidelity of an electromagnetic transients (EMT) simulation and gives an untrustworthy conclusion. So the detailed model of HESS is proposed in this thesis.

In order to achieve the optimal performance of HESS, the power allocation between batteries and UCs should be defined explicitly. The manufacture restricts the charging and discharging times and current magnitudes of a battery. Therefore, protecting a battery from high-frequency current can extend its lifetime[14]. In contrast, UC has a small time constant and is able to withstand frequently charging and discharging, which is more suitable to supply the high-frequency component of power demand. In order to separate the power reference, HESS allocation methods are going to be evaluated according to the dynamic performance of HESS.

1.3. Overall Objective and Research Questions

The overall objective of this thesis is to enhance the fast active power – frequency control of a fully decoupled wind power generator by using UC based HESSs. To achieve this goal, the UC model and control algorithm are implemented in a power system with a large share of RES, and the performance assessment is conducted in real-time digital simulations (RTDS). An optimization about frequency stability control and HESS sizing is formulated to search for the optimal solution and best performance.

The research questions and solutions are listed below:

1. What are the dynamic properties of an UC that should be taken into account for EMT modeling and simulation of interconnected power system?
 - The UC principles are studied to find the dynamic behaviours which are most relevant to the application of frequency stability control. The dynamic properties should be selected by trading off between fidelity and feasibility.
2. How can a generic UC model be designed in RTDS environment based on the capabilities of RSCAD?
 - Considering the UC dynamics, generic UC models are studied. Based on the principles of UC modeling, a self-defined UC model is created in RSCAD environment. The technology of RSCAD component should be studied.
3. Up to which extent can the fast active power-frequency control of a FDWG be enhanced by adding an UC in its DC link?
 - The performance of FDWG with/without UCs will be tested. The performance of different control approaches (droop control, droop-derivative control and virtual synchronous generator) are compared. The optimal solution of controller and power system setting is analyzed and solved in an optimization problem.

1.4. Literature review

Many categories of frequency control methods have been implemented in different applications. The principles of these frequency stability control strategies can be summarized as four aspects: droop and derivative control, virtual synchronous generator, virtual synchronous power (VSP) and other frequency control methods.

The working domain of derivative and droop control is to supply inertia response and primary control. Therefore, the frequency variation and its derivative will be input as control variables to calculate the required power reference. A typical design is expressed in [7], where a virtual inertia and droop control based frequency controller is implemented to calculate the required amount of power, and then the power reference will be delivered to a cascaded power controller. The power controller will calculate the current reference for inner current control loop, and finally, the output power of HESS will be determined by regulating the modulation index of power electronic converters. By means of supplying a determined amount of power, HESS can support system frequency and maintain it above a certain limit value. When a load mismatch happens, the derivative of frequency is rather large before the frequency variation influences the system. The virtual inertia releases a peak amount of power, until droop control settles system frequency at a new equilibrium point. Thresholds for frequency controller activation and deactivation are assigned in order to avoid small signal disturbance and excessive power output. The simulation result shows that frequency nadir is still above the system frequency limit even in severest case, and the ROCOF is also mitigated.

The small signal stability of derivative and droop based frequency control is discussed in [15]. The closed loop transfer function is written as $\delta f = -\frac{G_{MG}(s)}{1+G_{MG}(s)G_{BESS}(s)}$, where $G_{MG}(s)$ is equivalent transfer function of microgrid; $G_{BESS}(s)$ is the open loop transfer function of battery energy storage system. The $G_{MG}(s)$ can be represented by the swing equation and primary control as $G_{MG}(s) = \frac{\frac{1}{Ms+D}}{\left(\frac{-\lambda MG}{T_R s+1}\right)}$, where M is inertia constant; D is damping ratio; term $\frac{-\lambda MG}{T_R s+1}$ is transfer function of primary control. Since $\Delta P_{BESS} = G_{BESS}(s)\Delta f$ is the response of BESS, the transfer function of $G_{BESS}(s)$ can be composed as $G_{BESS}(s) = G_{PLL}(s) \cdot G_f(s) \cdot G_{FC}(s)$ where G_{PLL} represents phase locked loop (PLL) which measures system frequency; $G_f(s)$ is low-pass filter cancelling the high-frequency noise of frequency derivative; $G_{FC}(s) = (k_{droop_control} + k_{virtual_inertia} \cdot s)$ is the frequency controller. The corresponding pole loci and Bode plot shows the dynamic performance of controllers, and the controller parameters can be tuned to mitigate small signal disturbance. It is worth mentioning that the dynamics of inner current controller is faster enough to be negligible, same for generator and exciter transient.

As the control signal is extracted from frequency, the influence of frequency measurement should be taken into account. A comparison between system dynamic performance with and without PLL is analyzed in [1], where a regional inertia emulation with high-voltage-direct-current (HVDC) connection is given. A supplementary power modulation controller is used to calculate the dynamic behaviour of HVDC link. After representing the state space, the dynamic effects of derivative controller gain and PLL are analyzed. By calculating the participation factors of system modes and comparing eigen trajectories of various conditions, the superiority of derivative control is proved. It has been proved the PLL increases oscillations in control system.

As a conclusion, this type of control method may have different forms of controllers, but the common characteristic is the measurement of frequency and working as equivalent current sources, where the voltage-source converters (VSC) are grid-supporting topology. The phasor measurement unit may

impose negative impact on the system stability.

The principle of virtual synchronous generator is emulating dynamic performance of synchronous generators. In some cases, the dynamic of synchronous generator is simplified as only the swing equation. A general design of virtual synchronous generator is interpreted in [11] based on the swing equation, which is represented as a control block in frequency controllers to calculate the required amount of active power for frequency regulations. Frequency stability will be supported by controlling power angle of the terminal voltage of the virtual synchronous generator. In this case, UCs are directly connected to the DC bus. Since UCs releasing power will decrease the DC bus voltage, a DC/DC converter connected battery stack is used to maintain the DC bus voltage. As a conclusion, the VSC works in a grid-forming topology, and virtual synchronous generator is equivalent to a voltage source.

The typical characteristic of VSP is that it does not need a PLL for frequency measurements for inertia emulation controllers. Instead the power difference of converter output and power flow is input to inertia emulation controllers. Thereby, the disturbance and delay of PLL is avoided. An application of virtual synchronous power in frequency control of multiple regions is illustrated in [13]. The frequency reference and phase angle is calculated by the power difference of supply and demand rather than from phasor measurement units. The corresponding control loop represents the mechanical behavior of a synchronous generator, and it can simulate the frequency change under a given lack of power supply. By regulating the inertia factor of the power loop controller, the control system can supply the required active power-frequency response. A virtual admittance is used to determine the amount of transferred power P_{out} . As the phase angle δ is relatively small, it can be directly multiplied instead of $\sin\delta$. Therefore, the terminal voltage of ESS will be measured as a control variable.

Other frequency control methods share the similar principles with previous methods. Some variations are made to cope with specific applications. A PLL Embedded Frequency Control is presented in [12]. Instead of using a separate frequency controller, the swing equation is implemented in a PLL by tuning the inner phase detector and loop filter, i.e. the multiplication of their parameters is equal to virtual inertia. The transmission equation is used to calculate the required active power. [6] gives a UC coupled doubly fed induction generator (DFIG) control method without calculation of frequency derivative. The UCs are directly connected on the DC-link of DFIG, and the output power is controlled by regulating the voltage of DC-link which is determined only by frequency. Therefore, the frequency derivative is avoided.

In previous ESS studies, UCs are usually modelled as an ideal capacitor in series with an equivalent series resistance (ESR), e.g. in literature [16], [17], [18], and [19]. The reason for selecting this model is to simplify calculations. However, this simplified model is not accurate enough in real-time simulations of this thesis. Many detailed models have been derived to improve the accuracy. Among them, equivalent electric circuits and fractional calculus based models are discussed in this thesis. The general structure of equivalent electric circuit models can be concluded as RC parallel branch, RC ladder and RC series-parallel branch. A possible way of topology conversion is proposed in [20]. [21] where the accuracy of RC parallel model is improved by inserting a variable capacitor in parallel with the fast-term capacitor. A least mean square error (LMSE) method is proposed to identify the model parameters. The result of LMSE is evaluated by comparing with the real value of previous simulations with an error less than 2%.

As reported in [22], a three-order RC ladder model is adopted to simulate UC terminal voltage under different current profiles. The corresponding three-order transfer function is used to represent the RC

ladder model. The error of UC terminal voltage is used to validate this model. First, the UC model is charged to different voltages step by step, and the error of terminal voltage is less than 0.05V. In second test UC is fully charged from empty resulting a maximum -0.1V error. In [2] a curve-fitting program is used to determine the impedance versus voltage equations. An Electrical impedance spectroscopy (EIS) is used to provide the parameter information. However, the simulated waveform still has amplitude difference from experimental results. The reason is UC model is developed based on static performance of different voltages, but in real situation ions require a finite time to move into pores of electrodes, and the actual capacitance could be smaller. In order to adjust capacitance to an adequate value, phenomenons under various charging currents are derived in PSCAD simulations. The modified model is proved to have smaller errors than previous models. [23] proposed a better solution to fit the data from EIS. Weighting constants are involved in the linear least square calculations, because EIS contains more high frequency information than low frequency part. As a result, higher weighting constants on low frequency data can improve the fitting accuracy on low frequency in trade of the high frequency accuracy.

1.5. Thesis Timetable

The schedule and milestones of this thesis is conclude in Figure 1.1.

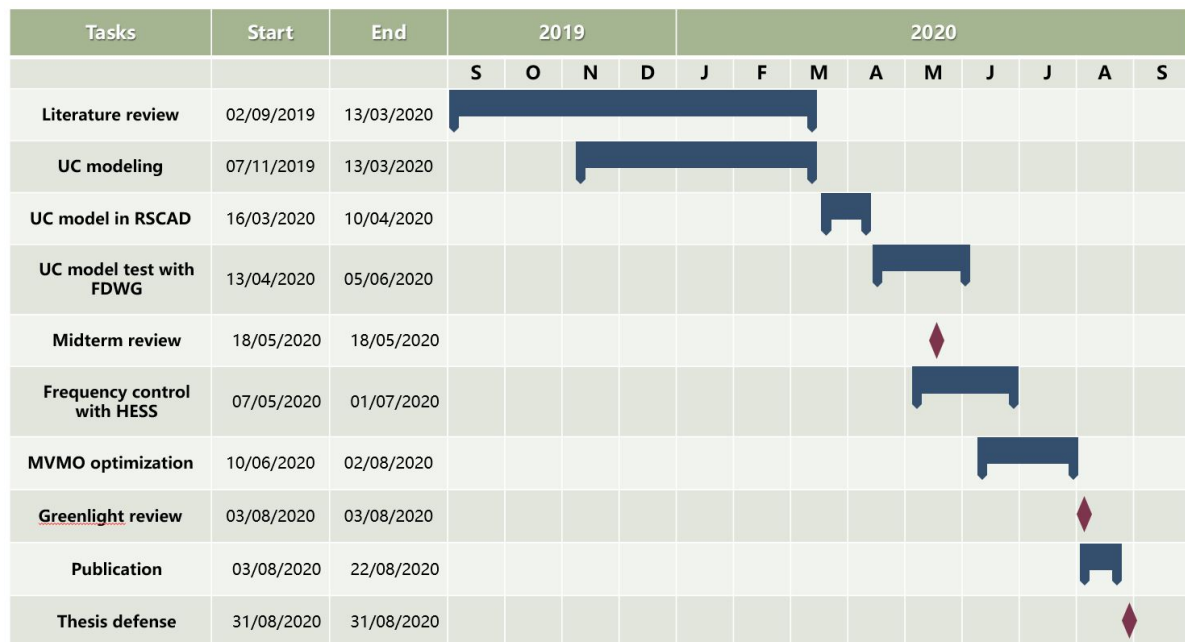


Figure 1.1: Time schedule and milestones

1.6. Thesis Outline

Chapter 1: Introduction

This chapter explains the motivation and background of this thesis. Then the overall objective is analyzed into 3 research questions. The corresponding solutions are the main work of this thesis. In literature review, results of previous researches are given as the reference of this thesis. The thesis timetable is given based on research milestones. Finally, the thesis outline introduces the sequence

and main contents of this thesis.

Chapter 2: Frequency Stability Control Strategies on FDWGs

Chapter 2 explains the methods to enhance the power-frequency response of a FDWG. It starts from analyzing the requirements of power system frequency stability, which leads to the droop and derivative control. Afterwards, energy storage system is proposed as a better energy source for the droop and derivative control. Virtual synchronous power is also implemented on FDWGs. UCs are considered as better power sources to supply the fast power response of VSP.

Chapter 3: UC Modelling and Implementation in RSCAD Environment

The principles of UCs are explained at the beginning of this chapter, which leads to the UC dynamic properties related with fast active power response. Generic UC models are discussed and compared to find the most suitable one in this thesis. Afterwards, the selected UC model is implemented in RSCAD environment. The technology of RSCAD c-builder is explained.

Chapter 4: Application of HESS in Frequency Stability Control

This chapter introduces the experimental power system at the beginning. Frequency behaviours are illustrated according to power flows of this system. Frequency control performance of UCs is compared with batteries to prove the advantages of UCs. Then a battery and UC combined HESS is proposed as a better solution. Actual concerns about HESS applications including HESS topology and power allocation methods are considered. Finally, the influence and rules of ESS sizing is discussed.

Chapter 5: Mean-variance Mapping Optimization of Droop and Derivative Control and Virtual Synchronous Power

According to the frequency stability control requirements and rules of HESS sizing, an optimization problem is formulated. In order to solve this non-convex, mixed-integer problem, a MVMO algorithm is used to find the optimal solution. The principles of MVMO is explained. Communication channels are established between MATLAB and RSCAD to transfer offspring variables and simulation results. The specific parameter settings are discussed according to the application of frequency stability control. The optimization result is analyzed and compared with the performance before optimization. The optimal results of droop and derivative control and VSP are compared to summarize their characteristics.

Chapter 6: Conclusions and Future Work

The conclusions from previous chapters and research questions are summarized here. The possible improvements in future work is also illustrated here.

2

Frequency Stability Control Strategies on FDWGs

In this thesis, the fully decoupled wind power generators (FDWG) are considered as one case in low-inertia power systems. Although a wind turbine contains a rotating mass, it is decoupled with the main grid by the power electronic interface. The configuration of a FDWG is shown in figure 2.1. The rotor-side converter (RSC) is controlled to output the maximum power generated by the wind turbine. The grid-side converter (GSC) is controlled by a voltage controller to keep DC-link voltage constant. When the main grid is suffered from frequency disturbance, the rotating speed of wind generators are not influenced due to the setting of power electronic converters. As a result, FDWGs cannot directly support system frequency, and a power system dominated by FDWGs is vulnerable to withstand frequency disturbance. Extra control methods are required to supply frequency response.

In this chapter, we are going to explain the objectives of frequency control, and discuss several possible methods to implement frequency control including wind turbine based droop and derivative control, virtual synchronous power and ESS based droop and derivative control.

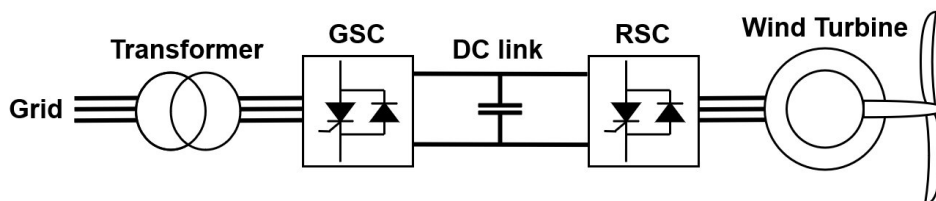


Figure 2.1: The configuration of fully decoupled wind power generator

2.1. Objectives of Frequency Stability Control

Conventionally, power system frequency is maintained 50HZ by the rotating speed of synchronous generators. Theoretically, the synchronous speed should remain constant to ensure the healthy operation of power system. However, the rotating speed of generators are impacted by power flows and disturbance. This phenomenon is described by the swing equation 2.1.

$$\frac{2H}{w_s} \cdot \frac{dw}{dt} = \frac{P_m - P_e}{S_b} \quad (2.1)$$

H is defined as an inertia constant with second as unit; w_s is the synchronous speed of power system; $\frac{dw}{dt}$ is the rate of change of rotating speed. The right side is the power balance of a generator, where P_m is the input mechanical power from the prime mover; P_e is the output electrical power to the grid; S_b is the nominal power of a generator to transfer the power into a per unit value. This formula describes how the rotating speed of generator changes with power disturbance. For example, w will decrease when a load increase leading to an increase of output electrical power P_e . The reason is that a synchronous generator fills the power gap by losing kinetic energy stored in the rotating mass. The inertia constant H is determined by the size of rotating mass, which is used to describe the changing rate of w . When inertia H is larger, the changing speed of w is slower, and hence the power system is more stable.

Since synchronous generators connected with the power system contribute their power generation to the grid, when disturbance happens, their rotating speeds are all going to be influenced. Therefore, frequency is seen as a global property in power system, which means that all synchronous generators are influenced by the same extent of synchronous speed changing. Hence, the swing equation 2.1 can be rewrote as equation 2.2 to represent the derivative of system frequency. According to the swing equation, the rate-of-change-of-frequency (ROCOF) is defined in equation 2.3 as the maximum frequency gradient which is often observed around 0.5s after load disturbance[1].

$$\frac{2H_{sys}}{F_s} \cdot \frac{df}{dt} = \frac{P_m - P_e}{S_b} \quad (2.2)$$

$$H_{sys} = \frac{S_{G1}}{S_b} H_{G1} + \frac{S_{G2}}{S_b} H_{G2} + \dots + \frac{S_{Gn}}{S_b} H_{Gn}$$

$$ROCOF = \max\left(\frac{df}{dt}\right) = \max\left(\frac{P_m - P_e}{S_b} \cdot \frac{F_s}{2H_{sys}}\right) \quad (2.3)$$

The system inertia consists of the inertia of n connected generators H_{G1}, \dots, H_{Gn} . The contribution of each generator is determined by its rated power S_{G1}, \dots, S_{Gn} . Therefore, decoupling the natural inertia of wind turbines will lead to a low inertia in the whole power system. When loads and generations are imbalanced, the ROCOF is larger in a low-inertia system. As a result, system frequency is easier to exceed the limits of frequency and impose great threats to system frequency stability. Therefore, extra power support are needed when power imbalance happens.

Primary frequency control stabilizes system frequency at a new stable state, which is traditionally achieved by the speed governors mounted at the generators. Since the system frequency is decoupled with the wind generators, speed governors are not useful to supply primary frequency control. As a summary, the frequency stability control at the FDWGs are required to not only migrate the ROCOF but also stabilize system frequency at a new state.

The objective of frequency control is to stabilize system frequency against disturbance by supplying inertia response and balancing the power difference. When a load mismatch happens, the derivative of frequency increases very fast before the frequency variation influences the system. Frequency drop with higher ROCOF can approach the admissible frequency faster and impose danger to the power

system. When power balance is recovered, system frequency is stabilized at a new value which should be higher than the admissible frequency. During this period, the minimum post-contingency frequency is defined as frequency nadir f_{nadir} in equation 2.4. This value is also a critical point of frequency stability control.

$$f_{nadir} = \min(f) \quad (2.4)$$

2.2. Droop and Derivative Control based on Wind Turbines

As discussed in the objective of frequency stability control, the two control targets are the ROCOF and frequency nadir f_{nadir} . One solution is derived as derivative and droop control, which inputs frequency derivative df/dt and frequency deviation Δf as control signals. The block diagram figure 2.2 shows the configuration of droop and derivative control, where the output power reference can be represented as below.

$$P_{ref.droop} = \frac{1}{R} \Delta f \quad (2.5)$$

$$P_{ref.derivative} = \frac{2H}{F_s} \cdot \frac{df}{dt} \cdot S_b$$

The power reference of droop control $P_{ref.droop}$ is proportional to the frequency deviation Δf . When power output of droop control equals to the shortage of load power, the frequency deviation Δf does not increase anymore. The power reference of derivative control $P_{ref.derivative}$ comes from the swing equation 2.1. More power output is required to simulate virtual inertia when frequency is changing faster.

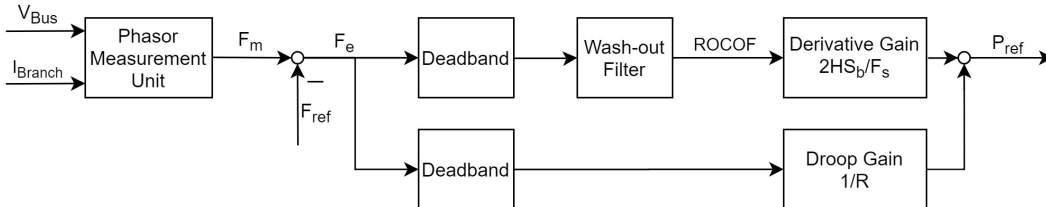


Figure 2.2: Diagram of droop and derivative control

The frequency reference is set as the nominal frequency 50HZ. Δf is the frequency deviation from frequency reference. The ROCOF is calculated through a wash-out filter with a very high cut-off frequency which is used to replace the derivative block in RSCAD environment.

The calculated power reference is input to the rotor-side converter of a FDWG. Since extra power is supplied by the wind generator during frequency drop, it operates similar like a synchronous generator with inertia response and primary control. In this case the power source is wind generator itself. Since a wind turbine is also a rotating mass, it is also possible to draw extra power by increasing the power reference of rotor-side converter. However, in reality, there is not power reserve in a wind turbine especially when the rotor-side converter is controlled to deliver maximum power generation from a wind generator.

2.3. Droop and Derivative Control based on ESS

The other possible power resource is a separate ESS. In this thesis, a battery and UC combined HESS is considered connecting on the DC-link of a FDWG. A buck-boost converter is used to control the power transfer between DC-link and the HESS. In normal conditions, the ESS is put into silence. When frequency disturbance happens in the main grid, the HESS is controlled to supply extra power, which will increase the voltage of DC-link. As the grid-side converter is set to remain DC-link voltage constant, extra power will also be delivered to the main grid and help to control the system frequency stability.

Comparing with wind generators, ESSs have larger energy capacity to supply for frequency stability control. In general, the setting for rotor-side converter is to output the maximum generation of a wind generator. Therefore, there is a limited power reserve stored in a wind generator. Besides, it is uneconomic to change the setting for wind generators, because it will reduce the efficiency.

The controller structure for ESS based droop and derivative control is shown in figure 2.3. An outer power controller and an inner current controller is used to generate duty cycle to control the buck-boost converters. The power reference is also generated as equation 2.5. The input signal for power controller comes from the power error P_e . The actual power output P_m and current I_m are measure at the terminal of the ESS. The current reference for current controller is generated from the power controller. During the operation of HESS, the DC converter is basically working in buck mode, because the DC-link voltage is 4kV which is normally higher than the ESS voltage. In contrast, ESS is charged in boost mode.

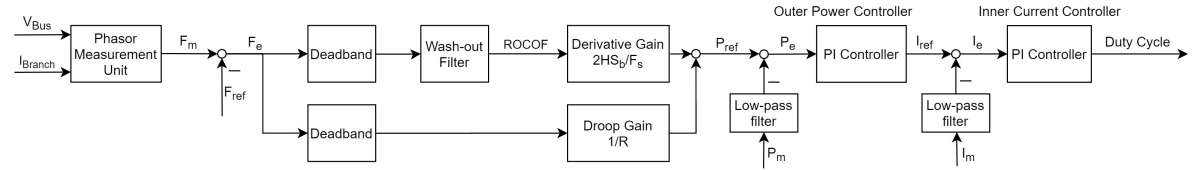


Figure 2.3: Diagram of droop and derivative control and cascaded controllers

The measured frequency value comes from phasor measurement units, hence the influence of frequency measurement should be taken into account. A comparison between system dynamic performance with and without PLL is analyzed in [1], where a regional inertia emulation with HVDC connection is given. A supplementary power modulation controller is used to calculate the dynamic behaviour of HVDC link. After the state space is represented, the dynamic effects of derivative controller gain and PLL are analyzed. By calculating the participation factors of system modes and comparing eigen trajectories of various conditions, the superiority of derivative control is proved. It has been proved the PLL increases oscillations in control system, which is a disadvantage of droop and derivative control.

2.4. Virtual Synchronous Power

The virtual synchronous power (VSP) is proposed under some special conditions where power flows have strong relations with power system frequency. For example, one load increase leading to rising of power flows shared by synchronous generators, and this load is also supplied by RESs. When power measurements detect that the power flow from synchronous generators is rising and RESs output is remaining same, this power difference is used as a signal of frequency drop according to the swing equation 2.1. This phenomenon inspires the idea of VSP. When a VSP is installed on a RES, the

difference of power flows motivate the RES to generate more power output, which is helpful to stabilize the power system frequency. The power reference of VSP is defined as equation 2.6, where P_{RES} is power generation from a wind generator; P_{Bus} is the power flow delivered from the bus of the FDWG.

$$P_{ref.VSP} = P_{Bus} - P_{RES} \quad (2.6)$$

The control diagram of VSP is shown in figure 2.4. A second-order control loop is used to generate the duty cycle for DC-DC converters, where ω_n is natural frequency and damping factor ζ . The power reference comes from the power difference. Considering a simple case of VSP application, where FDWGs are connected on the same bus with synchronous generators, the power output of the common bus is the sum of total power generation. Then during disturbance of load increase, active power is drawn from synchronous generators, and meanwhile the generation of FDWGs remain constant. Due to the different power responses at FDWGs and synchronous generators, the input signal of VSP controller is not zero anymore. The power reference will force RES to increase output power and balance the power difference. The power increase is not taken from wind generators but from ESSs. The duty cycle controls the operation of interfaced power electronic converters.

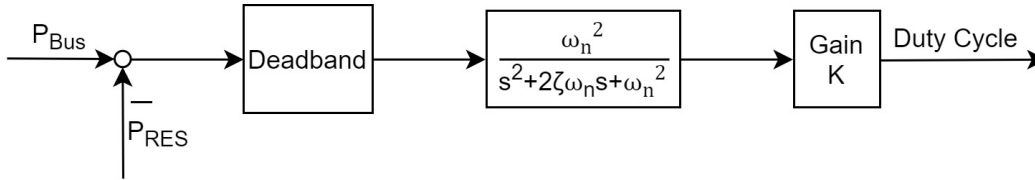


Figure 2.4: Control diagram of virtual synchronous power

Comparing with droop and derivative control, VSP does not need frequency measurements. This advantage avoids the delay and instability of phasor measurement units, and increase the reacting speed of frequency controllers. The diagram of phase locked loop (PLL) is shown in figure 2.5. It is composed by phase detector (PD), loop filter (LF) and voltage-controlled oscillator (VCO). The measured frequency comes from the output of PLL. When system frequency changes, the angle difference still requires a time delay to be measured at the terminal of output, which slows down the reacting speed of frequency control. Instead of measuring the frequency, VSP measures the power values which changes immediately when frequency starts to change.

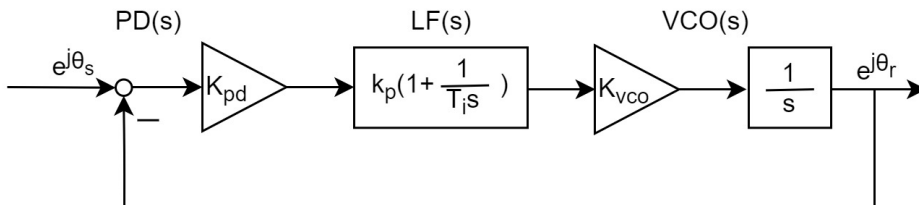


Figure 2.5: Diagram of phase locked loop [1]

However, in our study there is a constraint on VSP applications. The load variation influences the power flow at the bus of RES. It is an ideal situation to have a RES and synchronous generator connected on a common bus. More general situation is that RESs and synchronous generators connected

at different locations are sharing the same loads. In that situation, the relationships of their power flows can be calculated. Therefore, VSP controllers need to be designed according to actual power flow distributions at different locations. In contrast, frequency is a global value, and location does not influence droop and derivative controllers.

As a conclusion, VSP normally has a faster response than droop and derivative control especially at the beginning moment. However, for batteries, the reacting speed is still delayed by slowly building up the inductive current. In contrast, an UC has a very low time constant, and using UCs as energy sources can better fit the characteristic of VSP. The high power density and fast releasing speed of UC is necessary to achieve the optimal performance of VSP.

2.5. Summary of Frequency Stability Control Strategies

This chapter introduces two suitable frequency control methods on FDWGs, droop and derivative control and VSP. The characteristics of droop and derivative control and VSP are summarized in table 2.1. Among them, droop and derivative control can achieve a better performance with ESSs. Implementing UCs can further improve the speed of frequency stability control especially for VSP with a fast reacting speed .

In order to improve the performance of frequency stability control, next chapter introduces the characteristics of UCs, and implements UC models to build a HESS.

Table 2.1: The summary of frequency control methods

Frequency Control Methods	Properties
Derivative and Droop Control	<p>Control signal: Measured frequency and its derivative;</p> <p>Physical meaning: System inertia and primary control support;</p> <p>Controller structure: Cascaded PI controllers;</p> <p>Advantages/dis.: 1. Frequency measurement and frequency derivative required, which causes time delay and oscillations in control loops;</p> <p>2. Frequency is globally effective control signal for frequency control at different locations.</p>
Virtual Synchronous Power	<p>Control signal: Power difference between RES generation and changes of power flow;</p> <p>Physical meaning: Power mismatch support for frequency stability is supplied;</p> <p>Controller structure: Controllers are second-order systems;</p> <p>Advantages/dis.: 1. Control signal is faster because frequency measurement is not required;</p> <p>2. The difference of power flow is a location dependent value, and hence the output of VSP is also different at locations.</p>

3

UC Modelling and Implementation in RSCAD Environment

This chapter first illustrates the principles of UCs. Some dynamic properties of UCs are considered to build detail models in RSCAD environment. The UC modeling methods in reference are discussed and compared to find a most suitable one as the ESS for the study of fast active power-frequency control. The details of building a UC model in RSCAD environment is also explained.

Finally, the accuracy and power ramp-rate of these models are compared, and the most suitable UC model for RTDS simulations is selected.

3.1. Dynamic Properties of UC

A typical UC structure is formed by two porous electrodes, inner electrolyte and two current collectors. When external energy sources charge the UC, current collectors help to accumulate positive and negative charges on the two electrodes. Figure 3.1 shows the inner look of a charged UC. The electrolyte is filled between the two electrodes. Therefore, the cations and anions in electrolyte are attracted by the charged electrodes. Normally, the electrodes are made of carbon with numerous pores. The attracted cations and anions distributed in the porous electrodes forming the electric potential. In contrast, a normal parallel plate capacitor has a non-conducting material like air between two electrodes. The charges are only distributed on the surface of the parallel electrodes, and the strength of electric field depends on the dielectric strength. The general capacitance calculation is shown in equation 3.1, where ϵ_0 is the permittivity constant; A is the total area of electrodes including the area inside porous structures; d is the distance of electric field. Comparing with parallel plate capacitors, UCs have a significantly improved the electrodes' area to $1000-2000m^2/cm^3$ [2]. Besides, the electric field is formed between charges in porous electrodes and ions, so the small distance of electric field also increases the capacitance of UC.

$$C = \frac{\epsilon_0 \cdot A}{d} \quad (3.1)$$

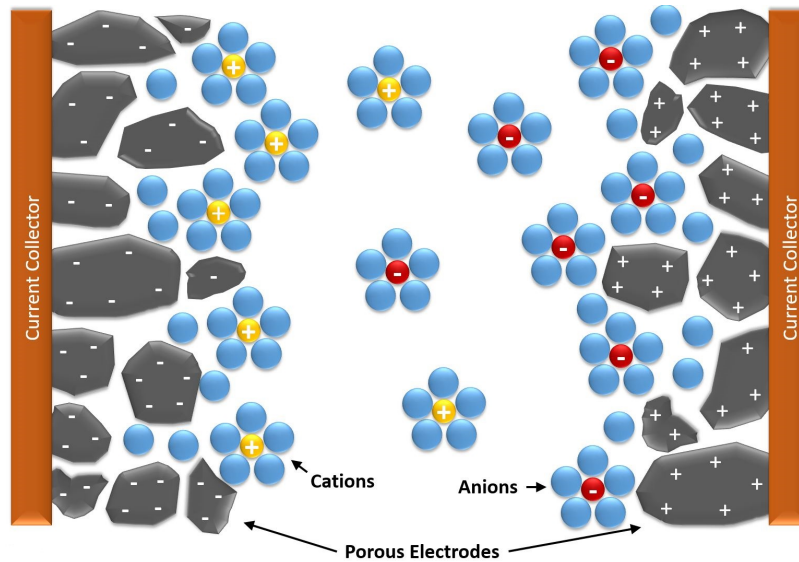


Figure 3.1: Porous structure of an Ultracapacitor(inspired by [2])

Due to the large capacitance of UCs, they have developed many applications in power system. Comparing with batteries, UCs have a larger power density. The charge releasing speed of UCs are always faster than chemical reaction based batteries. Therefore, UCs have been implemented in many applications with requirements of fast power supply. This also meets the requirements of fast active-power frequency response.

However, since UCs have different structures from parallel plate capacitors, some dynamic performance of UCs is also different from normal capacitors. In order to build detailed UC models, the dynamic properties of UCs should be considered in following aspects:

1. Distributed circuit elements: Unlike in parallel plate capacitors, charges are distributed on surface of the electrodes, the porous structures of UC electrodes contain more distributed charges forming numerous particle-scale electric fields. As shown in figure 3.1, the pores in electrodes are filled with electrolyte. This structure increases the effective area and decreases the distance between heterogeneous electrodes, which significantly increases the capacitance of UC. In order to model this distributed structure, partial capacitance and partial resistance need to be concerned[2].
2. Charge redistribution phenomenon: The diffusion ions travel a time in electrolyte into the porous electrodes leading to a spontaneously changing UC voltage. Because the apparent voltage (the voltage measured between the anode and cathode) changes faster than flowing speed of ions in electrolyte. Sometimes, an UC voltage appears like fully charged, but in fact ions have not fully flowed into the pores of electrodes. If the charging current stops at this time, the apparent voltage will spontaneously decrease and show the real state of charge of the UC. For this reason, UC with same amount of stored charges can have different voltage values. When current is larger, this partial charging phenomenon is more obvious. The redistribution phenomenon can be seen as delayed currents, which can be represented by different time constants of electric circuits.
3. Leakage current: The phenomenon of long-term voltage decline of an UC can be described by a parallel leakage resistance. However, if we focus our study on a 10s time scale of frequency stability control, the leakage current is negligible.

4. Voltage and temperature dependence: Experiments have proved that UC parameters are voltage and temperature dependant values [23]. In fact, an UC can be fully charged or discharged operating as an ESS in seconds [8], so UC parameters can be significantly influenced by its voltage. Meanwhile, UC parameters are also influenced by its temperature, especially in extreme environments[2]. However, the modeling of thermal environment is not the content of this thesis, so the operational temperature of UCs are assumed to be perfectly controlled.

As a result, property 1, 2 and 4 of an UC is consider in our thesis. A detailed UC model with distributed components, different time constants of circuits and voltage dependent parameters are going to be built in this thesis.

In previous ESS studies, UCs are usually modelled as an ideal capacitor in series with an equivalent series resistance (ESR) as shown in figure 3.2, e.g. in reference [16], [17], [18], and [19]. However, all the four aspects of dynamics are neglected in a simple RC model. The charging and discharging curve of a 4.2F simple RC model is compared with UC curves, which can show the difference of their dynamic performance. The apparent voltages of an UC model and a simple RC model are shown in figure 3.3a. The testing current is shown in 3.3b.

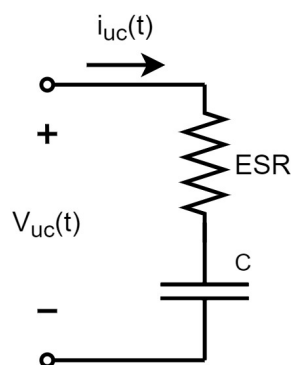


Figure 3.2: Simple RC represented UC model

In the first 1 second, the two models are charged with a constant 10A, and their voltage reach the maximum 2.27V at the same time. However, the ramp-rate of UC voltage decreases with time and does not like RC voltage which is proportional with time. The decreasing ramp-rate of UC voltage shows influence of voltage dependent capacitance. Later, during the time of zero current, the apparent voltage of UC changes spontaneously, which corresponds to the redistribution phenomenon. The ions in electrolyte are not completely located in porous electrodes in the first second of charging, and the UC curve during the zero current interval shows the process of still moving ions after charging. From 2s to 3s, two models are discharged with a 5A current. The increasing ramp-rate of UC curve proves the UC capacitance is decreasing with voltage value. The voltage curves have step changes at the turning points, because resistors share a certain amount of voltage when current flows. The final voltage of UC is lower than simple RC model, which means using a simple RC model to represent the UC model has a final voltage error of 0.046V in 4s. When many UC cells are integrated together, this error of modelling can also be accumulated, which have a bad influence on the result of UC implementation study. In this thesis, this error is expected to be overcome in the UC implemented frequency stability control.

As a conclusion, a simple RC model is not able to describe the dynamic properties of an UC including

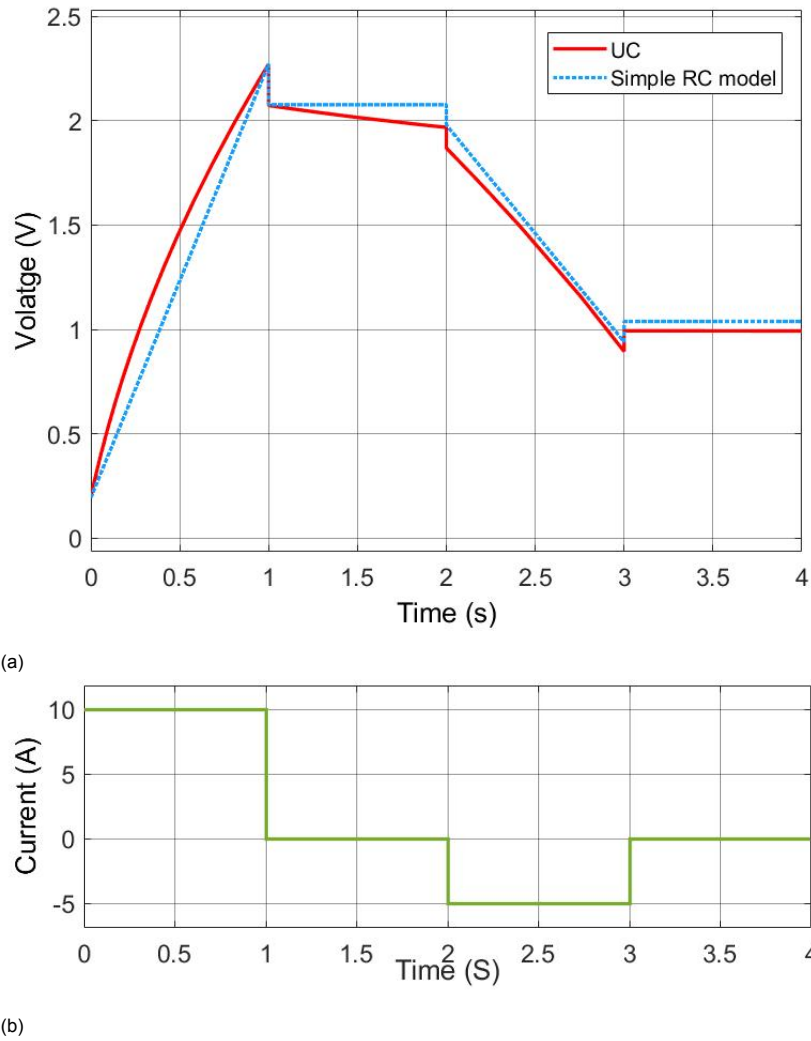


Figure 3.3: (a) Comparison of the terminal voltage between UC and simple RC model; (b) Charging and discharging current for testing

distributed components, charge redistribution and voltage dependent parameters. Therefore, extra modelling methods are required to represent these dynamic properties in a more detailed UC model. The methods of building detailed UC models are discussed in the next section.

3.2. UC Modelling Methods

This section illustrates the methods of building detailed UC models. References [2, 21–27] have proposed UC models based on different principles. These models can be summarized as equivalent electric circuit models and fractional-order models. Equivalent electric circuit models use resistance and capacitance formed circuits to represent the dynamic properties of UCs. The R, C values are estimated from the measurement of a real UC product. Equivalent electric circuit models are often used in power system simulations, because it is basically composed by normal electric elements which is easy to represent in power system models. On the other hand, fractional-order models use fractional-order capacitors which exhibit the capability of capturing UC dynamics. The impedance of a fractional-order model can be closer to the measured UC impedance than equivalent electric circuit models. The de-

tailed principles are going to be discussed in the following section. Finally, a most suitable UC model is selected for the study of fast active power-frequency control.

3.2.1. Equivalent electric circuit models

The general structures of equivalent electric circuit models can be considered as the composition of RC circuits. According to different structures, equivalent electric circuit models are classified as RC ladder models, RC parallel branch models and RC series-parallel branch models.

These models are derived from different principles, but their common idea is to simulate the performance of actual UCs by using simple electric circuit elements. However, they may have different estimation accuracy, because their principles only concentrate on partial behaviors of an UC in a certain application, e.g. a certain frequency range or time scale. Therefore, the principles and characteristics of these models should be studied before comparing and selecting the most suitable model for this thesis.

RC ladder model

RC ladder model or RC transmission line model has a strong physical meaning. It comes from the physical structure of an UC as shown in 3.1. The charges in porous electrodes forms numerous distributed capacitors, and the equivalent resistance of electrolyte connecting each of the capacitors. Hence, this RC ladder structure is formed between the anode and cathode of UC just like a transmission line. However, there are numerous microscope electric field distributed along this equivalent transmission line, and it is impossible to replicate this distribution in an electric circuit model. Therefore, this equivalent transmission is estimated by a finite number of RC circuits which is a RC ladder model. Considering the estimation accuracy and simple expression, RC ladder models are often 3 or 5 orders. An example of a three-order RC ladder model is shown in figure 3.4. As a outer layer capacitor, the state of C1 changes fastest with charging current i_{UC} . The charging speed of C2 is relative slower, and deepest layer capacitor C3 is the slowest. This is identical to the physical behavior of an UC. In figure 3.1, C1 represents the electric field at the surface of the electrodes, and C3 represents the electric field distributed in the deepest pores of electrodes. Hence, the delay of charging C2 and C3 creates the dynamics of distributed elements and charge redistribution.

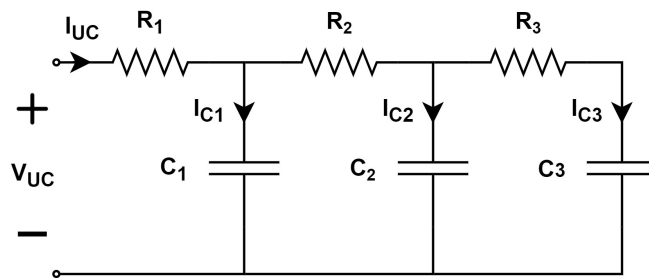


Figure 3.4: RC ladder model

The mathematical expression of a three-order RC ladder model is shown as :

$$\frac{V(s)}{I(s)} = \frac{As^3 + Bs^2 + Cs + 1}{Ds^3 + Es^2 + Fs} \quad (3.2)$$

where A to F are the circuit parameters dependent on R and C values in figure 3.4. In order to find the parameter values from an actual UC, a curve-fitting method is used to find the parameter values that give a closest UC impedance from the measured results of actual UCs.

As illustrated in subsection 3.1, voltage dependence of UC impedance is considered in this thesis. Therefore, the measured UC impedance used here for curve-fitting should also be voltage dependant. A technology known as Electrochemical impedance spectroscopy (EIS) is used to analyze the voltage dependence of UC impedance.

One example of measured Nyquist plot of UC impedance from EIS is shown in figure 3.5. This is a measurement result from reference [2]. During the EIS measurement, a series of AC excitation potentials with different frequency as equation 3.3 are applied on one UC cell. The measured current has a phase shift ϕ as equation 3.4. Then, the complex impedance of an UC can be calculated.

$$E(t) = E_0 \sin(\omega t) \quad (3.3)$$

$$I(t) = I_0 \sin(\omega t + \phi) \quad (3.4)$$

The test excitation potential is generated with a 0.01HZ to 10kHz sweep frequency which corresponds to the frequency range of Nyquist plot. In figure 3.5, every impedance curve moves along the direction of frequency increase from 0.01HZ to 10kHz. The full capacitance of an UC is only available in DC condition. Due to the porous electrodes, the UC resistance is higher for lower frequency. By measuring the real part and imaginary part of UC impedance under different voltages, trajectories from 0.037V to 2.5V are plotted in figure 3.5. Since the trajectories are voltage dependent, the R and C values of an UC can be considered as functions of UC voltage. If the functions for R and C can be formulated, the UC ladder model is determined.

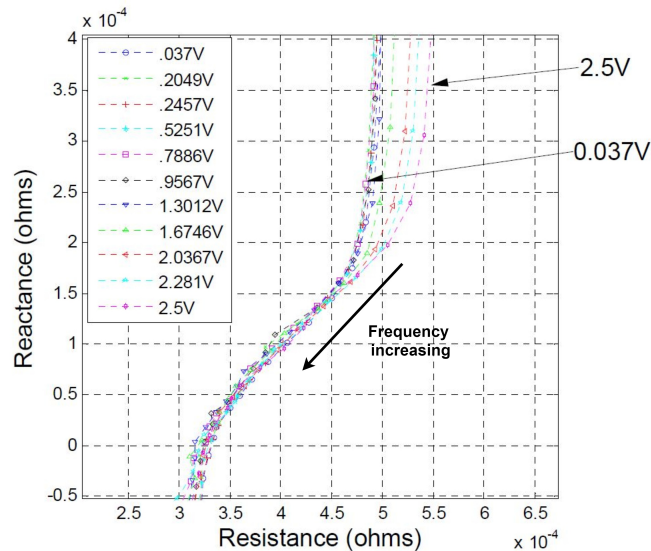


Figure 3.5: Nyquist plot of UC impedance from EIS[2]

Reference uses polynomial functions to estimate R and C functions during the curve-fitting. The results of curve-fitting is evaluated by the root-mean-square-error (RMSE) which is formulated as

$$\begin{aligned}
RMSE &= \sqrt{\frac{\sum_{i=1}^N error_i^2}{N - N_{fitted\ points}}} \\
&= \sqrt{\frac{\sum_{i=1}^N [(R_{model} - R_{true})^2 + (X_{model} - X_{true})^2]}{N - N_{fitted\ points}}}
\end{aligned} \tag{3.5}$$

where N is the total number of impedance points measured in EIS. This RMSE shows the average Euclidean distance between model curve and measured curve. A model curve with smaller RMSE has a better identity with measured curve. Therefore, the curve-fitting result with minimum RMSE gives the most accurate estimation of UC parameters. In [22], the UC model is charged to different voltage levels step by step, and the error of terminal voltage is less than 0.05V. In second test, UC is fully charged from empty resulting a maximum -0.1V error.

A RC ladder model is often used in the study of UC principles and manufacture rather power system applications. Because the solution for C_1 , C_2 and C_3 voltage has a complex analytical expression which is complicated to be implemented in simulations. Besides, in power system applications, people may prefer to know the state of charge of a whole UC rather than the charge distribution state at outer layer and inner layer.

RC series-parallel branch model

In order to explain the principle of RC series-parallel branch models, the EIS of an UC should be analyzed. As shown in figure 3.5, the curves at resistance axis have a inserting value around $3.2 \times 10^{-4}\Omega$ which can be described as a series resistance named R_a . The curves' ramp have an angle around 45° , which can be recognised as the impedance of porous structure of electrodes named $Z_p(j\omega)$ [28]. Figure 3.5 also shows that the real part of an UC decreases with frequency increasing, reference [24] finds an equation to represent the impedance of porous electrodes as

$$Z_p(j\omega) = \frac{\tau \cdot coth(\sqrt{j\omega\tau})}{C_a \cdot \sqrt{j\omega\tau}} \tag{3.6}$$

where τ is the time constant of porous electrodes; C_a is the maximum capacitance can be used in an UC. The time domain expression of impedance $Z_p(j\omega)$ can be transferred as

$$\frac{\tau \cdot coth(\sqrt{j\omega\tau})}{C_a \cdot \sqrt{j\omega\tau}} \Rightarrow \frac{1}{C_a} + \frac{2}{C_a} \sum_{n=1}^{\infty} e^{-\frac{n^2\pi^2}{\tau}t} \tag{3.7}$$

Equation 3.7 represents the impedance of porous electrodes as a capacitor C_a in series with infinite numbers of RC parallel branches. For real-time simulations, the RC series-parallel branch model is estimated by a three-order electric circuit same as the example of RC ladder model[23]. Then only two RC parallel branches left in equation 3.7, which have time constants $\frac{\tau}{\pi^2}$ and $\frac{\tau}{4\pi^2}$. The the parameters of two RC parallel branches are expressed as

$$C_1 = C_2 = \frac{C_a}{2}, R_1 = \frac{2\tau}{\pi^2 C_a}, R_2 = \frac{\tau}{2\pi^2 C_a} \tag{3.8}$$

where C_1 and C_2 are capacitance of two branches; R_1 and R_2 are resistance of two branches.

As a summary, the total impedance of a RC series-parallel branch model is expressed as

$$\begin{aligned} Z(j\omega) &= R_a + Z_p(j\omega) \\ &= R_a + \frac{\tau \cdot \coth(\sqrt{j\omega\tau})}{C_a \cdot \sqrt{j\omega\tau}} \end{aligned} \quad (3.9)$$

Figure 3.6 shows the structure of a three-order RC series-parallel model according to equation 3.9. In steady states, all energy is stored in main capacitor C_a , and the voltages of C_1 and C_2 should be 0, which means that the voltage of capacitor C_a also represents the SOC of this UC. When a charging current I_{UC} is applied on this RC series-parallel model, capacitors C_1 and C_2 are getting charged by currents I_{C1} and I_{C2} . With the increase of C_1 and C_2 voltages, currents I_{C1} and I_{C2} gradually converge to 0. This phenomenon makes terminal voltage V_{UC} increase faster at the beginning of charging. When charging current is removed, energy stored in C_1 and C_2 is dissipated in R_1 and R_2 , which creates a spontaneous voltage decreasing after charging corresponding to the charge redistribution phenomenon. As a conclusion, the main capacitor represents the SOC, and two parallel branches create the dynamic properties of an UC.

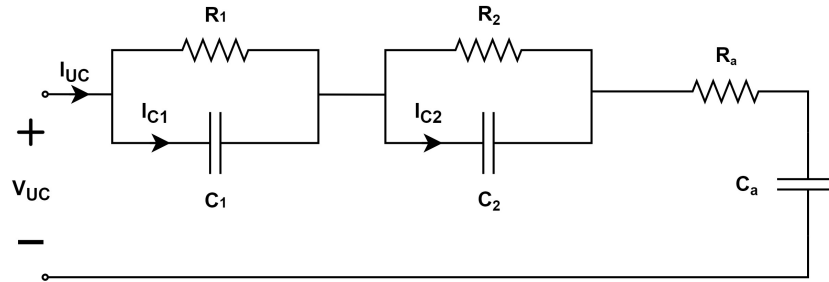


Figure 3.6: RC series-parallel model

As shown in equation 3.9, the three unknown parameters of a RC series-parallel branch model are R_a , C_a and τ . These parameters are all voltage dependant. The unknown variables are time constant τ and main capacitance C , which should be determined by curve-fitting. Similar with the curve-fitting in RC ladder model, polynomial curves are used to estimate the measured impedance curves of EIS. The curve-fitting result with minimum RMSR gives the optimal solution.

RC parallel branch model

As name implies, RC series branches are all in parallel in this model. RC parallel branch model is relatively simpler than RC ladder model on structures. Because the charging state of each RC branch is independently influenced by terminal voltage V_{UC} . One example of RC parallel model is shown in figure 3.7, where the subscripts "f", "d" and "l" stands for fast branch, delayed branch and long-term branch. The fast branch has the smallest resistance and RC time constant around seconds. The delayed branch is relatively slower with a time constant around minutes, and the long-term branch is the slowest with a time constant around half an hour. The reason for implementing different time constants of RC branches is to represent distributed elements and charge redistribution. In steady state, capacitor voltages of three branches equal to the terminal voltage V_{UC} . When terminal voltage V_{UC} changes due to charging current I_{UC} , the voltage of fast branch capacitor C_f changes fastest to follow the terminal voltage. The delayed branch and long-term branch follow in a longer time scale,

which leads to voltage differences between these branches. For this reason, the capacitor voltages will change spontaneously even when external current is removed, which corresponds to the charge redistribution phenomenon.

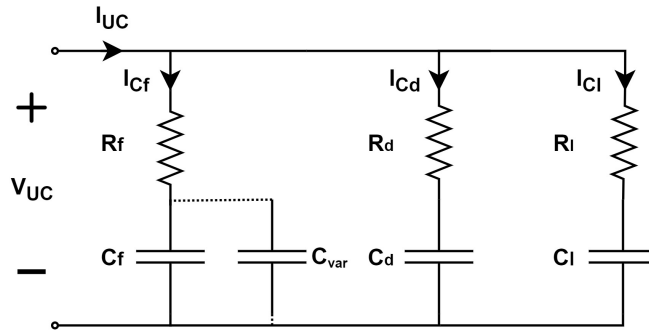


Figure 3.7: RC parallel branch model

The voltage dependant parameters can be estimated by using polynomial curve-fitting of EIS curves same as cases of RC ladder model and RC series parallel mode. However, EIS tests require strict experimental facilities, and the measured impedance spectrum is also complicate to be processed into R and C values corresponding to model parameters. A simplified way can be used to determine parameter values according to reference [26] and [21].

Instead of measuring the EIS of an UC, reference [26] measures UC voltage to estimate parameter values. As mentioned in the principles of RC parallel branch models, the three RC series branches are defined as a fast branch (with a time constant around 20ms), a delayed branch (around 100s) and a long-term branch (around 30 minutes). Since the time ranges of three branches are very distinct, we can use a constant current test lasting a specific time to test every branch separately. For example, a current source is switched on for 20ms, and the measured UC voltage can be assumed to be fully influenced by the fast branch, because the currents of delayed branch I_{Cd} and long-term I_{Cl} are very small in 20ms. After determining values for R_f and C_f , the charging time increases to 100s which is the time scale for the delayed branch. Since parameters of the fast branch have been calculated, the delayed branch current I_{Cd} can be calculated by deducting the fast branch current I_{Cf} . Similar for long-term branch, the UC is charged for 30min, and the long-term parameters R_l and C_l are estimated by calculating the current for long-term branch I_{Cl} . By using this constant current test, the complicated EIS curve-fitting is avoid.

Reference [21] further simplifies the UC parallel branch model and parameter estimation. Since UCs are used for fast active-power response in a few seconds, the behavior of delayed branch and long-term branch is less important than the fast branch. Therefore, parameters expect the fast branch capacitor are assumed constant. The fast branch capacitor is formed by a constant capacitor C_f and a voltage dependent capacitor C_{var} which can be expressed as equation 3.10.

$$C_{var} = K_V \cdot V_{UC} \quad (3.10)$$

where K_V is the voltage-dependant capacitance constant determined in the constant current test.

By using constant current tests and variable capacitance of fast branch capacitor, the RC parallel branch model is simplified especially for applications of fast active power.

3.2.2. Fractional-order model

In subsection 3.2.1, an UC is represented by different types of electric circuit models. These models can also be categorised as integer-order models. Because their R and C elements can be represented by ordinary differential equations. On the other hand, fractional-order models, based on fractional-order differential equations, have attracted increasing interest in UC modeling research [29]. Because they exhibit the capability of capturing UC dynamics including distributed elements, charge redistribution and voltage dependence. For equivalent electric circuit models, equations like equation 3.7 are used to represent UC impedance, and these equations need to be simplified into a finite term of expression in real applications. In contrast, fractional-order models can achieve a better dynamic performance with fewer parameters.

A discrete version of Grünald-Letnikov formulation of fractional-order calculus is shown as follow [25]:

$$D^\alpha y(t) = (\Delta t)^{-\alpha} \sum_{j=0}^{\lceil t/\Delta t \rceil} (-1)^j \binom{\alpha}{j} f(t - j\Delta t)$$

$$\binom{\alpha}{j} = \frac{\alpha!}{j!(\alpha - j)!} \quad (3.11)$$

where D^α means the integral-differential operator with order α ; Δt is the discrete time interval; $\lceil t/\Delta t \rceil$ represents the memory length needed to consider; $\binom{\alpha}{j}$ is the Newton binomial coefficient. For fractional calculus, α can have any continuous values rather than integer numbers in ordinary differential equations. When α is larger than 0, D^α means fractional derivatives; When α is smaller than 0, D^α means fractional integrals.

With the definition of fractional calculus, a fractional-order capacitor can be expressed as equation 3.12, where $0 < \alpha < 1$ stands for a fractional derivative order smaller than a normal capacitor.

$$Z_{UC}(j\omega) = \frac{1}{C(j\omega)^\alpha}, \quad 0 < \alpha < 1 \quad (3.12)$$

According to the definition of fractional derivative, the current through this fractional capacitor is actual related to the historical states of voltage. Therefore, it is possible to use finite fractional-order elements to fully describe the dynamic phenomenon of an UC. One example of fractional-order modeling for UC is shown in figure 3.8 [25]. A Walburg-like element ($Z_w = \frac{1}{W s^\beta}$) is adopted to represent the main capacitance of UC, and a constant phase element (CPE, $Z_{CPE} = \frac{1}{C s^\alpha}$) is connected in parallel with a charge-transfer resistance R_c to create the the dynamics of distributed elements and charge redistribution. The six parameters $[W, C, \beta, \alpha, R_c, R_s]$ of this fractional-order model can also be estimated by curve-fitting of the measured UC impedance. Curve-fitting result shows that the impedance of fractional-order model is more close to the measured experimental data than the impedance of equivalent electric circuit models, especially for low frequencies[25].

However, fractional-order model are not often applied in power system applications. One reason is that the benefits of implementing fractional-order circuit elements are not motivating enough, because fractional-order circuit theorem is rarely used in applications, and more research work is required to apply this fractional-order model in electric circuits[30]. In fact, in order to run numerical simulations for

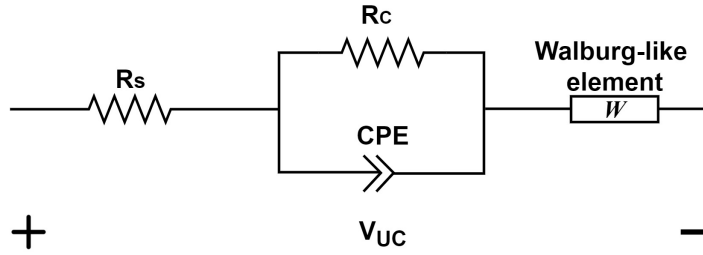


Figure 3.8: Fractional-order UC model

fractional-order systems, fractional-order calculus still needs to be estimated by integral-order calculus. One example is Oustaloup's recursive approximation shown as follow[30]

$$s^\alpha = \prod_{n=1}^N \frac{1 + s/\omega_{z,n}}{1 + s/\omega_{p,n}} \quad (3.13)$$

where $\omega_{z,n}$ and $\omega_{p,n}$ are designed zeros and poles. The accuracy of approximation is determined by number of terms N . So the approximation of a fractional-order capacitor can be similar like the equation 3.2 of RC ladder model impedance. Besides, this approximation is only valid in a certain range of frequency. As a result, it is not necessary to implement a fractional-order model in this thesis.

3.2.3. Summary of UC modeling methods

In this section, we introduced four types of UC models which have been studied in the existing literature. Table 3.1 lists their characteristics.

Considering the study of fast active power-frequency response in this thesis, UCs are implemented as the solution of fast active power demands. Therefore, the time domain of UC simulation is focused on a few seconds, which corresponds to the high-frequency performance of UC models. Table 3.1 shows that RC parallel branch models are based on different time scales of UC performance, so Hence, the design of RC parallel branch model is more suitable to the time-scale dependent applications like fast active power-frequency control. Besides, the fast branch of a RC parallel branch model has a relatively higher curve-fitting accuracy than slower branches, which is exactly the time domain of fast active power-frequency control. In contrast, RC ladder models and RC series parallel models emphasize the average curve-fitting accuracy over a wide range of frequencies, and their physical meanings are more related to the UC structures rather than time scales. This means that their parameters are selected only according to the dynamic principles itself like charge redistribution, and UC performance in different time scales are not distinguished. Fractional-order models are theoretically more accurate in curve-fitting of UC impedance, but they are not practical to be implemented in the simulation of fast active power-frequency control because of lack of fractional-order circuit theorem applications and integer-order approximations.

Table 3.1: Qualitative comparison between UC models

UC models	Properties
RC ladder model	<ol style="list-style-type: none"> 1. Physical properties: This model is derived from the porous structure of an UC, and it is able to reflect the actual charge distribution with an UC. 2. Merits in simulations: It has the ability to simulate distributed capacitance and electrolyte resistance. Because parameters are derived from EIS curve-fitting, model values fit the experimental data very well in a wide range of frequencies. 3. Drawbacks in simulations: The states of charge distribution within electrolyte and electrodes are not the goal of this thesis study. Instead, a rather clear form of UC model like the other two forms of UC model is more preferred.
RC series-parallel branch model	<ol style="list-style-type: none"> 1. Physical properties: This model is derived from the mathematical expression of UC EIS curves, and it has the most identical nature to an EIS curve. 2. Merits in simulations: It theoretically has the ability to replicate the impedance of an UC in different frequencies. The SOC of an UC is clearly shown by the voltage of main capacitor. 3. Drawbacks in simulations: The selected time constants of RC series parallel branches can influence the model performance, hence in real applications, various of time constants are tested to find the optimal one.
RC parallel branch model	<ol style="list-style-type: none"> 1. Physical properties: This model is based on the UC performance on different time scales, and the time constants of branches are selected according to different time scales. 2. Merits in simulations: It has a relatively higher high-frequency accuracy (model current in time domain of milliseconds is most identical with measured UC current), because the voltage dependent capacitor is applied only the fast branch. This is beneficial to our study of fast active-power frequency response. The charging state of each RC branch is independently influenced by the terminal voltage V_{UC}. 3. Drawbacks in simulations: In order to improve high-frequency accuracy of curve-fitting, some slow dynamic performance like voltage dependence of delayed branch and long-term branch is compromised.
Fractional-order model	<ol style="list-style-type: none"> 1. Physical properties: Model is expressed by fractional-order calculus. It has a memory ability, because the current value of a fractional-order capacitor is influence by historical voltage values, which is very close to the inherent characteristics of an UC. 2. Merits in simulations: Comparing with equivalent electric circuit models, fractional-order models have a higher accuracy in curve-fitting with measured UC impedance, and fractional-order models have less parameters, which makes this model easy to express. 3. Drawbacks in simulations: More technology of fractional-order circuit theorems is required to fully implement fractional-order model in power system simulations. Currently, the approximation of fractional-order calculus limits the accuracy of fractional-order models.

As a conclusion, a UC parallel branch model is selected due to four reasons:

1. RC parallel models are based on time scales of UC performance, which is also the research scope of fast active power-frequency control.
2. Fast active power-frequency control focus on the power response in a few seconds. The fast branch of RC parallel model has a relative higher accuracy in curve-fitting of UC impedance, which is also in a time scale of a few seconds.
3. The impedance accuracy of the fast branch of UC parallel branch models is guaranteed and not influenced by other branches during simulations. Because the charging state of each RC branch is independently influenced by the terminal voltage V_{UC} .

In next subsection, the selected RC parallel branch model is going to be implemented in RSCAD environment.

3.3. Implementing UC Model in RSCAD Environment

This thesis uses the builtin c-builder in RSCAD to create the UC model for simulations. The four steps to create a component model in RSCAD c-builder is shown in figure 3.9. Drawing the graphic UC not only determines the symbol of UC, but also defines the data input and output of UC model during simulations. The graphic drawing area in c-builder is shown in figure 3.10. If the designed component is an electric element like an UC, the terminals should be selected as physical nodes. A physical node is allowed to connect with other physical components in a RSCAD model. This UC has two physical nodes which stands for the two current collectors.

Step 2 is defining parameters. The inner parameters of a component model is defined on the right side of figure 3.10. The parameter definition allows the parameter values to be assigned in a RSCAD model. In the case of UC model, the parameter definition should not only includes the UC parameters discussed in section 3.2, but also the names for the output variables, e.g. the name for the output current of a UC model. Because every variable should has a unique name in a RSCAD model. Besides, the size of a UC storage system is also defined here including the series number of UC cells $N_{s,UC}$ and the parallel number of UC cells $N_{p,UC}$. Both the storage systems for UCs and batteries are considered as matrix forms in this thesis as figure 3.11. Every UC cell represents a UC parallel branch model in figure 3.7.

The third step, C source code determines the actual function of this model. Mathematical representation of an UC model should be written in this C code file. This is achieved under the "C File Associations" tab shown in figure 3.12. The nodes defined in step 1 and parameters defined in step 2 are automatically associated with the model and placed in a ".h" file. As the RC parallel branch model of an UC is composed by R and C elements, the representation of a normal capacitor in c-builder should be studied.

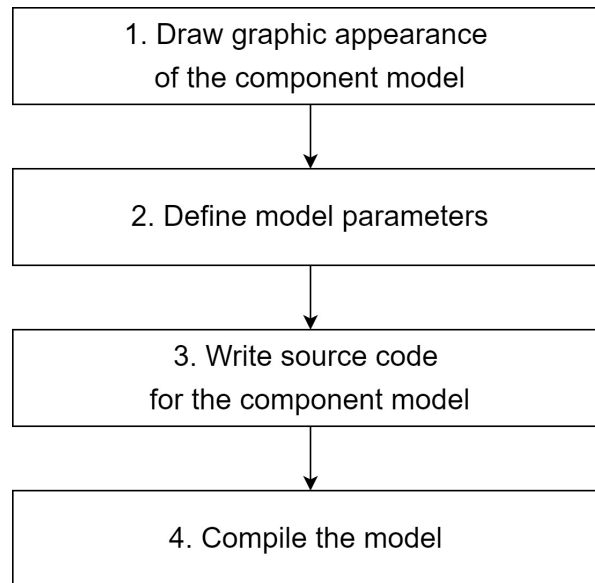


Figure 3.9: Four steps to create a component model in RSCAD c-builder

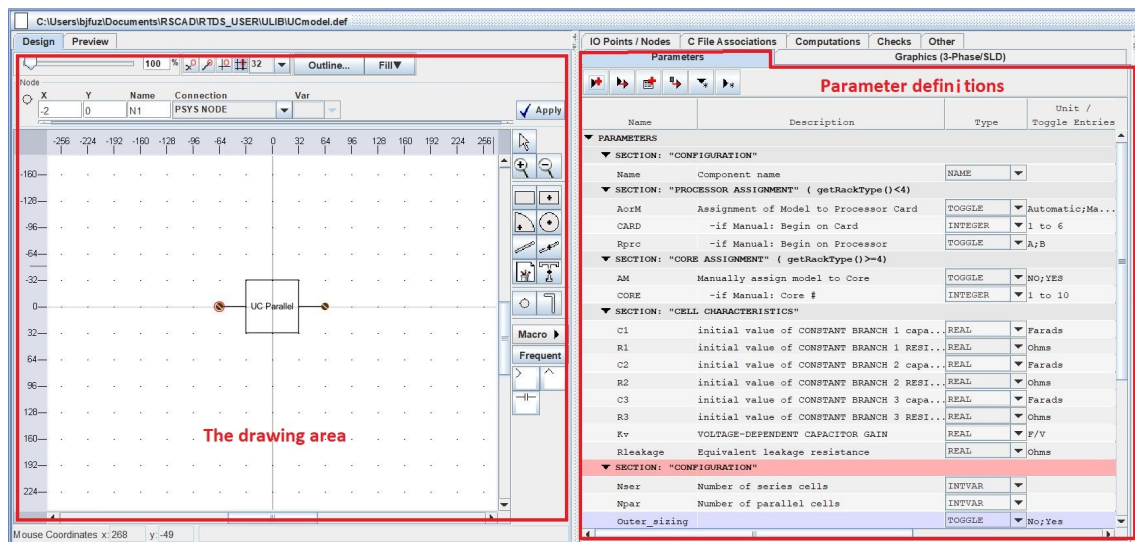


Figure 3.10: User interface of RSCAD c-builder

For a normal capacitor, the voltage over it can be represented as the integral of current divided by capacitance as shown in equation 3.14, where Δt is the simulation time step.

$$\begin{aligned}
 V(t) &= \frac{1}{C} \int_0^t i(t) dt + V(0) \\
 &= \frac{1}{C} \int_{t-\Delta t}^t i(t) dt + V(t - \Delta t)
 \end{aligned}
 \tag{3.14}$$

However, integral in c-builder is calculated by trapezoidal rule. The integral in one simulation time step is estimated by the trapezoidal area as shown in the equation 3.15 [4]. The continuous capacitor current $i(t)$ is discretized by a sampling time Δt .

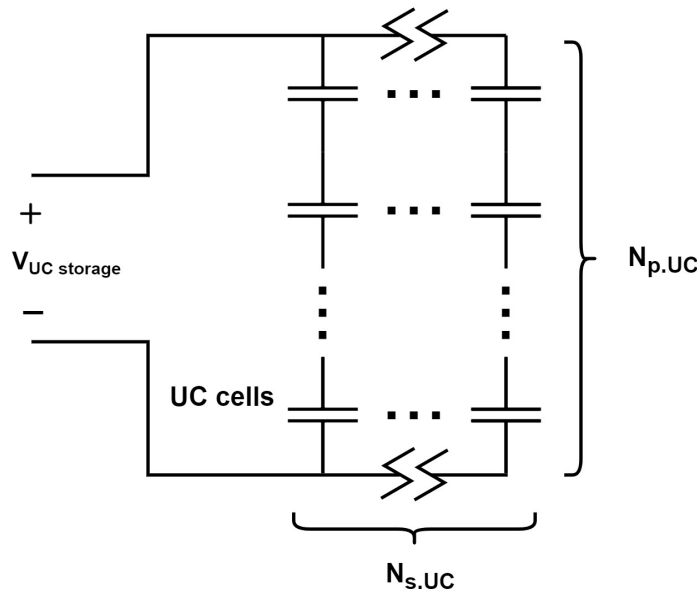


Figure 3.11: Structure of the UC storage system

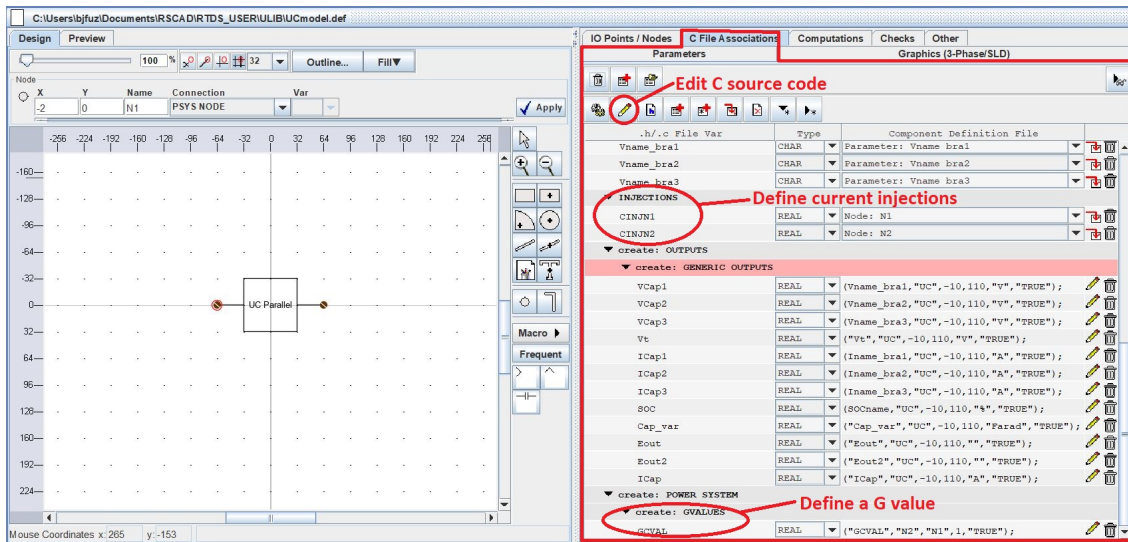


Figure 3.12: Tab of C file associations

$$V(t) \approx \frac{1}{C} \cdot \frac{\Delta t}{2} \cdot (i(t) + i(t - \Delta t)) + V(t - \Delta t) \tag{3.15}$$

Another rule of c-builder is that an electric component should be represented as a Norton equivalent circuit [4]. In every time step of RTDS, the Norton circuit of components are used to calculate the voltage result of the power system model. A Norton form is represented as a conductance in parallel with a current source. This is the rule of electric circuit calculation in RSCAD. The power system model is represented as a network of Norton equivalent circuits, all the current injections are already known before the start of one simulation time step. The voltage for each electric component is calculated by solving this network. Therefore, equation 3.15 is transformed as a Norton equivalent form in equation 3.16, where G is the equivalent conductance and $I_{CS}(t)$ is the equivalent current source. It is worth to

notice that G and $I_{CS}(t)$ does not stand for the real physical value of a model. The G value is represented as a conductance, because it is associated with the current voltage $V(t)$. For the terms in $I_{CS}(t)$, these are all memory values not associated with the current voltage $V(t)$, hence they can be treated as extra current injections in parallel with conductance G . By using this way, a capacitor is represented as a conductance in parallel with a time-varying current source, which can participate in RTDS calculations.

$$\begin{aligned} i(t) &= \frac{2C}{\Delta t} V(t) + \left(-\frac{2C}{\Delta t} V(t - \Delta t) - i(t - \Delta t) \right) \\ &= G \cdot V(t) + I_{CS}(t) \\ G &= \frac{2C}{\Delta t}, \quad I_{CS}(t) = -\frac{2C}{\Delta t} V(t - \Delta t) - i(t - \Delta t) \end{aligned} \quad (3.16)$$

Further considering the representation of a RC series branch in c-builder, its voltage can be represented as equation 3.17 according to trapezoidal rule. The RC series branch circuit and its Norton equivalent circuit is shown in figure 3.13. The conductance should be represented as the term proportional with terminal voltage $V(t)$, and the additional terms are expressed as the current source $I_{CS}(t)$. Therefore, the Norton equivalent circuit of a RC series branch is formulated as equation 3.18. Comparing with the expression for a normal capacitor, a RC series branch has an extra time constant of RC .

$$V(t) \approx \frac{1}{C} \cdot \frac{\Delta t}{2} \cdot (i(t) + i(t - \Delta t)) + R \cdot (i(t) - i(t - \Delta t)) + V(t - \Delta t) \quad (3.17)$$

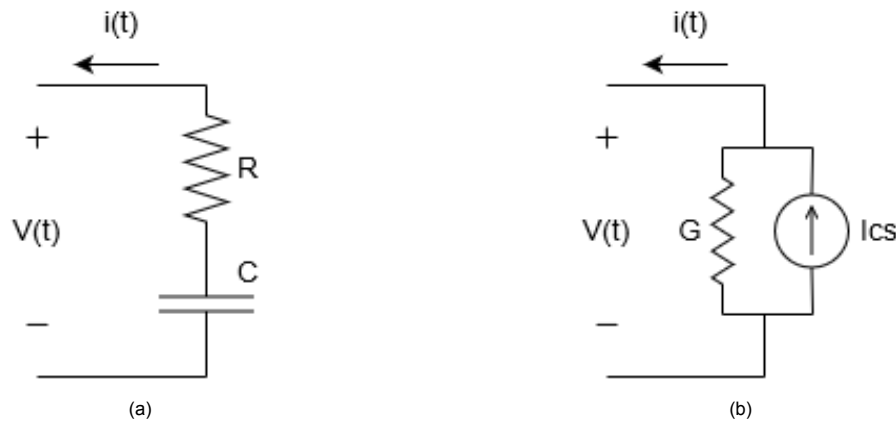


Figure 3.13: (a) RC branch circuit, (b) Norton equivalent circuit

$$\begin{aligned} i(t) &= \frac{2C}{2RC + \Delta t} \cdot V(t) - \frac{2C}{2RC + \Delta t} V(t - \Delta t) + \frac{2RC - \Delta t}{2RC + \Delta t} i(t - \Delta t) \\ &= G \cdot V(t) + I_{CS}(t) \\ G &= \frac{2C}{2RC + \Delta t}, \quad I_{CS}(t) = -\frac{2C}{2RC + \Delta t} V(t - \Delta t) + \frac{2RC - \Delta t}{2RC + \Delta t} i(t - \Delta t) \end{aligned} \quad (3.18)$$

An UC parallel branch model should also be expressed as a Norton form which has the same structure as figure 3.13b. The values for every RC branch is estimated as table 3.2 in reference [26]. The Norton expression of an UC model is composed by the Norton circuits of RC branches. In figure

3.12, a "GVALUES" is defined to stand for the conductance G , and two "INJECTIONS" are defined to represent the current source $I_{CS}(t)$ seeing from two nodes, which equal to $I_{CS}(t)$ and its minus. In the C source code of this UC model, the Norton circuit of each RC branch is expressed as equation 3.18. For the fast branch, the capacitance value is voltage dependent, which is calculated in every simulation step to update the UC capacitance. Since the three RC branches in this model is all in parallel, an RC parallel branch model is expressed as a conductance G_{UC} in parallel with a current source $I_{CS,UC}(t)$ by summing up the conductance $[G_f, G_d, G_l]$ and current sources $[I_{CS,f}, I_{CS,d}, I_{CS,l}]$ of three branches as equation 3.19. As two physical nodes are defined for an UC model in the drawing area of figure 3.10, the voltages of two nodes are calculated in every simulation step and delivered as input signal $V(t)$ to the UC model. If the R and C parameters are voltage dependent, their new parameter values are calculated as a function of voltage $V(t)$. $V(t - \Delta t)$ and $i(t - \Delta t)$ as the UC voltage and current of last simulation step are known already. With the updated G and I_{CS} , RTDS is able to calculate the new voltage value of every node in power system model. In next simulation step, this procedure repeats again.

Table 3.2: Estimated parameters of RC parallel branch model

$C_f : 270F$	$R_f : 2.5m\Omega$	$C_d : 100F$	$R_d : 0.9\Omega$
$C_l : 220F$	$R_l : 5.2\Omega$	$K_V : 190F/V$	

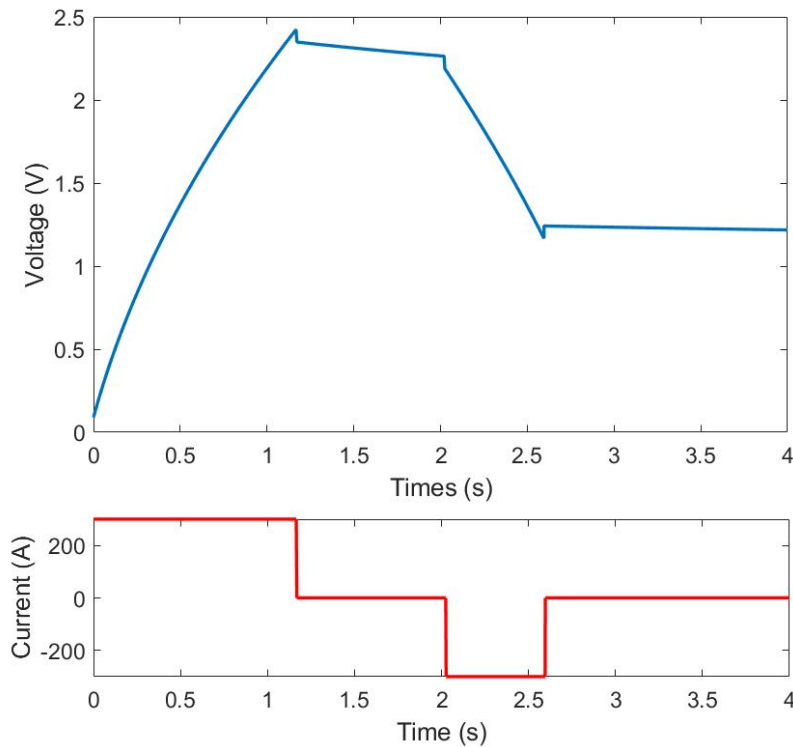


Figure 3.14: Test of RC parallel model in RTDS

$$\begin{aligned}
 G_{UC} &= G_f + G_d + G_l \\
 I_{CS,UC}(t) &= I_{CS,f} + I_{CS,d} + I_{CS,l}
 \end{aligned}
 \tag{3.19}$$

The final step before using the UC model in RTDS is compiling this model in c-builder. If no syntax error happens, a machine code is created, which contains the instructions to run this UC model in RTDS.

The RC parallel model implemented in RTDS is shown in figure 3.14. In the first second, model shows the voltage dependence of an UC. After charging, spontaneous changing voltage shows the charge redistribution phenomenon in an UC. As a summary, after implementing a RC parallel model in RSCAD environment, the expected UC dynamics can still be represented.

3.4. Summary for UC Modelling and RSCAD Implementation

The study of UC principles and dynamic properties answers the research question 1 (What are the dynamic properties of an UC that should be taken into account for EMT modeling and simulation of interconnected power system?). It shows that UC has distributed elements. Charges stored in these elements are redistributed along with time. Besides, UC parameter values are voltage dependent. The considered dynamics have been proved necessary to be represented in UC models by comparing with a simple RC series model in a few seconds.

Research question 2 (How can a generic UC model be designed in RTDS environment based on the capabilities of RSCAD?) is answered by quantitatively analyzing and comparing UC models proposed in reference. RC parallel branch models are finally selected due to different time scales of branches, high accuracy in short term and independently connected branches. These advantages are beneficial to the real time simulation of fast active-frequency control. After selecting the RC parallel branch model, this model is implemented in RSCAD by using the builtin c-builder. This UC model is ready to operate as an ESS in power system simulations.

In next chapter, a battery and UC based HESS is implemented as the energy source in the real-time simulations of frequency stability control.

4

Application of HESS in Frequency Stability Control

This chapter introduces the UC and battery based HESS where the UC is represented by the RC parallel model. The HESSs are implemented in a modified IEEE 9 bus system with 52% of wind generations. A testament proves that UCs have a faster reacting speed and higher power density than batteries. Therefore, the fast changing power component is allocated to the UCs. After determining the HESS, the rules of energy sizing is concluded from a series of output power tests.

4.1. Setting for FDWG Implemented 9 Bus IEEE System

The 52% of power generation in IEEE 9 bus system is replaced by FDWGs at bus 7 and bus 3. FDWGs cannot contribute natural inertia to power system. Therefore, the system inertia is decreased, and power system frequency becomes more vulnerable to disturbance. The structure of FDWG and ESS connected on the DC-link is shown in figure 4.1. The values of generation and loads are listed in table 4.1. Wind generators are connected to power grid through back-to back converters. The rotor-side-converter is controlled to transfer the maximum amount of power from wind generators. The grid-side-converter is under voltage control to maintain the DC-link voltage constant.

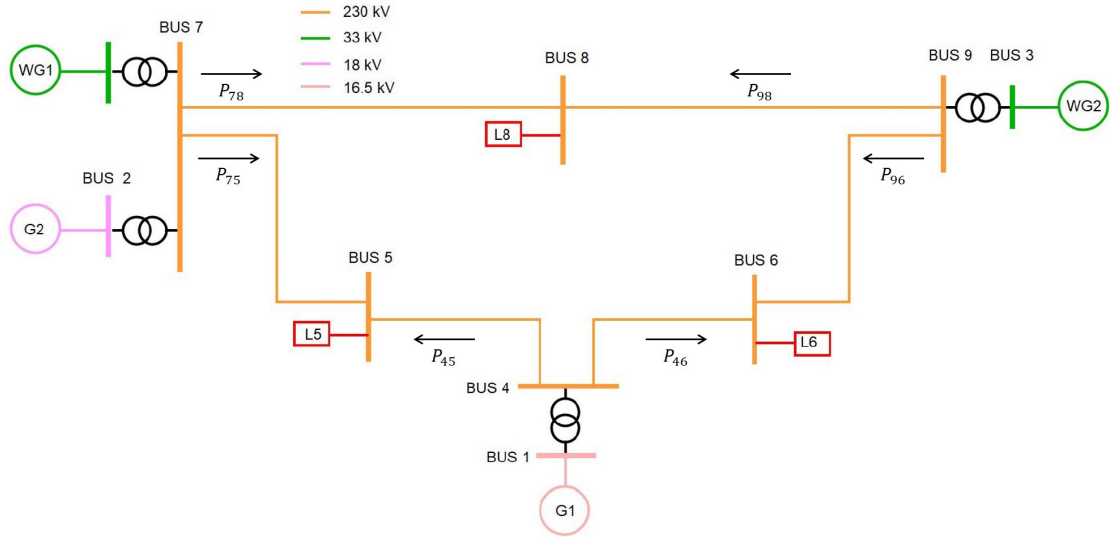


Figure 4.1: IEEE 9 bus system with 52% wind generations [3]

Table 4.1: Power flows in IEEE 9 bus system

Load Flow Results		P (MW)	Q (Mvar)
Generations	G1	73.4	33.8
	WG1	82.6	0
	G2	78.2	-1.8
	WG2	84	0
Loads	L5	125	50
	L6	90	30
	L8	100	35

A load step increases at bus 8 is used to test the frequency stability of this power system. The scale of load increase is according to the largest generation which is wind generation WTG2 84MW. This load increase does not change the direction of power flows but their magnitudes. At the beginning of load increase, more active power is drawn from the rotating mass of synchronous generators, which is the reason of frequency drop. The HESSs with batteries and UCs are mounted on DC-links of FDWG at bus 7 and bus 9 as the energy source for frequency control. The power balance of synchronous generators will be restored by increasing the power output from FDWGs. In order to guarantee the healthy operation of power system, the goal of frequency control is to prevent frequency drops below the admissible value and mitigate the changing speed of frequency.

In normal operations, directions of power flows are shown in figure 4.1. When load 8 increases at bus 8, synchronous generator G1 and G2 will increase their active power output. The power flows P_{78} and P_{98} increase immediately. These increasing power flows are from the natural contributions of synchronous generators. However, FDWG generations are remaining constant at the beginning, which causes a difference between FDWG generations and increasing power flows P_{78} and P_{98} . For example, the original power flow P_{98} is 0.25 times of WG2 generation P_{WG2} . When load 8 increases 84MW, the power flow increases to 0.72 times of P_{WG2} . As a result, this power difference can be used as the power

reference of VSP controllers.

The studied methods including droop and derivative control and VSP are both going to be implemented in this IEEE 9 bus system to compare their performance and characteristics. Before result evaluations, the HESSs and frequency controllers should be tuned optimally.

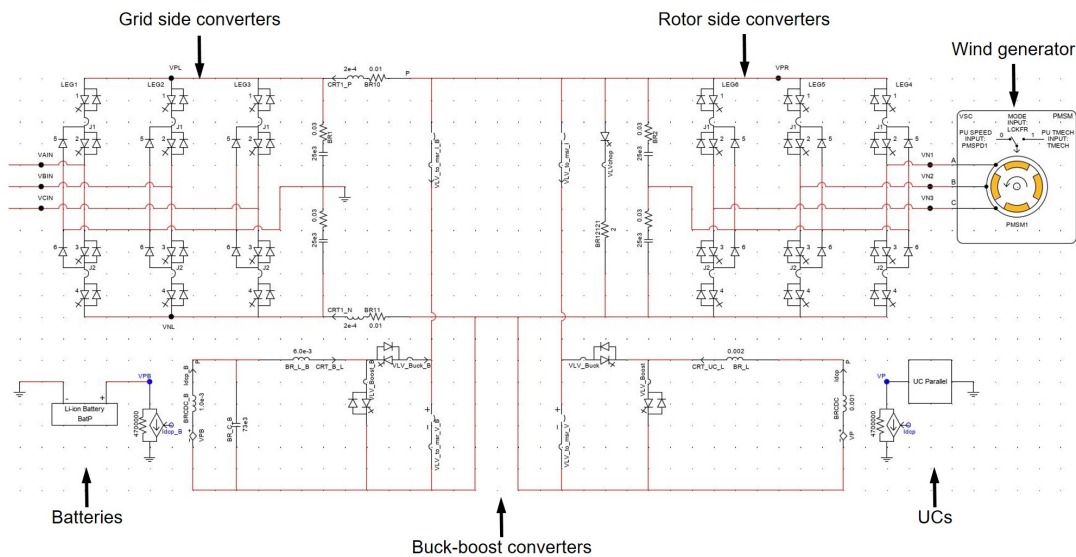


Figure 4.2: Fully decoupled wind generator with ESS connected on the DC-link

Figure 4.2 shows the FDWG in RSCAD environment. The wind generator is connected with power grid through the rotor-side converters and the grid-side converters. The rotor-side converters controls output power from the wind generator. The grid-side converters maintains constant DC-link voltage to ensure normal operation of the FDWG. Capacitors are used to support DC-link voltage. A HESS is connected on DC-link through buck-boost converters. When extra power from HESS goes to DC-link, the DC-link voltage will increase and force grid-side converters to transfer more power to the grid. Inductors and capacitors are used as filters on buck-boost converter to keep current and voltage stable.

4.2. Comparison between UC and battery

Before implementing the HESSs, a comparison between UC and battery is made to illustrate the advantages of using UCs in HESSs. From the perspective of their physical structures, UC has a higher power density but relatively less energy density comparing with battery, which means UCs can be used to improve ROCOF in a short period of time, and batteries are more suitable for frequency recovery in a longer period. The performance of frequency control can be improved by utilizing the high power density and fast releasing speed of UCs. In this subsection we are going to prove the advantages of UCs over batteries in frequency control. The result will be evaluated by the frequency nadir and the ROCOF. Finally, UCs and batteries are combined in a HESS to compensate their properties.

4.2.1. Performance testament design

In this subsection, UCs and batteries are simulated separately in the same situation of droop and derivative control. The performance of frequency stability control with a 60 MW load increase at bus 8 is tested. In order to fairly judge the performance of batteries and UCs, they should be sized equally,

including their energy storage and terminal voltage.

The energy storage of an UC is calculated as equation 4.1, which is represented as the electric potential energy of stored charges in a RC parallel branch model (figure 3.7).

$$E_{UC} = \frac{1}{2}C_f V_{Cf}^2 + \frac{1}{2}C_d V_{Cd}^2 + \frac{1}{2}C_l V_{Cl}^2 + \frac{1}{3}K_V V_{Cf}^3 \quad (4.1)$$

All the parameter values can be found in table3.2. The last term is the third power of voltage V, because K_V is a voltage-dependant capacitance constant. The total capacitance for branch1 is $C_f + K_V V_{Cf}$. Considering nominal UC voltage is 2.3V, the calculated energy storage in one UC cell is 2331J ($6.475 \times 10^{-4} \text{kw} \cdot \text{h}$).

The battery model used for this simulation is derived from commercial Li-ion polymer battery product TCL-PL-383562, which is a build-in model in RSCAD. Its stored energy can be calculated using its parameters:

$$E_{battery}(100\%SOC) = AH \times V_{rated} \quad (4.2)$$

where the Ampere-Hour of each battery cell is 0.85Ah; The nominal voltage V_{rated} is 3.4V. The calculated battery energy is 10404J (2.89×10^{-3}).

One example of battery size and UC size is shown in table 4.2. The terminal voltage and energy storage of UCs and batteries are sized as the same level. The battery size is slightly larger than UC in order to compensate the errors in simulations.

Table 4.2: Size selection of battery and UC

	N_s	N_p	Terminal Voltage	Energy storage
Battery	900	80	3.45kV	$7.5 \times 10^8 \text{J}$
UC	1500	200	3.42kV	$7 \times 10^8 \text{J}$

4.2.2. Comparison result between UC and battery

The result of UC and battery testament is shown in figure 4.3. At 0.5s, a 60 MW load step increase happens on bus 8. The system frequency starts to drop since rated power generation is lower than load demands. After the frequency derivative decreasing to -0.07HZ/s , the derivative control starts to activate. The frequency drop stops within 2s. During this time, the output of droop control gradually increases to meet the load demand. Finally, power system is stabilized after 4s. Since the setting of droop control is same for battery and UC, the settled system frequency is same for two cases, 49.78HZ. The most significant difference of two cases happens in the first few seconds, because the power density and reacting speed of UC is better than battery. Sufficient power is supplied to prevent frequency change in UC case. The minimum ROCOF of UC is 0.225HZ/s higher than battery data 0.309HZ/s, and UC frequency nadir is 49.753HZ also better than the battery case 49.711HZ. Therefore, this result proves that UC has a better performance especially for derivative control.

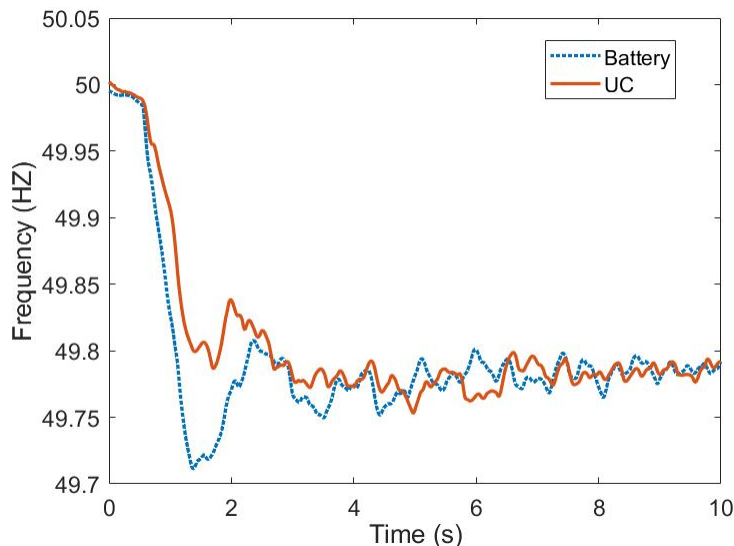


Figure 4.3: Frequency regulated by battery and UC under 60MW load increase

Table 4.3: Result of battery and UC comparison

	Frequency nadir	ROCOF
Battery	49.711HZ	0.309HZ/s
UC	49.753HZ	0.225HZ/s

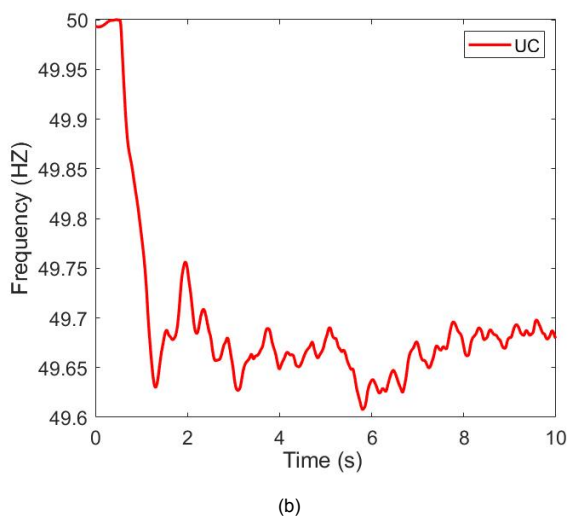
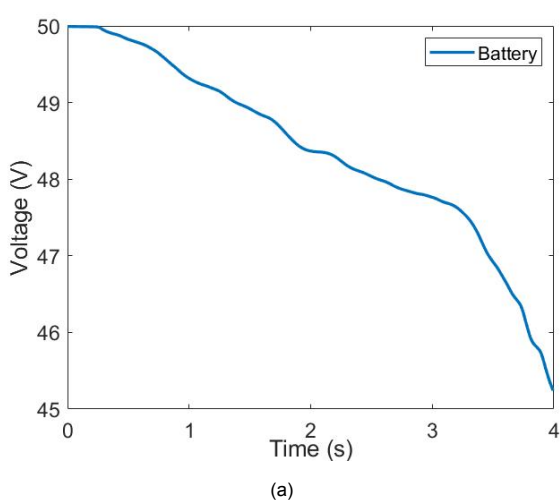


Figure 4.4: (a)Frequency regulated by battery under 84MW load increase, (b) Frequency regulated by UC under 84MW load increase.

Both batteries and UCs are able to withstand a load increase of 60MW. Hence, a severer test is used to distinguish their performance in frequency control. The load demand $L8$ increases to 84MW which is equal to the largest generation in system. This 84MW test in figure 4.4 shows that battery based frequency control cannot withstand this amount of frequency disturbance, because battery has

a relatively lower power density and reacting speed, and frequency drops below the admissible value with a ROCOF of 0.76HZ/s. The synchronization of power system collapses after this disturbance.

In contrast, UCs react immediately after load increase. The ROCOF is improved to 0.458HZ/s. By fast injecting active power to the power system, frequency is stabilized at 49.65HZ with a frequency nadir at 49.60HZ. This result shows the importance to have high power-density component and fast power reacting speed. Although batteries contain large energy density, the power rating is still insufficient for severe frequency disturbance. Building even larger battery storage may solve this problem, but it is uneconomic comparing with UCs. For derivative control, only 30MW·s of energy is released during this period. However, in order to double the power rating, the battery storage also needs to be double sized. The battery will be oversized and most of the stored energy will not be used.

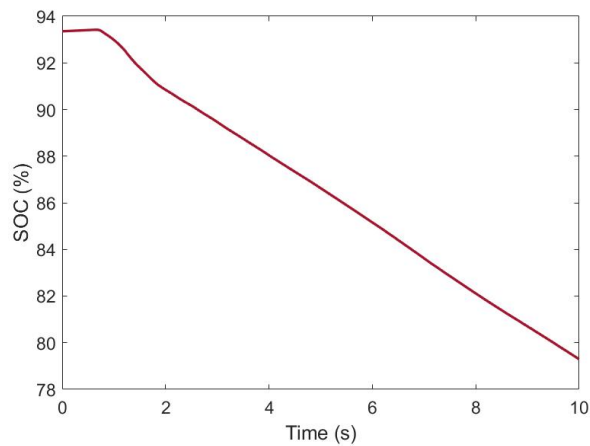


Figure 4.5: UC SOC during frequency regulation

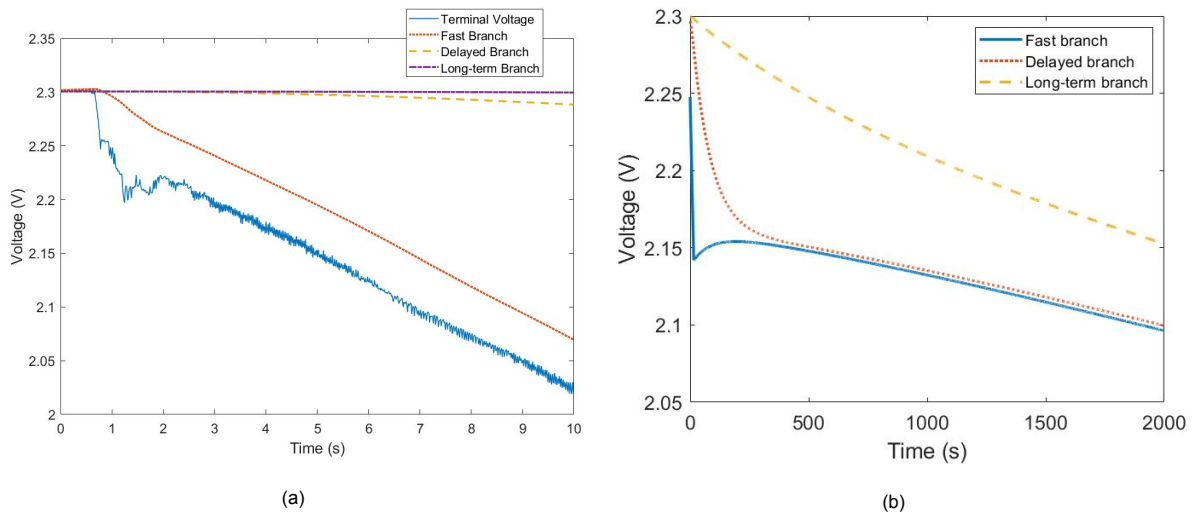


Figure 4.6: (a) UC inner voltages during frequency regulation, (b) UC inner voltages in long term.

The voltage and SOC of an UC is shown in figure 4.5. Around 15% of energy is used for frequency control. In the corresponding 10s, only the fast branch follows the terminal voltage in the first ten seconds as shown in figure 4.6a. Figure 4.6b shows UC voltages appearance in half an hour. The

voltages of fast branch and delayed branch finally become equal at around 500 seconds. The voltage of long-term branch is still chasing after them, and their converge will take even longer time.

The comparison between UC and battery shows that UCs have high power density, and they are able to withstand severer frequency disturbance than batteries. However, batteries contain a higher energy density. For the same size of energy storage, the price for battery is lower than UC. Especially after we know the fact that batteries perform same as UCs for droop control. In order to avoid ESS oversize, UCs are used to improve the power density and reacting speed of the system, and batteries are used to supply bulk amount of energy. A HESS is implemented in this thesis to compensate the benefits of both UC and battery.

4.3. Topology of HESS

The topology of a HESS can be categorized as passive, semi-active and fully-active topologies based on whether the energy source is connected through a power electronic interface[16]. The connection topology of HESS should be determined by the implementation of energy sources.

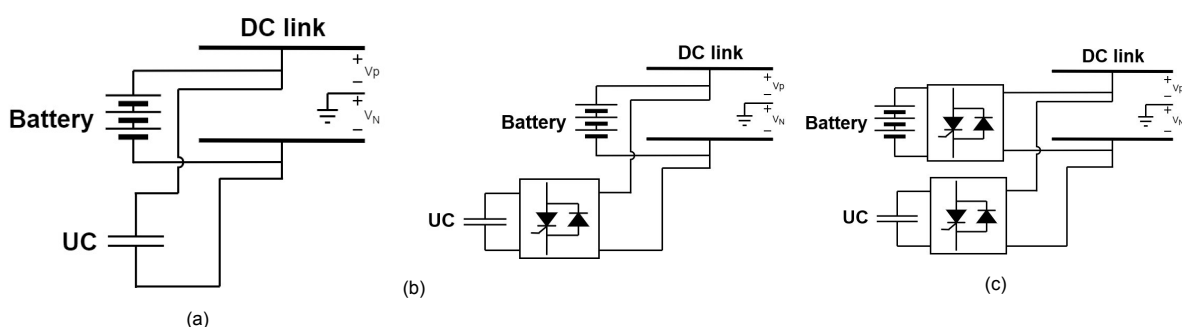


Figure 4.7: (a)Passive topology, (b) semi-active topology, and (c) fully-active topology of HESS.

Passive topology means that all the energy sources are directly connected to the DC-link. The SOC of energy sources determines the voltage of DC-link. This topology is designed for HESS with a separate bus. The advantage is no converter losses. In this thesis, the DC-link is also shared by the wind generator. Since normal operation of wind generator requires a constant DC-link voltage, it is not realistic to have a HESS disturbing the DC-link voltage intensively. Hence, passive topology is not realistic in this thesis.

In contrast, DC converters connected batteries and UCs are easier to control their output voltage. A semi-active topology is a HESS with partially converter connected energy sources. A battery directly connected HESS is battery semi-active topology. A large enough battery pack can keep the DC-link almost constant during each operation of HESS. However, the batteries are directly exposed under the high-frequency current which has a negative impact on battery life. If we swap the position of batteries and UCs, the batteries can be protected by DC converters and controlled to generate only an average value of power demand. However, UCs are limited by the DC-link voltage and not able to response fast to power reference. This contradicts the reason why we are trying to use UC to improve the frequency-control performance.

As a result, the fully-active topology is adopted in this thesis. Batteries and UCs and both connected through buck-boost converters. This topology gives the most control-ability to achieve better performance of HESSs. We can also size battery and UC separately depending on their own applications.

One disadvantage of fully-active topology is more converter losses which is acceptable in this thesis.

4.4. Power Allocation Between UC and Battery

The purpose of power allocation between UCs and batteries is to achieve an operating performance according to control demands. The goal is to quickly react to control reference and extend batteries' life-time. Since batteries and UCs are both connected on the DC-link through DC-DC converters, we can easily control their output by changing duty cycles of buck-boost converters. The total HESS power is separated as a high-frequency component supplied by UC and a slow changing component supplied by batteries. UC controllers react fast to control errors, while battery controllers generate an average value of control reference by damping out high-frequency disturbance. In order to separate the total power reference properly, power allocation methods are discussed in this section.

Power allocation methods in references [11, 16, 31] can be classified as two categories: one is rule based, the other is filter based. The idea of filter-based method can be implement in the case of droop and derivative control. The control signal of derivative control is naturally faster than the droop control. The derivative control first reacts to the frequency derivative, and then droop control gradually responds to the accumulated frequency error. Therefore, extra methods are not needed to separate these power references, and the control signals for UCs and batteries can be properly allocated according to this time sequence. One example is a HESS formed virtual synchronous generator in [11], where UCs emulate fast inertial responds, and batteries conduct a relatively slow droop control. When power system has a step load increase or a generator trip, system frequency drops immediately resulting in an extremely large frequency derivative. Afterwards, frequency slowly approaches its minimum value and settles in a new equilibrium state. During this process, UCs can supply a spike current to increase system inertia, and batteries can deliver a constant power for primary frequency control. As shown in figure 4.8, this HESS can supply necessary system inertia only through UCs without impacts on battery packs, and latter the battery stored energy can regain the system frequency stability. Consequently, droop and derivative control can be naturally adopted as a rule-based allocation method.

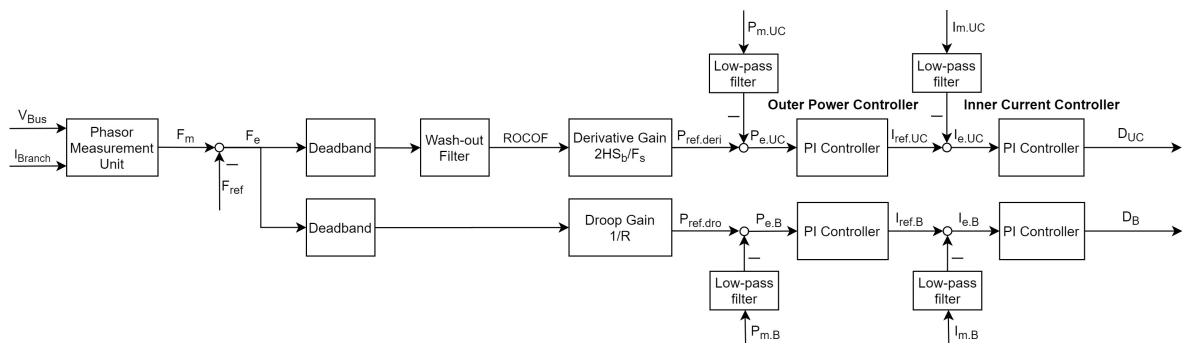


Figure 4.8: Power allocation of droop and derivative control

Filter based methods use frequency as the reference to separate power demand. If we can define a cut-off frequency, then a whole power reference can be separate as fast and slow components. One example is paper [31], a high-pass filter with a cut-off frequency around 2Hz is used to allocate high-frequency power to UCs, and the filtered slowly-changing current will be left to batteries. In experiments, this HESS is connected with a fluctuating demand, and it proves that HESS can meet these demands

without exceeding the limit boundary of battery power variants. If the cut-off frequency of high-pass filter needs to be selected precisely, the bode plot of filter and controllers can be used to search for this value. In conditions with separate controllers for UCs and batteries, the speed of two power sources can also be determined by tuning the natural frequency of two controllers. In [16], controllers are designed to decouple the bandwidth of inner current control loop and outer voltage control loop, by means of analyzing dynamic and steady components of transfer function separately. The result is that inner current control loop react fast to intermittent load current, while outer voltage control loop only supply the average (active) current with a large time constant to maintain the UC voltage at nominal value eventually.

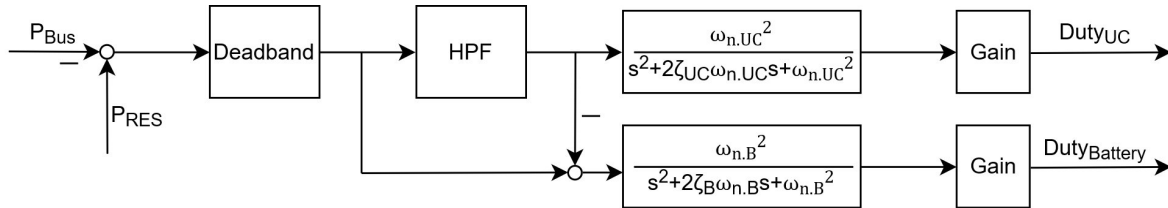


Figure 4.9: Power allocation of VSP

Considering our application with VSP, where power reference comes from power difference, an explicit high-pass filter are used to allocate the total power reference to batteries and UCs. When load increase happens, the power gap arises immediately as the power reference. This step change will be allocated to UCs for the fast response speed. In contrast, batteries are protected from peak current and slowly take over the responsibility of power reference. The ideal condition is that UCs only generate the power demand at the first one second and gradually returns to zero. However, the high-frequency disturbance from high-pass filter is easy to be amplified as oscillations in the power grid. The solution is tune the bandwidth of UC controller. The natural frequency of transfer function should be at least two times lower than oscillations. For example, when a disturbance around 2HZ is input as a power reference, a high-pass filter has time constant higher than 2HZ cannot block this disturbance leading to UC output power with oscillations. Selecting a natural frequency ω_n of second-order control loop lower than 0.5HZ can damp this disturbance.

4.5. Energy Storage Sizing

The sizing of ESS decides the number of series and parallel elements as in figure 3.11, which directly determines ESS parameters including terminal voltage, equivalent series resistance and stored energy. These parameters are highly related with the performance of an ESS. Energy storage sizing also determines the construction cost of ESS. Some design of ESS may provide a good performance but leading to a less economic cost which is not realistic. In this section, the influence of energy sizing is discussed considering the requirements of maximum power, stored energy, efficiency and the cost constraint.

4.5.1. Power Requirements of frequency stability control

The power requirements are determined by power allocation methods from last section. The power capability of HESS should be at least larger than these requirements.

First, let us think about droop and derivative control. The drop control determines the settling state of

system frequency which should be higher than the admissible frequency 49.2HZ. The derivative control migrates the ROCOF to an acceptable level by reducing the power gap of synchronous generators. This threshold for ROCOF should prevent system frequency collapse before droop control is activated. The theoretical power output of droop and derivative control is expressed in equation 2.5.

In order to determine the maximum values of the two power demands, the severest condition is considered as a 84MW load increase which is equal to the largest generation in the system. FDWGs on bus 7 and bus 9 supply twice of the active-power frequency response. Hence, the actual load for each FDWG is half of the total amount. Droop control determines the settled frequency value which should be always above the admissible frequency 49.2HZ. Therefore the maximum output of droop control should be larger than the severest load demand 84MW. The frequency droop is calculated as

$$P_{droop} = 2 \cdot \frac{1}{R} \cdot \Delta f_{max} > \Delta P_{L,max} \quad (4.3)$$

where the maximum frequency error is $(50 - 49.2) = 0.8\text{HZ}$; the maximum power variation $\Delta P_{L,max}$ is 84MW in this case. The calculated frequency droop R is in range $R < 0.019\text{HZ/MW} = (49.97 - 49,951)\text{HZ/MW}$.

The derivative control determines system inertia and ROCOF during frequency control. Normally, the derivative control works in the first 1-2 seconds, and later droop control will operate to supply the load demand. The limit of ROCOF is selected as 0.4HZ/s, because setting the tripping threshold of ROCOF relays as 0.4HZ/s improves relays' stability[32].

$$H_{sys} = \frac{\Delta P_{L,max}}{S_b} \cdot \frac{F_b}{\max(df/dt)} \quad (4.4)$$

Based on swing equation 4.4, the required system inertia is 16.67s. In equation 4.4, S_b is the nominal total generation 315MW; F_b is nominal power system frequency 50HZ; the maximum frequency derivative $\max(df/dt)$ is ROCOF 0.4HZ/s. However, the calculated system inertia needs to be transferred to the inertia setting for FDWGs. The original system inertia without frequency stability control is calculated by measuring the ROCOF of a series of load increases. The data is listed in table 4.4. The average of H_{sys} is 4.82s which is consider as the natural inertia of power system.

Table 4.4: Inertia of the modified IEEE 9 bus system without frequency control

ΔP (MW)	ROCOF (HZ/s)	$H_{sys} = \frac{\Delta P \cdot f_s}{2(df/dt \cdot S_{sys})}$ (s)
-5	0.080	4.94
-7	0.115	4.87
-10	0.166	4.77
-12	0.200	4.83
-15	0.242	4.90
-17	0.274	4.92
-20	0.342	4.65

The inertia setting for FDWG is calculated as the required system inertia deduct the existed natural inertia. The basement power should be transferred from system generation to FDWG generation in equation 4.5. Finally, the calculated virtual inertia of FDWG is 22.76s.

$$H_{FDWG} = \frac{1}{2} \cdot (H_{sys.design} - H_{sys.natural}) \cdot \frac{S_{sys}}{S_{FDWG}} \quad (4.5)$$

The power reference in droop and derivative control is a global value, although two FDWGs are located at bus 7 and bus9. However, for VSP, power reference is highly related with power distribution. When load 8 increases 84MW, power flow P_{78} from bus 7 increases from 82MW to 130MW, and load flow P_{98} from bus 9 increases from 20MW to 56MW. Then the VSP requirements for WG1 and WG2 are 48MW and 36MW respectively.

4.5.2. Calculation of HESS power output

The HESS is connected on DC-link through a buck-boost converter shown in figure 4.10. The output current is controlled by duty cycles of the buck-boost converters. In order to know which size of HESS is capable to supply enough power, the maximum output power of buck-boost converter is studied.

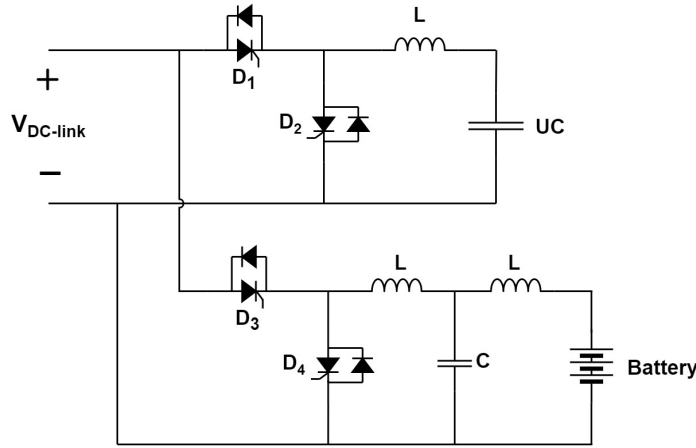


Figure 4.10: Buck-boost converter connecting HESS with DC-link

In order to simplify the calculation and only focus on the power output of buck-boost converters, UCs and batteries are represented by voltage sources in series with equivalent resistors in the following calculations. Then the power calculation procedures of UC and battery are same. UC power calculation is analyzed as an example.

According to the structure of UC based ESS in figure 3.11, the total voltage, current and resistance can be determined by ESS size as following equations

$$\begin{aligned} V_{UC}(t) &= N_s \times V_{cell}(t) \\ i_{UC}(t) &= N_p \times i_{cell}(t) \\ R_{ESR} &= \frac{N_s}{N_p} \times R_{cell} \end{aligned} \quad (4.6)$$

where $V_{UC}(t)$ is the terminal voltage of UC ESS; R_{ESR} is the equivalent series resistance of UC ESS; N_s and N_p are the number of series and parallel UC cells; $V_{cell}(t)$, $i_{cell}(t)$ and $R_{cell}(t)$ are values of one UC cell.

By considering UCs as one voltage source, the output power through a boost converter is easy to represent as

$$P_{output} = V_{dc-link} \cdot ((1 - D) \cdot i_{UC}) \quad (4.7)$$

The UC current i_{UC} also equals to the inductive current i_L on UC side. For a certain duty cycle D , the output power is proportional to the inductive current i_L . Therefore, maximum output power is achieved when inductive current reaches its maximum value. During this period, the DC-link voltage is constant 4kV. The change of inductive current is determined by the integral of voltages over it in one period.

$$\Delta i_L(t + T) = \int_t^{t+DT} (V_{UC}(t) - R_{ESR} \cdot i_L(t)) dt + \int_{t+DT}^{t+T} (V_{UC}(t) - R_{ESR} \cdot i_L(t) - V_{dc-link}) dt \quad (4.8)$$

At the beginning, the inductive current increases from zero. After some time, it reaches its maximum. According to the equation 4.8, the maximum inductive current is reached when its increment $\Delta i_L(t + T)$ becomes zero. By taking the derivative of equation 4.8 and making it equal zero, the duty cycle of maximum power is calculated in equation 4.9.

$$\begin{aligned} (1 - D) \cdot V_{dc-link} &= v_{UC}(t) - R_{ESR} \cdot i_L(t) \\ \Rightarrow D &= \left(1 - \frac{V_{UC}}{V_{dc-link}}\right) \end{aligned} \quad (4.9)$$

The theoretically maximum output power is

$$P_{output.max} = \frac{V_{UC}^2}{4R_{ESR}} \quad (4.10)$$

In the condition that UC voltage equals 2.3kV, the maximum output power is 84.94MW when duty cycle equals 0.7125. However, in real measurement the maximum power is less than 80MW, because the terminal voltage of UCs decrease very fast even in 1-2 seconds. According to measurement, the UC voltage decrease could be 0.232kV when maximum output power is achieved and duty cycle equals 0.7125. Therefore, the real maximum power measured is 77.31MW lower than the theoretical value. The relationship between output current and UC voltage decrease can be expressed in differential equations 4.11. The numerical solutions are calculated in MATLAB to find the maximum output power and the corresponding duty cycle.

$$\begin{aligned} \frac{di_{UC}(t)}{dt} &= \frac{1}{L} (V_{UC}(t) - R_{ESR} - (1 - D) \cdot V_{dc-link}) \\ \frac{V_{UC}(t)}{dt} &= \frac{i_{UC}(t)}{(C + K_v V_{UC}(t))} \end{aligned} \quad (4.11)$$

The result of MATLAB in figure 4.11 shows the maximum output power is 77MW when duty cycle is around 0.71, which is very close to the result of real-time simulations 77.31MW at duty cycle 0.7125. This result is for UCs with a size of 1000 × 200. In next subsection, a series of UC sizes are tested to find the maximum output power. Meanwhile, the corresponding duty cycle and efficiency are considered.

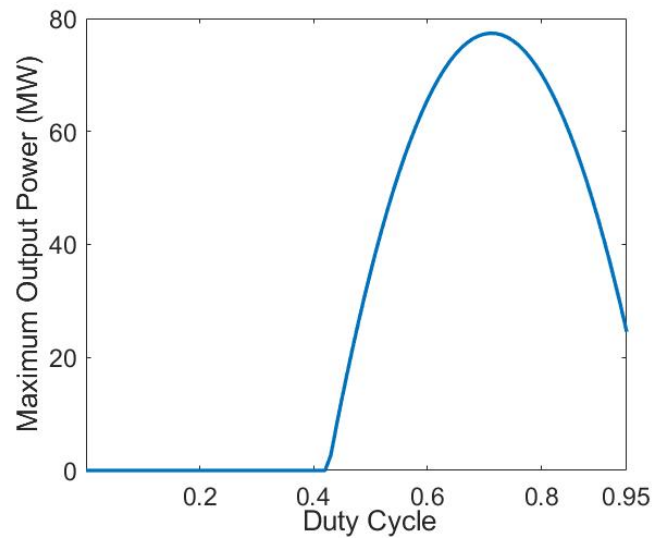


Figure 4.11: Maximum output power of UC changing with duty cycles (Continuous mode)

4.5.3. Influence of energy storage sizing

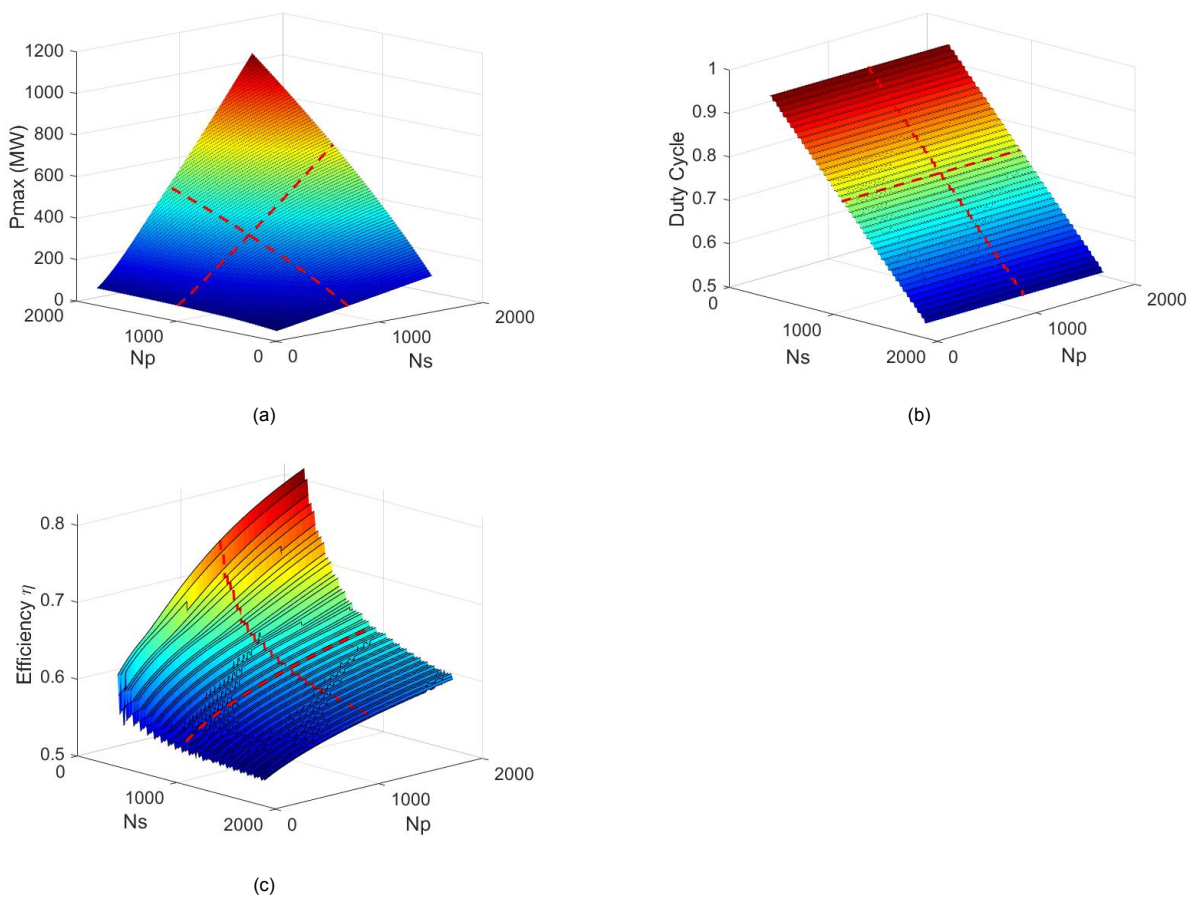


Figure 4.12: (a) Maximum output power, (b) duty cycle at the maximum power point and (c) efficiency at the maximum power point changing with the size of UC.

In this subsection, ESS sizing not only optimize the power output, but also consider the economy of ESS. Apparently over-sizing the ESS or low efficiency is uneconomic in real applications. Figure 4.12a shows the maximum output power changing with UC size. Apparently, the maximum output power increases with the size of UCs. However, in the most of cases of figure 4.12, the output power of UC is way larger than our actually needs. The duty cycle for maximum power point is dominantly influenced by the series number of UCs which also means the terminal voltage of ESS. However, equivalent series resistance also increases with the series number of UCs, which directly increases the resistive losses. As shown in the figure 4.12c, efficiency is lower when series number increases. When parallel number decreases, the efficiency is even lower only around 50%. Therefore, it is better to operate UC ESS in a state where the duty cycle is lower than the maximum power point. On the one hand, lower duty cycle can improve the ESS efficiency but requires a larger size of UC ESS. On the other hand, a smaller ESS can save more construction cost. In order to find the minimum size of UC ESS with an acceptable efficiency supplying sufficient power, an efficiency constraint is imposed on maximum power searching.

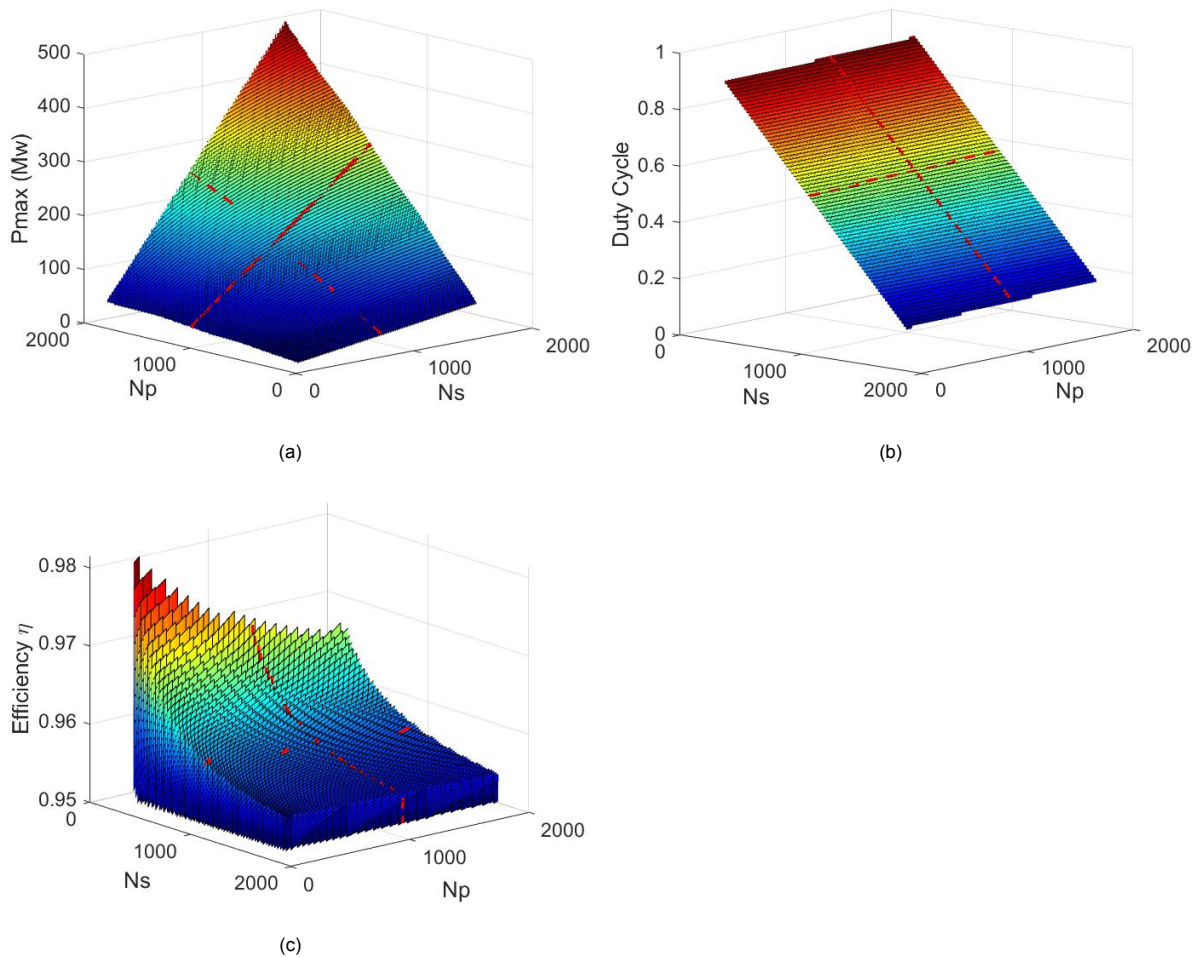


Figure 4.13: (a) Maximum output power, (b) duty cycle at the maximum power point and (c) efficiency at the maximum power point changing with the size of UC, when efficiency is required higher than 90%.

Figure 4.13 show the modified curves of maximum power and duty cycle with efficiency higher than 0.95. P_{max} is the maximum output of UCs complying to the efficiency limit 0.95; duty cycle and efficiency are recorded when maximum power is reached. The maximum output power is lower than half of the

original value, and the duty cycle when maximum power is achieved is also decreased. As a result, the preferred size of an ESS is larger than its power capability. In next chapter, an optimization problem is formed to find the optimal solution for HESS sizing.

4.6. Summary for Power Allocation and HESS Sizing

In this modified IEEE 9 bus system, 52% of generation is replaced by FDWGs. Extra power injections are required to enhance the frequency stability of power system. UC and battery combined HESSs are adopted as a good solution for fast active power-frequency control of FDWGs. On the one hand, UCs have high power density and fast reacting speed, which can improve the fast active power-frequency response. On the other hand, batteries have higher energy density and lower price, which is suitable to extend the duration of power supply. Meanwhile, UCs can work in severer situations including rapid changing current, wide temperature range, etc. Hence, UCs can supply a fast power spike and leave the slowly average power to batteries to extend batteries' lifetime.

In order to achieve the designed HESS performance, HESS topology and power allocation methods are studied. A fully-active topology is selected to achieve better controllability of battery and UC. Power reference of derivative control and droop control is allocated to UC and battery naturally. In contrast, a high-pass filter is used to allocate the fast component of power reference of VSP to UCs.

Finally, the influence of HESS sizing is studied. The maximum power changing with HESS size is recorded. However, the duty cycle, when maximum power is reached, also influences the efficiency of HESS. In some situations, the HESS is only around 0.5. In order to increase HESS efficiency above 0.95. The duty cycle of buck boost converter is decreased to reduce the current value. In next chapter, an optimization problem about HESS sizing is formulated to find the most suitable HESS size which provides sufficient power and meanwhile has an acceptable efficiency.

5

Mean-variance Mapping Optimization of Droop and Derivative Control and VSP

In last chapter, we discussed the establishment of HESSs and how the power of HESSs can supply sufficient power for frequency stability control. By implementing the HESS based frequency stability control, the frequency stability performance trading off with HESS construction cost becomes an optimization problem. In this chapter, a mean-variance mapping optimization (MVMO) algorithm is used to find the optimal parameter settings for droop and derivative control and VSP and optimal HESS sizing. The objective of optimizing these two frequency stability control methods is to answer the research question 3 (To which extent can these methods improve power system frequency?). The optimization results are used to compare two frequency control methods.

5.1. Formulation of the Optimization Problem

The optimization formulation of frequency stability control and HESS sizing is consider as four aspect:

1. The objectives of frequency stability control should not be violated. The indicators selected for power system frequency are frequency nadir and ROCOF as equation 2.3 and 2.4. ROCOF describes the maximum varying speed of frequency which reflects power system inertia. Frequency nadir f_{nadir} is severest frequency value. If the frequency nadir is kept in the safe region of frequency, then the frequency stability is sufficiently protected during load disturbance. In the analysis of the IEEE 9 bus system shown in figure 4.1, the limits of frequency nadir and ROCOF is given as 49.2HZ and 0.4HZ/s. In order to ensure the normal operation of power system, frequency stability control should fulfill the constraints of frequency nadir and ROCOF.
2. HESSs are the power sources selected for frequency stability control. The power capability of HESSs directly influences the performance of frequency control. However, oversized HESSs are uneconomic and unrealistic in real applications. Therefore, optimization searches for the minimal size of HESSs that fulfill frequency stability constraints.

3. Power losses is one of the operational cost that should be considered in energy sizing and frequency controller design. As shown in the result of chapter 4, a HESS has a low efficiency close to 0.5 when maximum output power is achieved through a buck-boost converter. In order to improve HESS efficiency, equivalent series resistance should be reduced. Decrease the output current can also reduce the resistive losses. The equivalent series resistance of a HESS is described in equation 4.6. The current is related with the duty cycle output from frequency controllers and HESS terminal voltage. Therefore, the HESS size and controller parameters should all be regulated by efficiency constraints.
4. Last but not least, the battery life-time is influenced by the changing rate of current. Batteries should be protected from high-frequency current. A measurement of high-frequency current magnitude should be designed. Parameters of frequency controllers should be supportive to mitigate the changing rate of battery current.

Considering these four goals, an optimization problem is formulated as equation 5.1. The requirements on frequency control, HESS efficiency and changing speed of battery current can be written as optimization constraints. Then the objective function is the construction cost of HESS. The objective of optimization is to fulfill all these constraints with a minimized HESS construction cost.

$$\text{Minimize } OF(\mathbf{x}) = \text{HESS Cost} \quad (5.1)$$

subject to

$$g_1(\mathbf{x}) = (f_{nadir.min} - f_{nadir}) < 0 \quad (5.2)$$

$$g_2(\mathbf{x}) = (ROCOF.max - ROCOF) < 0 \quad (5.3)$$

$$g_3(\mathbf{x}) = (\eta_{HESS.min} - \eta_{HESS}) < 0 \quad (5.4)$$

$$g_4(\mathbf{x}) = (|I_{batt.DC}.min - |I_{batt.DC}|) < 0 \quad (5.5)$$

The objective function $OF(\mathbf{x})$ is formulated by HESS cost which is consider as an opposite value to the frequency control performance. The overall objective of optimization is to improve the frequency response by minimizing ROCOF and frequency nadir f_{nadir} , and also avoid oversized HESS wasting more investment than actual demand.

The HESS cost is calculated as function 5.6 which can be further divided into UC cost and battery cost. The UC price and battery price are selected as 200\$/kw.h and 500\$/kw.h according to currently primary cost assumptions[33] [6]. The energy stored in one cell of fully charged battery and UC are 10404J($2.89 \times 10^{-3}kw.h$) and 2331J($6.475 \times 10^{-4}kw.h$) respectively according to equation 4.1 and 4.2.

$$\begin{aligned}
UC \text{ Cost} &= N_{s,UC} \times N_{p,UC} \times UC \text{ price } (\$/kw.h) \times UC \text{ energy } (kw \cdot h \text{ per cell}) \\
Battery \text{ Cost} &= N_{s,B} \times N_{p,B} \times battery \text{ price } (\$/kw.h) \times battery \text{ energy } (kw \cdot h \text{ per cell}) \\
HESS \text{ Cost} &= UC \text{ cost} + Battery \text{ cost}
\end{aligned} \tag{5.6}$$

Constraint g_1 is the admissible frequency nadir. The admissible frequency $f_{nadir.min}$ of the IEEE 9 bus system is selected as 49.2HZ according to [34]. The power system is under the risk of collapse with a lower frequency value.

Constraint g_2 is the upper limit of ROCOF. As calculated in equation 2.3, ROCOF is determined by the magnitude of load change and overall inertia of power system. When a load increase equals to the maximum generation, the upper limit of ROCOF is 0.4HZ/s as calculated in [35] and the system inertia should be above 16.67s as calculated in 4.5.1.

Constraint g_3 limits the efficiency of HESS η_{HESS} . The result of chapter 4 shows methods to improve HESS efficiency. A lower efficiency limit $\eta_{HESS.min}$ is selected as 0.95 according to [19]. On way is decreasing the duty cycle of buck boost converters, which leads to a low output current and reduces the resistive losses. However, the output power is reduced. If we want to improve HESS efficiency and meanwhile increase the power output, the parallel number of HESS elements should be increase to reduce equivalent series resistance and increase output current. The efficiency of batteries and UCs should be considered separately.

The last constraint g_4 is on the high-frequency component of battery current. A slowly changing battery current is helpful to extend batteries' life-time. In order to protect batteries from high-frequency current, frequency components of battery current should be analyzed. One example is shown in figure 5.1. Figure 5.1a is a current curve of 900×300 sized batteries. Figure 5.1b is the Fourier transformed histogram of this battery current, and most of battery current is DC component. However, there are still some magnitudes from high-frequency disturbance. In this case, 75% of total magnitudes are located at the left side of 1.599HZ marked as red dashed line in figure 5.1b. We can slow down the changing of battery current by limiting the magnitudes of high-frequency components during optimizations. The lower threshold for direct current component is selected as the 75% of total current magnitudes, which stands for the majority of frequency components[36]. Therefore, the limit of battery DC current is defined as 75% of total magnitudes in equation 5.7.

$$|I_{batt.DC}|_{min} = 0.75 \times sum(I_{batt}(allfrequency)) \tag{5.7}$$

As an optimization constraint, the frequency of 75% battery current magnitudes is analyzed in every iteration. If high-frequency oscillations happen during optimizations, this constraint will penalize the optimization fitness and modify the controller parameters to damp out disturbance. Normally, the natural frequency of second-order system should be twice smaller than disturbance frequency, so that the disturbance will not be amplified. Any cases with a peak current or high-frequency oscillations will be avoided when frequency components of battery current is checked. With this constraint, system will prefer to slow down the battery controllers and to increase the time constant of high-pass filters.

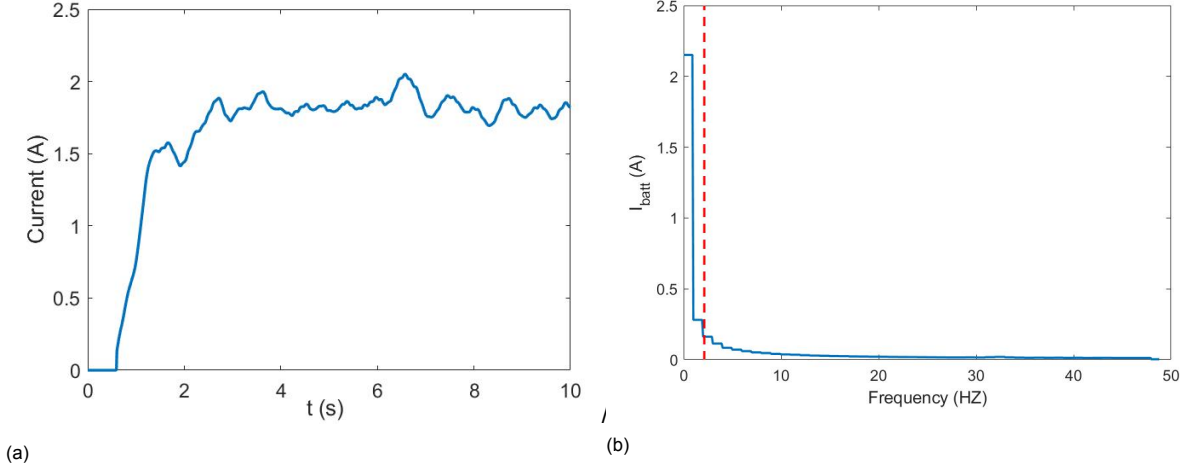


Figure 5.1: (a) Battery current, (b) frequency component analysis of battery current.

As summary, the controller parameters and HESS size should be optimized to fulfill these constraints. The HESS size includes the series and parallel numbers of batteries and UCs ($N_{s.UC}$, $N_{p.UC}$, $N_{s.B}$ and $N_{p.B}$). As described in equation 4.6, series numbers ($N_{s.UC}$, $N_{s.B}$) determine the terminal voltage of batteries and UCs; parallel numbers ($N_{p.UC}$, $N_{p.B}$) determine their current and series resistance. Therefore, these four size numbers should be considered as optimization variables.

On the other hand, controllers for droop and derivative control and VSP have different structures. For droop and derivative control, the power reference is calculated according to virtual inertia H_{FDWG} and frequency droop R . PI controllers are used to control the power and current of HESSs, hence the parameters of PI controllers are also chosen as optimization variables, including proportional gain and integral gain of outer power controllers of UCs ($K_{P.p.UC}$, $K_{I.p.UC}$), inner current controllers of UCs ($K_{P.i.UC}$, $K_{I.i.UC}$), same for PI controllers of batteries ($K_{P.p.B}$, $K_{I.p.B}$, $K_{P.i.B}$, $K_{I.i.B}$). These gain values should be tuned well to give a fast active-power frequency response speed and avoid noise signals in the control system.

For VSP, the power reference comes from the power difference in equation 2.6, so no extra parameters are needed to generate the power reference. However, high-pass filters are used to allocate power references to batteries and UCs. The cut-off frequency T_{HPF} should be selected as one optimization variable to tune the output power allocation between batteries and UCs.

The controllers of VSP is formed by second-order control loops. Therefore, parameters of second-order functions play an important role in reacting speed and damping noise signals. The natural frequency, damping factors and gains of second-order control loops should be selected, including $\omega_{n.UC}$, $\omega_{n.B}$, ζ_{UC} , ζ_B , K_{UC} and K_B . In VSP, high-pass filters are used to allocate power references, so the time constant of high-pass filter T_{HPF} is also an optimization variable.

The total optimization vectors for droop and derivative control and VSP are listed below:

Droop and derivative control (14 variables):

$$\mathbf{x} = [N_{s.UC}, N_{p.UC}, N_{s.B}, N_{p.B}, H_{FDWG}, R, K_{P.p.UC}, K_{I.p.UC}, \dots \\ \dots K_{P.i.UC}, K_{I.i.UC}, K_{P.p.B}, K_{I.p.B}, K_{P.i.B}, K_{I.i.B}] \quad (5.8)$$

VSP (11 variables):

$$\mathbf{x} = [N_{s,UC}, N_{p,UC}, N_{s,B}, N_{p,B}, \omega_{n,UC}, \omega_{n,B}, \zeta_{UC}, \zeta_B, K_{UC}, K_B, T_{HPF}] \quad (5.9)$$

As a result, 4 constraints are implemented in this thesis to limit the frequency, ROCOF, efficiency and current disturbance. The objective function is designed to improve frequency performance and to save more HESS cost. The optimization tunes 14 variables for droop and derivative control and 11 variables for VSP.

The HESS size ($N_{s,UC}, N_{p,UC}, N_{s,B}, N_{p,B}$) as optimization variables are integer numbers. Therefore, this optimization is a mixed-integer problem. Besides, the constraints are non-convex, because the order of frequency controller is lower than power system order [37]. For classical optimization algorithms like interior point methods, problem needs to be transferred to a convex and smooth optimization problem, which is difficult for this complicated system. In order to solve this mixed-integer, non-convex problem, the mean-variance mapping optimization (MVMO) method as one of the evolutionary algorithms is applied in this thesis.

5.2. Mean-variance Mapping Optimization

MVMO is one of the evolutionary algorithms. It has the ability to evolve optimization variables to produce a better performance in the optimization problem. The update of optimization variables is achieved by a mean-variance mapping method. The mean value and variance of n-best optimization variables are calculated to guide the generation of new variables in the next trails, which ensures the solution evolves to the direction of better performance.

The flowchart of MVMO algorithm is shown in figure 5.2. The optimization starts with randomly initialized D-dimensional variables $\mathbf{x}_0 = [x_1, x_2, \dots, x_D]$. The values of variables are between user defined boundaries \mathbf{x}_{max} and \mathbf{x}_{min} same for the updated variables, so that variable values are always accessible and valid. New variables are normalized as equation 5.10 to guarantee offspring generation between 0 and 1. No extra constraints or penalization rules are needed for variable generation.

$$\mathbf{x}_{nor} = \mathbf{x}_{min} + \frac{\mathbf{x}}{\mathbf{x}_{max} - \mathbf{x}_{min}} \quad (5.10)$$

In our applications, the generated D-dimensional variables \mathbf{x} are same as the optimization variables defined in equation 5.8 and 5.9. The fitness of a set of optimization variables \mathbf{x} should be defined according to optimization problem formulated as equations 5.1, 5.2, 5.3, 5.4, 5.5. The values of frequency, ROCOF, efficiency and battery current should be measure during power system simulations. The power system for simulations is the IEEE 9 bus system defined in subsection 4.1. In every trail of optimization, new variables are used to simulate the frequency stability control results which is then evaluated by fitness values.

The fitness of optimization variables is evaluated by summing the user defined objective function and constraint penalties. The fitness is minimized during the optimization. The equation for fitness calculation is given as 5.11, where $OF(\mathbf{x})$ is the objective function value of optimization vector \mathbf{x} ; n_{con} is the total number of constraints; λ_i is the penalty constant of i-th constraint violation; $g_{i,nor}$ is the normalized value of i-th constraint, which is defined as equation 5.2. The penalty of constraints are selected much larger the objective function $OF(\mathbf{x})$, so that optimization algorithm will give priority to satisfy constraints than to minimize the objective function.

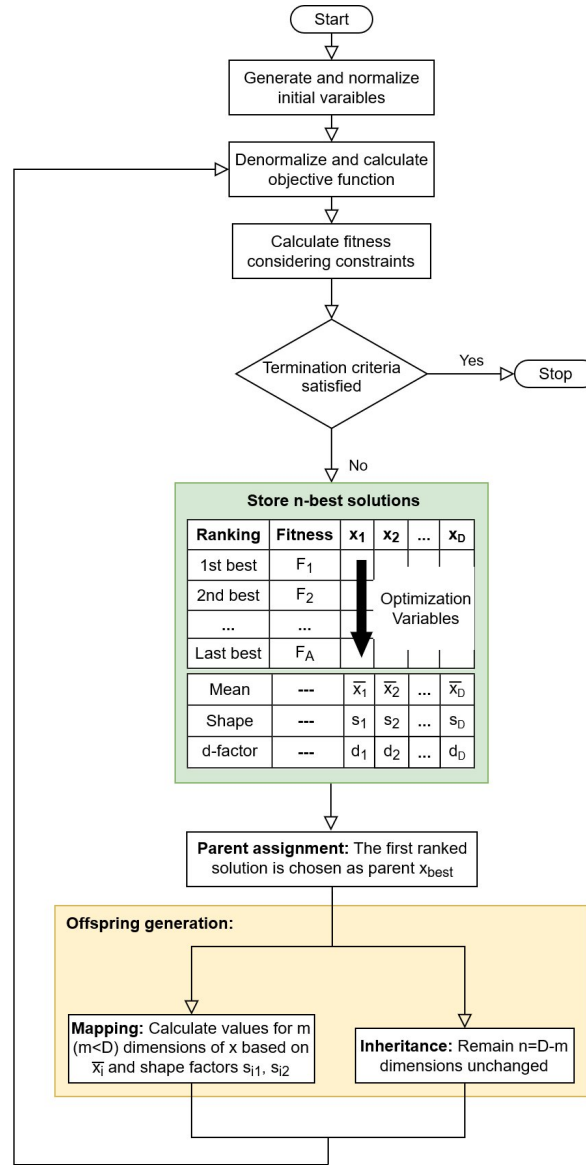


Figure 5.2: The flowchart for the MVMO algorithm procedures

$$\text{Minimize Fitness} = OF(\mathbf{x}) + \sum_{i=1}^{n_{con}} (\lambda_i g_{i.nor}(\mathbf{x})) \quad (5.11)$$

$$g_{i.nor}(\mathbf{x}) = \min \left[1, \max \left[0, \frac{g_i(\mathbf{x})}{g_{i.max}} \right] \right] \quad (5.12)$$

The purpose of constraint normalization is to fairly penalize constraints with different units. $g_{i.max}$ is the limit of i -th constraint. For example, in ROCOF constraint, the limit $g_{i.max}$ equals to admissible ROCOF 0.4HZ/s. It is worth to mention, $g_i(\mathbf{x})$ is formulated as the canonical form in equation 5.3, so that $g_i(\mathbf{x})$ represents the difference between the value of constrained formula and limit $g_{i.max}$. Normalized constraint $g_{i.nor}$ has a value between 0 and 1. When i -th constraint is satisfied, $g_{i.nor}$ always equals to 0. The penalty $\lambda_i g_{i.nor}(\mathbf{x})$ depends on the severity of constraint violation with a maximum penalty of λ_i . Less penalty value is applied when $g_i(\mathbf{x})$ is closer to 0. Comparing with the constraint penaliza-

tion method with binary $g_i(\mathbf{x})$, a continuous $g_i(\mathbf{x})$ is beneficial to the converging speed of optimization, because the latter gives the distance to the feasible solutions.

$$\begin{aligned} \text{Equality constraint : } g_i(\mathbf{x}) &= 0 \\ \text{Inequality constraint : } g_i(\mathbf{x}) &\leq 0 \end{aligned} \quad (5.13)$$

An archive is used to store n-best solutions during the optimization. The solutions (optimization variables) are ranked according to calculated fitness. The depth n of an archive is user defined which influences the converging speed of optimization. Only the latest n-best solutions are stored in the archive. When a new solution \mathbf{x}_{new} is generated with a smaller fitness than any existed solutions, it will be placed in archive according to its fitness rank comparing with other existed solutions, and the last ranked solution will be discarded from the archive. The archive keeps updating during iterations. The finally first ranked solution will be chosen as the optimal solution. An optimization with more variables may need a larger archive. In this thesis maximum 14 variables are optimized, after several testaments, the archive depth is chosen with a good convergence as 15.

The n-best solutions stored in archive is used to generate the offspring variables \mathbf{x}_{new} in the next iterations. The mean and variance values of n-best solutions are calculated as equation 5.14 and equation 5.15, where \bar{x}_i and var_i are mean and variance of i-th variable; j means j-th best solution \mathbf{x}_j . The mean and variance of n-best solutions in archive will participate in offspring generation and guide the mapping from parent variables x_{best} to offspring variables.

$$\begin{aligned} \bar{\mathbf{x}} &= [\bar{x}_1, \bar{x}_2, \dots, \bar{x}_D] \\ \bar{x}_i &= \frac{1}{n} \sum_{j=1}^n x_{j,i} \end{aligned} \quad (5.14)$$

$$\begin{aligned} var(\mathbf{x}) &= [var_1, var_2, \dots, var_D] \\ var_i &= \frac{1}{n} \sum_{j=1}^n (x_{j,i} - \bar{x}_i)^2 \end{aligned} \quad (5.15)$$

Besides, a shape factor and a d-factor are defined and updated with iterations. The shape factor is calculate as a function of variance as below

$$\begin{aligned} s_i &= -\ln(var_i) \cdot f_s \\ f_s &= \frac{n_{itera}}{n_{MaxItera}} (f_{s.end} - f_{s.start}) + f_{s.start} \end{aligned} \quad (5.16)$$

where f_s is the scaling factor. User can define its initial $f_{s.start}$ and final value $f_{s.end}$, so that optimization algorithm can automatically increase archive members' influence offspring generation. The archive members have little influence at the beginning, and therefore $f_{s.start}$ is selected as 1. The final scaling factor has a range between 1 and 50. In this thesis, $f_{s.end}$ is selected as 10 which gives a good converging speed.

The d-factor also has a user defined initial value d_{start} and variation Δd . Starting from d_{start} , every iteration d_i times variation Δd when d-factor is smaller than shape factor, or its inverse $\frac{1}{\Delta d}$ when d-factor is larger than shape factor. The decision making is shown in equation 5.17. The result is d-factor keeps oscillating around current shape factor s_i . The variation step Δd is selected as 0.25 which gives a good converging speed.

$$\begin{aligned} d_i &= d_i \times \Delta d, & s_i > d_i \\ d_i &= d_i / \Delta d, & s_i < d_i \end{aligned} \quad (5.17)$$

A new set of optimization variables are generated by mapping the current best solution \mathbf{x}_{best} in archive before the next iteration. The mapping function is determined by shape factor, d-factor and mean value as equation 5.18.

According to shape factor and d-factor, the mapping function of i-th dimension of optimization variables can be calculated as

$$\begin{aligned} h(\bar{x}_i, s_1, s_2, x_{i,best}) &= \bar{x}_i \cdot (1 - e^{-x_{i,best} \cdot s_1}) + (1 - \bar{x}_i) \cdot e^{-(1-x_{i,best}) \cdot s_2} \\ s_1 &= s_i, s_2 = d_i, \text{ when } rand \geq 0.5 \\ s_1 &= d_i, s_2 = s_i, \text{ when } rand < 0.5 \end{aligned} \quad (5.18)$$

The factors s_1, s_2 of mapping function has 50% of possibility to be equal to shape factor s_i or d-factor d_i . This mapping function determines the offspring generation according to equations

$$\begin{aligned} x_i &= h_x + (1 - h_1 + h_0) \cdot x_i^* - h_0 \\ h_x &= h(x_i = x_i^*), h_0 = h(x_i = 0), h_1 = h(x_i = 1) \end{aligned} \quad (5.19)$$

where x_i is i-th dimension of offspring generation \mathbf{x}_{new} ; x_i^* is a randomly generated number between [0,1]. It is worth to mention both new and old values are normalized according to equation 5.10 during the offspring generation. As a result, best solution \mathbf{x}_{best} is used as parent to generate offspring variables. The optimization updates the archive and factors during iterations, and gradually the local optimal solution in archive will converge to the global optimal point.

There is a dimension selection strategy before variable mutation. Not all the variables are mutated in every iteration. Instead, only m dimensions of n variables are updated. The benefit of this strategy is increasing the converging speed of optimization. The number of mutation dimensions m also updates with iterations. The updating speed of m is defined every $n_{m.freq}$ iterations. User can define the initial and final number of m. The m dimensions of optimization variables for mapping are selected randomly before offspring generation. The other n-m dimensions will remain same as the values of best solution \mathbf{x}_{best} . Normally, the initial value m_{start} is larger than the final value m_{end} . Consequently, more dimensions of optimization variables are mutated at the beginning, and later, only several non-optimal dimensions of variables are selected for mapping, which will help optimization concentrate on important targets and save more optimization time. The m_{start} is selected equal to variable dimension 11 or 14 in two frequency control cases, and the end value m_{end} is 1. The updating speed $n_{m.freq}$ of dimension m is selected as maximum iteration number divided by 20 which equals to around 23.

5.3. Communication between MATLAB and RSCAD

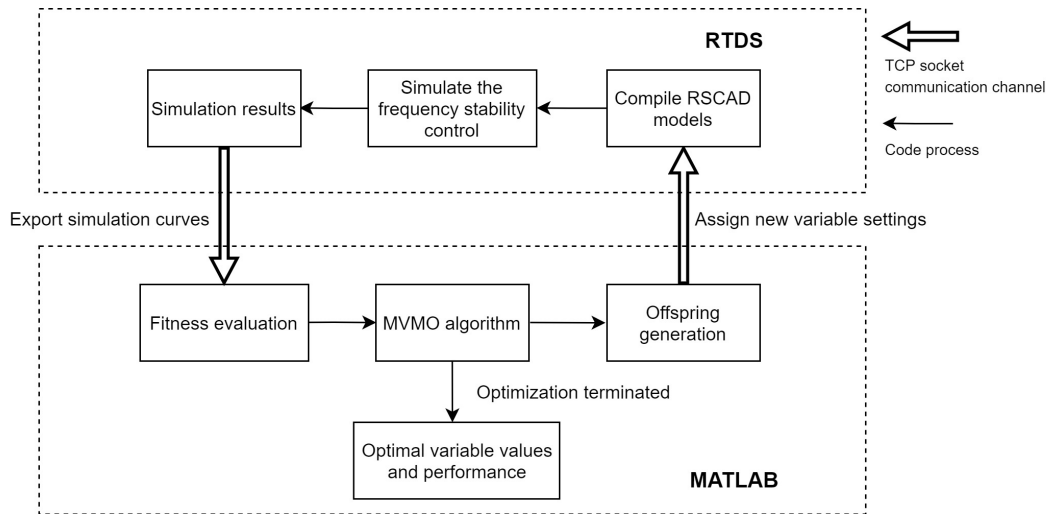


Figure 5.3: Flowchart for optimization between MATLAB and RTDS

The MVMO code is written as MATLAB scripts. However, the real-time simulation of the IEEE 9 bus system is processed in RSCAD every iteration. Therefore, the communication channel between MATLAB and RSCAD should be established in every iteration to exchange data and results. The flowchart of optimization and simulation processes are shown in figure 5.3. Before the start of every simulation, generated new variables are compiled in the RSCAD power system model. The MATLAB scripts send command to RSCAD and control all the actions during simulations like the load switching. Normally, the action commands can be written in a script file, and executed in RSCAD 'Runtime' file. Considering the cooperation between MATLAB and RSCAD, the action commands are sent and received from the communication channel instead.

In every iteration, the simulation result is exported as the form of signal curves, including curves of frequency, frequency derivative and battery current. These curves are proceeded in MATLAB to calculate the objective function and constraints. The MVMO algorithm will record necessary information and generate a new set of variables, and then optimization moves to the next iteration. The final result including best variables and fitness evaluations is generated from MVMO algorithm.

The communication channel between MATLAB and RSCAD is established by using command 'ListenOnport()'. This command establish a TCP/IP socket communication between RSCAD and MATLAB. The RSCAD 'Runtime' file (.sib file) operates as a TCP server which listens to a port with a certain port number. Meanwhile, MATLAB also connects to the same port number, and automatically commands the real-time simulation. The codes to establish a communication channel between RSCAD 'Runtime' file and MATLAB is shown below. The RSCAD 'Runtime' script needs to establish communication channel $n_{MaxItera}$ times until the optimization is finished. MATLAB uses an external library known as 'jtcp.m' to connected the port with same port number as RSCAD. Then RSCAD 'Runtime' file can listen to the commands from MATLAB. First, MATLAB assigns new optimization variables to the IEEE 9 bus system model in RSCAD and compile it. Then, RSCAD is commanded to start the simulation and record the plots of results. Finally, simulation is stopped and communication channel is closed by MATLAB.

Commands in RSCAD 'Runtime' script to operate as a TCP server [4]:

```
for(j = 1; j < nMaxItera + 1; j + +){
    fprintf(stdmsg, "Runtime is now acting as TCP Server...\n");
    fprintf(stdmsg, "Evaluation Number : %d\n", j);
    ListenOnport(4575, true);
    //close the port in Matlab for for loop to continue.
    fprintf(stdmsg, "Runtime is still acting as TCP Server\n");
    fprintf(stdmsg, "Runtime is now finished acting as TCP Server\n");
}
```

'jtcp.m' based TCP communication in MATLAB M file[4]:

```
portnum = 4575;
JTCPOBJ = jtcp('REQUEST', '127.0.0.1', portnum);
msg = sprintf('SetSlider "DraftVariables : NsB" = %f;', x(1));
jtcp('writes', JTCPOBJ, msg);
:
msg = sprintf('SetSlider "Subsystem#1 : CTLs : Inputs : droop" = %f;', xxy(14));
jtcp('writes', JTCPOBJ, msg);
jtcp('writes', JTCPOBJ, 'Start;');
:
jtcp('writes', JTCPOBJ, 'SavePlot"Frequency", "C : \Desktop\Frequency";');
:
jtcp('writes', JTCPOBJ, 'Stop;');
closeportMsg = sprintf('Closeport(%d);', portnum);
jtcp('writes', JTCPOBJ, closeportMsg);
```

Afterwards, MATLAB imports the saved simulation results and run the MVMO algorithm illustrated in 5.2. The generated new variable settings will be assigned to the RSCAD 'Runtime' file, and a new iteration starts again, until the optimization is terminated.

5.4. Experimental Settings for MVMO

Table 5.1 shows the parameter settings for MVMO. The settings for droop and derivative control and VSP are same only expect variable dimension n_{var} and initial mutation dimension $n_{m.start}$. As explained in subsection 5.2, the mutation dimension n_{muta} , scaling factor f_s and d-factor influence the convergence speed of optimization. Their values are also updating with optimization. Therefore, their initial values, final values or variation steps are defined in table 5.1. At the beginning, mutation dimension n_{muta} is larger to encourage variation of optimization variables, and scaling factor f_s is smaller to reduce the influence of archive values during the offspring generation. In contrast, at the end of optimization, archive values dominate the offspring generation, and mutation dimension is very small. As the d factor oscillates around current shape factor, Δd determines the oscillation magnitudes.

The optimization starts with random initial values within user defined ranges. The boundaries in two optimization cases are shown in table 5.2 and 5.3 respectively. The upper and lower bounds of variables are determined by constraints of hardware and sensitivity analysis.

The series number of batteries $N_{s,B}$ and UCs $N_{s,UC}$ are constrained by the DC-link voltage 4kV. The nominal voltage values of battery and UC per cell are 3.4V and 2.3V. The maximum series number is DC-link voltage divided by voltage per cell. $N_{s,B}(max)$ and $N_{s,UC}(max)$ are calculated as 1176 and 1739. The lower limits of $N_{s,B}$ and $N_{s,UC}$ are the lowest voltage to maintain the continuous mode of buck boost converter. Considering $D = 1 - \frac{V_{battery,UC}}{V_{DC-link}}$, in order to maintain the sensitivity of duty cycle, the HESS voltage is selected higher enough to avoid duty cycle always operates above 0.9. Then the lower limits for battery and UC voltage is $\frac{1}{10}$ of DC-link voltage corresponding to $N_{s,B}(min)=118$ and $N_{s,UC}(min)=174$.

The parallel number of batteries and UCs related to the output current and equivalent series resistance. The size of HESS cannot be too larger because otherwise current will overflow converters and transformers. Considering duty cycle is not preferred to be higher than 0.9, the maximum output current of HESS can be estimated as equation 5.20, where the maximum current equals to the switch current of power electronics 10kA; The per-cell voltages for battery and UC are 3.4v and 2.3V. Hence, the maximum of parallel numbers $N_{p,B,max}$ and $N_{p,UC,max}$ are 1176 and 884. No lower limits are needed for the parallel numbers.

$$I_{max} = N_{p,max} \times \frac{U_{cell}}{R_{cell}} \quad (5.20)$$

For droop and derivative control, the virtual inertia H_{FDWG} should be larger than the calculated inertia requirement 22.76s in equation 4.5 but still in a range that HESSs are capable to supply. The output power of droop control is inversely proportional to the frequency droop. Therefore the upper limit of R is calculated droop requirement 0.019HZ/MW. The outer power controllers and inner current controllers are PI controllers. The ranges of their parameters are determined by sensitivity analysis. A series of parameter settings are tested to find the boundaries for stable operation. During testaments, the proportional gains of PI controllers are vary sensitive around value 1, because the final output of PI controllers is duty cycle which is valid between 0 and 1. A PI controller setting with proportional gain larger than 1 can easily saturate the output duty cycle. A similar idea for the ranges of integral gains, their upper limits show the range of stable operation.

For VSP, second-order control loops are used to output the duty cycle. The upper limits of their natural frequency should be at least two times lower than the switching frequency of converters. The damp factors ζ should be in range [0,1], because the system is designed under-damped. The lower limit of the time constant of high-pass filter $T_{HPF}(min)$ is selected as 1, because the operation time of UCs should be around 1 second. The upper limit of T_{HPF} is 3, because batteries should take over the load demand after UCs.

Table 5.1: MVMO parameter values

$n_{MaxItera}$	Maximum iteration numbers;	300
$n_{archive}$	Stored population in archive;	8
$n_{m.start}$	Initial dimensions for mutation;	11 or 14
$n_{m.end}$	Final dimensions for mutation;	1
$n_{m.freq}$	Frequency when dimensions are changed;	23
$f_{s.start}$	Initial value of scaling factor;	1
$f_{s.end}$	Final value of scaling factor;	10
d_{init}	Initial value of d factor;	1
Δd	Variation of d factor;	0.25
n_{var}	Variable dimensions;	11 or 14
$n_{var.con}$	Number of continuous variables;	7 or 8
$n_{var.dis}$	Number of discrete variables;	4
n_{constr}	Number of constraints;	6

Table 5.2: Upper and lower limits of optimization variables (droop and derivative control)

$N_{s.B}(max; min) : [1176; 118]$	$N_{p.B}(max; min) : [1176; 1]$
$N_{s.UC}(max; min) : [1739; 174]$	$N_{p.UC}(max; min) : [884 1]$
$K_{P.p.B}(max; min) : [1.0; 0.0]$	$K_{I.p.B}(max; min) : [10.0; 0.0]$
$K_{P.i.B}(max; min) : [1.0; 0.0]$	$K_{I.i.B}(max; min) : [10.0; 0.0]$
$K_{P.p.UC}(max; min) : [1.0; 0.0]$	$K_{I.p.UC}(max; min) : [10.0; 0.0]$
$K_{P.i.UC}(max; min) : [1.0; 0.0]$	$K_{I.i.UC}(max; min) : [20.0; 0.0]$
$H_{FDWG}(max; min) : [25.0; 10.0]$	$R(max; min) : [0.3; 0.05]$

Table 5.3: Upper and lower limits of optimization variables (VSP)

$N_{s.B}(max; min) : [1176; 118]$	$N_{p.B}(max; min) : [1176; 1]$
$N_{s.UC}(max; min) : [1739; 174]$	$N_{p.UC}(max; min) : [884 1]$
$\omega_{n.UC}(max; min) : [120.0; 0.0]$	$\omega_{n.B}(max; min) : [120.0; 0.0]$
$\zeta_{UC}(max; min) : [1.2; 0.0]$	$\zeta_{B}(max; min) : [1.2; 0.0]$
$K_{UC}(max; min) : [1.0; 0.0]$	$K_{B}(max; min) : [1.0; 0.0]$
$T_{HPF}(max; min) : [0.6; 0.0]$	

5.5. Results of MVMO for Droop and Derivative Control and VSP

After 300 times of evaluations, the result of optimization gives the optimal solutions of two cases with minimized fitness values. The convergence of optimization can be shown by the fitness curves during evaluations in figure 5.4 and 5.6. The fitness values have been normalized to their initial value as equation 5.21. Because the initial value is also the largest fitness value, and the fitness value is gradually reduced during optimization.

$$\text{Normalized Fitness} = \frac{\text{Fitness}}{\text{Fitness}(1)} \quad (5.21)$$

Figure 5.4 shows the fitness evaluations and objective function values of droop and derivative control during the optimization. The optimization starts with a random initial state, and fitness value is rather high at the beginning, because some constraints are violated. The fitness converges fast in the first 100 iterations, which means constraints are gradually satisfied during this time. After that, fitness is slightly improved by decreasing the value of objective function. Meanwhile, the value of objective function is also high at the beginning, because the HESS is oversized. Then the cost of HESS is reduced during the optimization, and finally the optimal solution gives a minimized HESS cost.

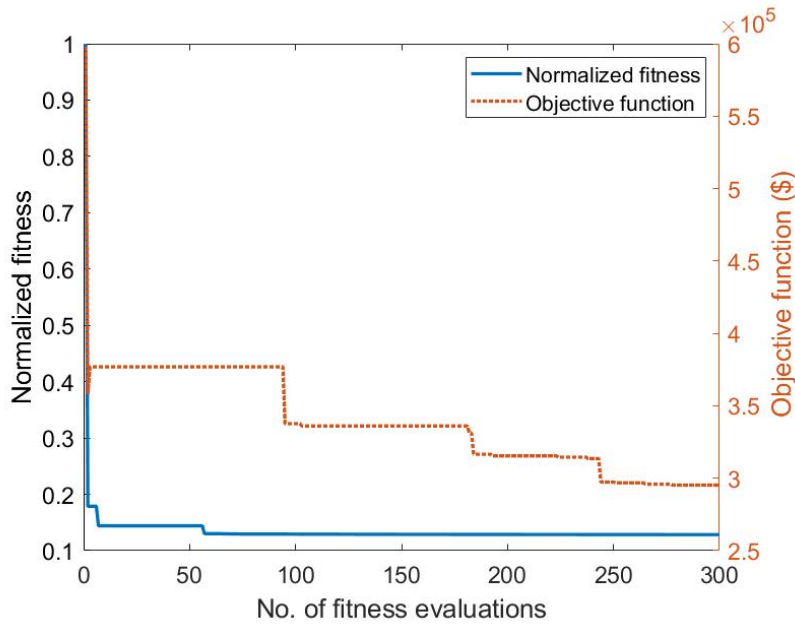


Figure 5.4: Normalized fitness value and objective function value of droop and derivative control

Figure 5.5 shows the convergence of optimization variables. These variables are normalized within the upper and lower boundaries as equation 5.10. The real value of the optimal solution is shown in table 5.4. Optimization starts with random initial values which violate many optimization constraints leading to a high fitness value. The variable values oscillate a lot to search for satisfied solutions before 100 iterations. Later, variable values gradually converge to the best solution that MVMO algorithm found. The optimal solution is shown in table 5.4. The gain value $K_{I,i,UC}$ for UC is obviously larger than battery value $K_{I,i,B}$, because UC current is faster than battery. Besides, the optimized frequency droop R is more gentle than calculated value 0.019HZ/MW in equation 4.3.

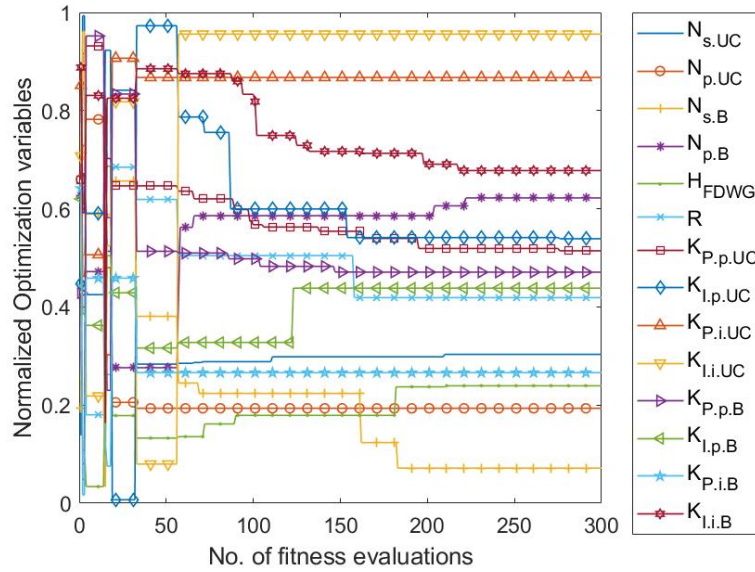


Figure 5.5: Normalized optimization variables of droop and derivative control

Table 5.4: Optimal solution (droop and derivative control)

$N_{s.UC} : 886$	$N_{p.UC} : 266$	$N_{s.B} : 545$	$N_{p.B} : 695$
$K_{P.p.UC} : 0.77$	$K_{I.p.UC} : 6.57$	$K_{P.i.UC} : 0.58$	$K_{I.i.UC} : 10.10$
$K_{P.p.B} : 0.56$	$K_{I.p.B} : 6.02$	$K_{P.i.B} : 0.18$	$K_{I.i.B} : 3.27$
$H_{FDVG} : 22.41s$	$R : 0.012HZ/MW$		

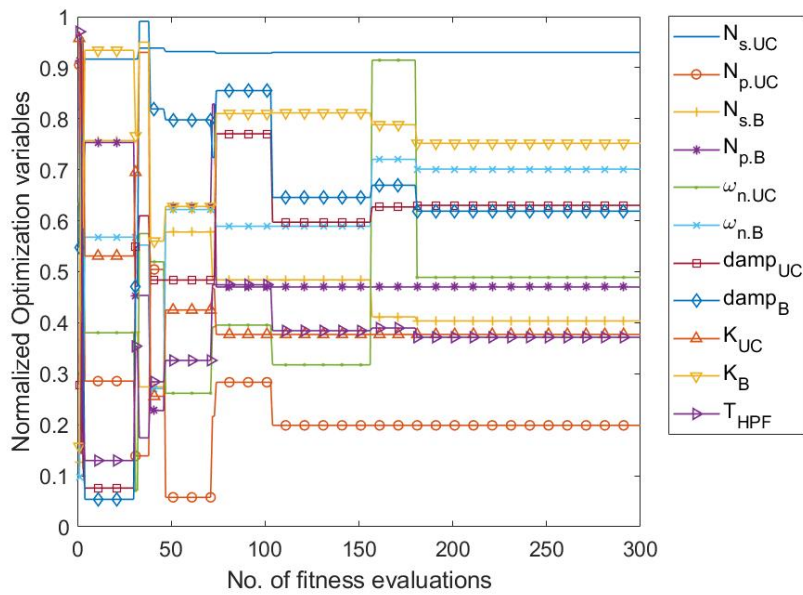


Figure 5.7: Normalized optimization variables of VSP

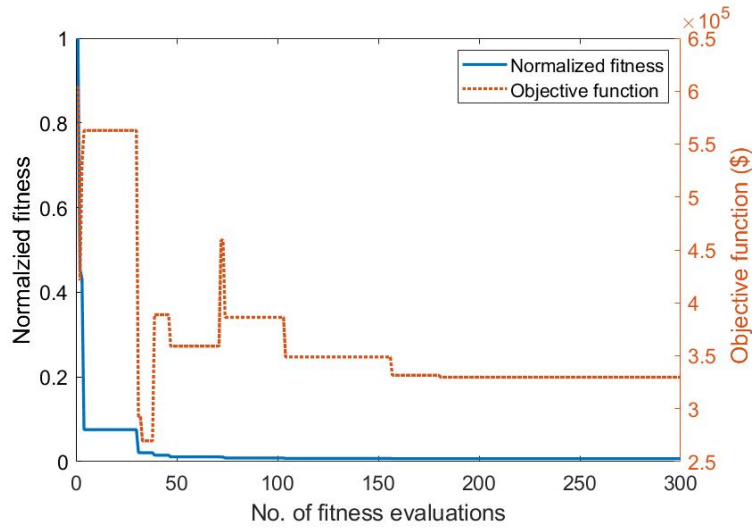


Figure 5.6: Normalized fitness value and objective function value of VSP

Table 5.5: Optimal solution (VSP)

$N_{s,UC} : 698$	$N_{p,UC} : 551$	$N_{s,B} : 866$	$N_{p,B} : 410$
$\omega_{n,UC} : 36.82\text{rad/s}$	$\omega_{n,B} : 65.44\text{rad/s}$	$\zeta_{UC} : 0.50$	$\zeta_B : 0.65$
$K_{UC} : 0.65$	$K_B : 0.79$	$T_{HPF} : 1.72\text{s}$	

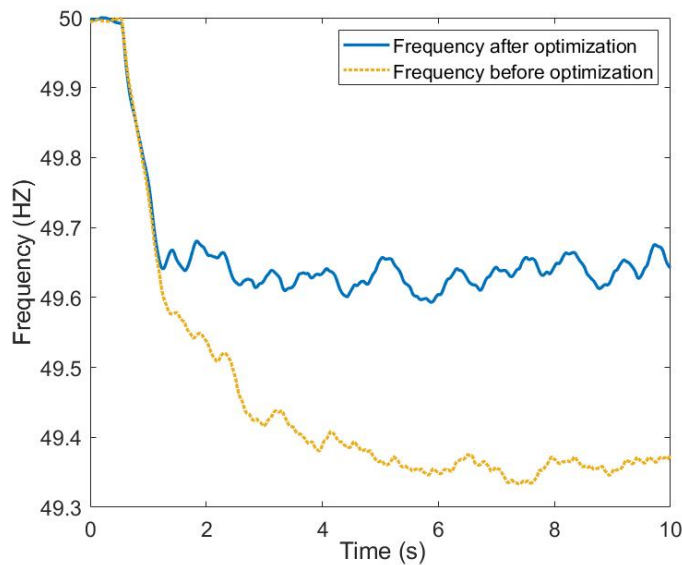


Figure 5.8: Comparison of frequency performance of droop and derivative control before and after optimization

Similar phenomenons of fitness, objective function and optimization variables in VSP case can be observed in figure 5.6 and 5.7. The normalized fitness also converges fast before 100 iterations, but its final value 0.0109 is much lower than droop and derivative control case value 0.128. In fact, the optimized HESS cost of VSP 329740\$ is larger than droop and derivative control 295230\$. Therefore, the small difference in objective function values does not have a huge impact on the final value of

normalized fitness. On the other hand, the fitness is normalized by its initial value which has a larger difference in two cases. More constraints are violated at the beginning of VSP optimization (penalty 3.16×10^7) than droop and derivative control case (penalty 2.73×10^6) leading to a smaller normalized VSP fitness. The fact is that the fitness in both case is finally optimized to a same level. The oscillation of objective function shown in figure 5.6 takes longer time to converge comparing with droop and derivative control optimization, which means constraints take longer time to be fully satisfied. This oscillation is also reflected in the variation of optimization variables in figure 5.7. After the oscillation, variable value are very close to the best solution and gradually converge to it.

Table 5.6: Comparison of droop and derivative control results

	Old results	Optimized results
f_{nadir}	49.3333HZ	49.5931HZ
ROCOF	0.4120HZ/s	0.3774HZ/s
$N_{s,UC}$	1200	886
$N_{p,UC}$	200	266
$N_{s,B}$	900	545
$N_{p,B}$	300	695
UC cost:	77700\$	76300\$
Battery cost:	156060\$	218930\$
Total HESS cost	233760\$	295230\$
η_{UC} :	0.9934	0.9943
$\eta_{battery}$:	0.9057	0.9699

The frequency control results of droop and derivative control before and after the optimization are compared in figure 5.8. The previous setting of frequency stability control is calculated in subsection 4.5. The frequency droop is set just above admissible frequency 49.2HZ in 84MW load increase condition, and ROCOF is controlled around 0.4HZ/s. However, this performance is achieved according to the lowest standard, and the battery efficiency 0.9057 $\eta_{battery}$ is lower than our requirement 0.95. After the optimization, as shown in table 5.6, the settled frequency is significantly improved with a nadir of 49.5931HZ. The rising of settled frequency is because of the optimally tuned frequency droop and HESS size. It is worth to mention, although settled frequency may increase with the droop setting, it is still limited by the power capability of HESS. That is the reason for optimizing HSEE size and frequency droop together. For example, in the old result, the battery pack has a rather higher equivalent series resistance leading to an efficiency around 0.9. This efficiency will keep decreasing if we increase the output power of droop control as the result of chapter 4, and to a certain extend of power reference, the battery output will not increase anymore. As a result, batteries should supply sufficient power and meanwhile operate economically. So the optimal solution, as shown in table 5.6, is increasing the parallel number of batteries to reduce the power losses and increase power output. Meanwhile, some series batteries are removed to save construction investment.

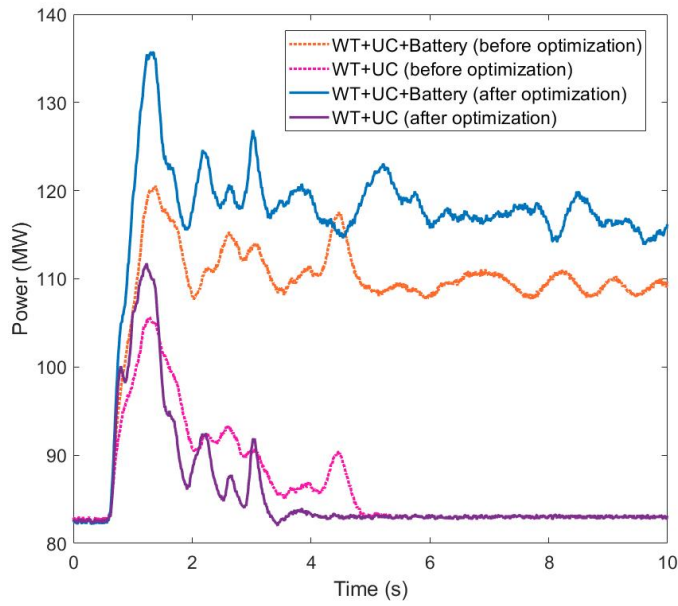


Figure 5.9: Comparison of power output of droop and derivative control before and after optimization

Table 5.7: Comparison of VSP control results

	Old results	Optimized results
f_{nadir}	49.5517HZ	49.6908HZ
ROCOF	0.3844HZ/s	0.3045HZ/s
$N_{s,UC}$	1200	698
$N_{p,UC}$	200	551
$N_{s,B}$	900	866
$N_{p,B}$	300	410
UC cost:	77700\$	124510\$
Battery cost:	156060\$	205230\$
Total HESS cost	233760\$	329740\$
η_{UC} :	0.9939	0.9846
$\eta_{battery}$:	0.8897	0.9591

The ROCOF of optimization result is improved to 0.3774HZ/s, which helps system frequency settle at an earlier time than the old settling time. The ROCOF improvement shows the increasing of system inertia which is enhanced by the virtual inertia of UCs. The power output of frequency stability control is shown in figure 5.9. The UC power after optimization is faster and larger than previous value, because UCs are sized larger, and PI controller for UC is tuned faster. Since the droop setting is increased, the battery power output is around 10MW larger than previous result.

Considering construction cost of HESS, the battery cost is increased due to the expansion of parallel

cells. The optimized parallel number of battery $N_{p,B}$ is more than two times of previous value, but the series number is almost halved. The change in battery size shows that the output power of battery is more impacted by equivalent series resistance rather than terminal voltage. The cost of UCs does not change much, which means previous UC size is sufficient to supply required power. Since UCs have a very low equivalent series resistance, UC efficiency η_{UC} is not a problem. However, resistance of batteries not only influences in output power, but also leads to a low efficiency around 0.9. After increasing the parallel number $N_{p,B}$, equivalent series resistance of batteries is reduced and optimized efficiency of power delivery is improved to 0.9699. As a result, system frequency is enhanced to a more stable performance, and HESS size becomes more efficient.

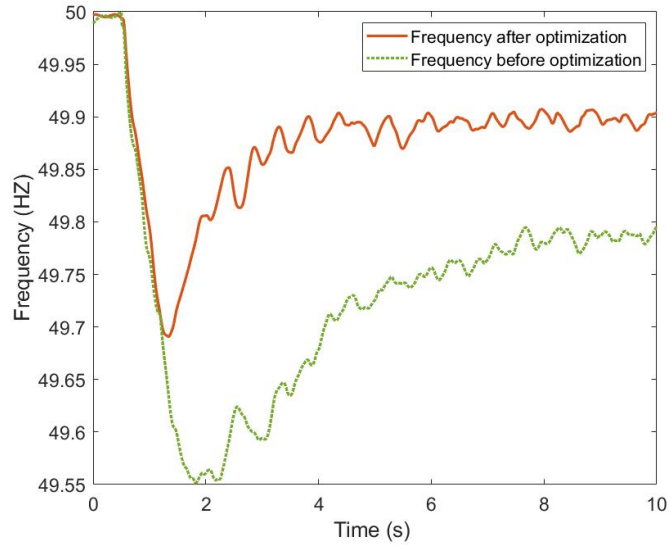


Figure 5.10: Comparison of frequency performance of VSP before and after optimization

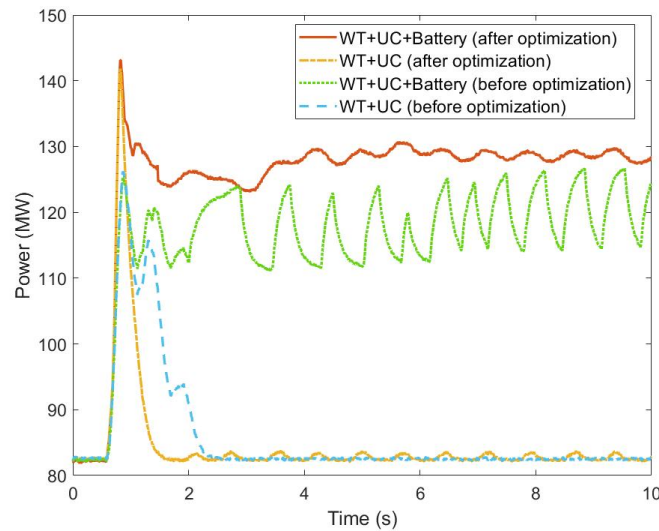


Figure 5.11: Comparison of power output of VSP before and after optimization

Figure 5.10 shows the frequency curve of VSP before and after optimization. As discussed in sub-section 2.4, the control reference of VSP comes from power difference rather than frequency. There-

fore, the VSP performance is not determined directly by setting the inertia value and settled frequency. Instead, the performance of second-order control loop in VSP has a huge impact on frequency response. The ROCOF is mainly determined by reaction speed of controllers, where the natural frequency ω_n and damping factor ζ have been considered as optimization variables. As shown in table 5.7, the optimized ROCOF is reduced 0.08HZ/s than the old value. Hence, the frequency is settled earlier after optimization, which means the power difference between FDWG generations and the power flows delivered by FDWGs located buses 7 and 9 to load 8 (P_{78} and P_{98}) is balanced faster. According to swing equation 2.1, frequency drop is prevented after power balance. Therefore, faster controller response is one reason to explain why VSP has a higher settled frequency after optimization. The other reason is increased controller gain values K_{UC} and K_B which determine the controller sensitivity to input signals. A higher gain means a smaller settling error of input power difference. As shown in figure 5.11, the power output after optimization is 10MW larger than the old value, which can explain why frequency is settled at a higher value after optimization.

After optimization, more load demand is undertaken by FDWGs leading to a higher settled frequency. However, high gain values are not always suitable in VSP controllers. Since the output signal of VSP controller is duty cycle which is only valid between 0 and 1, a large gain value may saturate the duty cycle, especially when power capacity of HESS is insufficient. For example, when duty cycle reaching its maximum, the power output is still lower than the power reference due to a high controller gain. The worst situation is duty cycle keeps oscillating between 0 and 1. A larger controller gain may not only cause oscillations but also amplify disturbance. The optimization tuned the gain values by trading off between fast response and stable output.

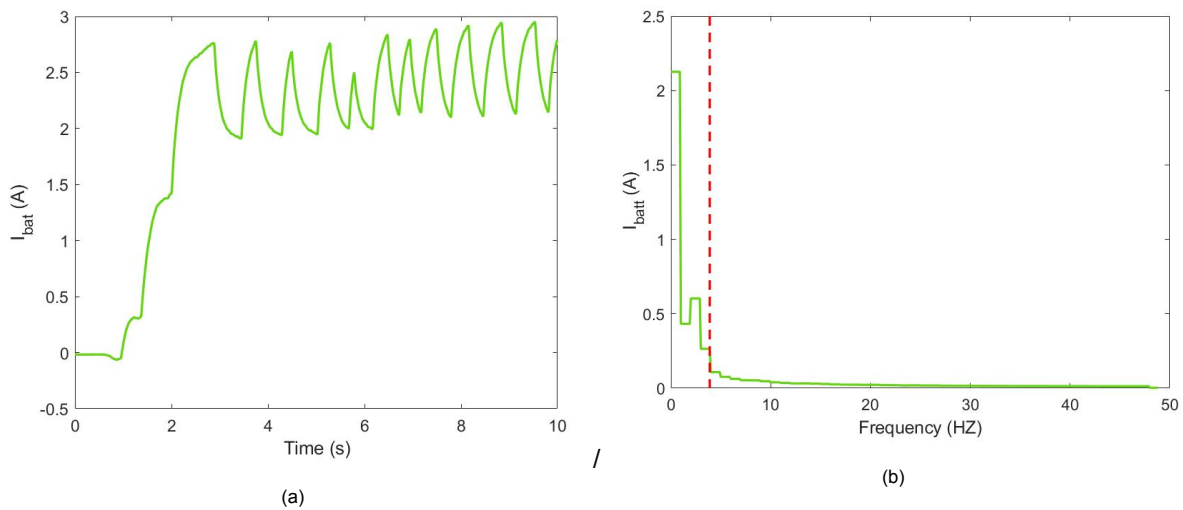


Figure 5.12: (a) Battery current of VSP before optimization, (b) frequency component analysis of corresponding battery current.

The result of HESS sizing is also shown in table 5.7. The optimized UC cost is 1.6 times than the old cost due to the higher power demand. In figure 5.11, the optimized UC power is much faster and higher than the old curve. The reason has been explained according to controller improvement in last paragraph. The higher power reference from frequency controller needs to be supplied by a larger size of UCs. However, in table 5.7, only the parallel number of UC $N_{p,UC}$ is increased, and the series number of UC $N_{s,UC}$ is actually reduced. On the one hand, the old $N_{p,UC}$ 200 is rather small comparing

with $N_{s,UC}$, and increasing $N_{p,UC}$ can give a more significant improvement in power capability. On the other hand, the terminal voltage of UC is proportional with $N_{s,UC}$ which also influences the duty cycle of DC-DC converters. The terminal voltage after optimization 1.6kV is less than half of the DC-link voltage 4kV, which means the duty cycle of maximum power is less than 0.5. As analyzed in the conclusion of subsection 4.5.3, the duty cycle is selected smaller to guarantee the UC power efficiency, which correspond to the duty cycle decrease after optimization.

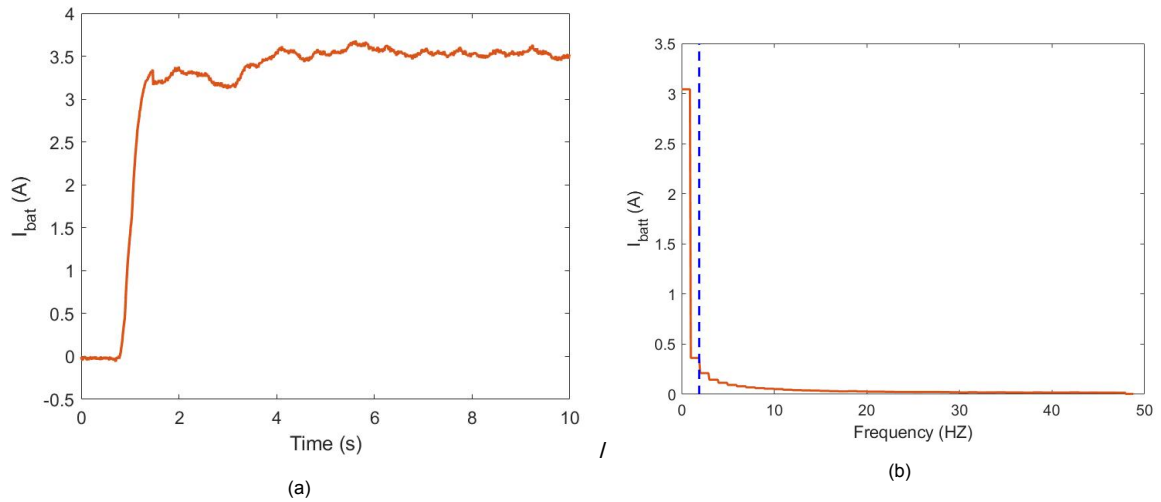


Figure 5.13: (a) Battery current of VSP after optimization, (b) frequency component analysis of corresponding battery current.

As seen in figure 5.11, the total power before optimization oscillates a lot, because the old cut-off frequency $T_{HPF} = 1s$ cannot filter out this oscillation, and the old damp factor and $\zeta_B = 0.26$ cannot damp the oscillation. The frequency analysis of battery current is shown in figure 5.12, the 75% of current magnitudes are located at the left side of the red line 3.898HZ. The oscillation is shown as the spike away from DC current. As the DC component of battery current is added in constraint $g_4(\mathbf{x})$, the oscillation magnitude after optimization is damped a lot. The position of 75% of current magnitude is improved to the blue line 1.399HZ. As a result, the oscillation is battery current is sufficiently avoided.

5.6. Comparison between Optimized Droop and Derivative Control and VSP

The optimized performance of droop and derivative control and VSP is compared in this subsection. Figure 5.14 shows the frequency curves of two cases. It is clear to observe that VSP has a better frequency nadir and ROCOF. The reason for this performance result can be explained by the power output from FDWG in two cases. We can assume that the generation from wind turbine does not change during the time of frequency disturbance. Then the curves above 82MW can be seen as the extra power generation from HESSs.

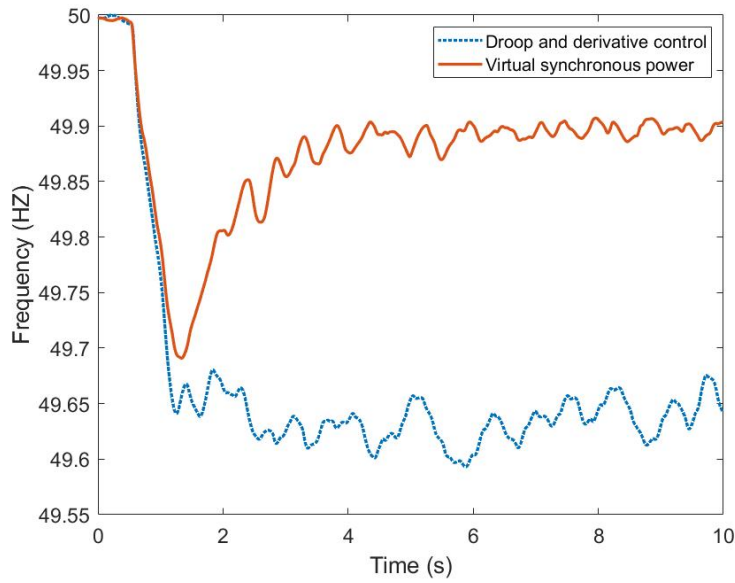


Figure 5.14: Comparison between optimized frequency performance of droop and derivative control and VSP

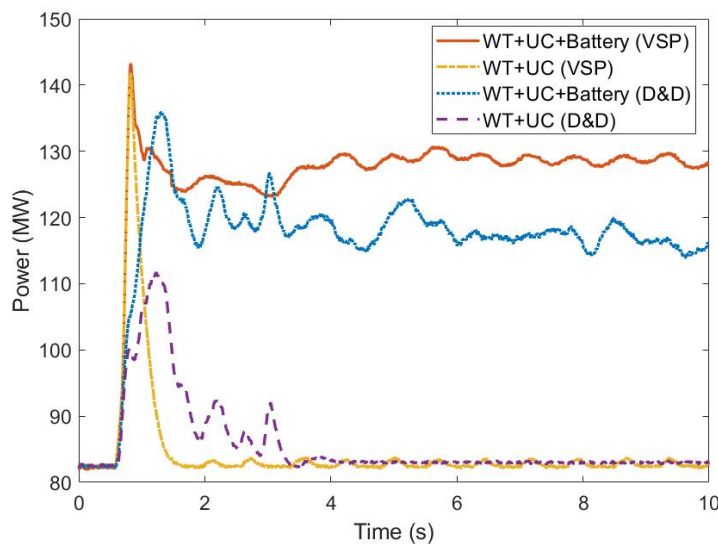


Figure 5.15: Total power output of droop and derivative control and VSP

First, let us compare the difference of UC power. The derivative control requires frequency measurement and derivative calculation. As observed from the corresponding curve, the UC output of derivative control works in around 3 seconds from beginning. After 4s, the derivative control is block due to only left small variations on frequency curve. This operation strategy can also help stabilize system frequency. For VSP, UCs operate in around 1 second from beginning. The UC output in VSP is larger and faster than derivative control leading to a lower ROCOF, which can be explained by VSP principles. As discussed in subsection 2.4, VSP does not need frequency measurement and derivative calculation. Therefore, VSP is able to avoid the delay of PMU and disturbance in these control loops. As observed, UCs of VSP reach the peak value earlier than derivative control case, the UC power equals the total power for 1s in VSP case. Besides, the power reference of UC in VSP comes from

a HPF, which means UCs can immediately supply a step power increase. Comparing with derivative control, VSP can make a better use of the high power density of UCs.

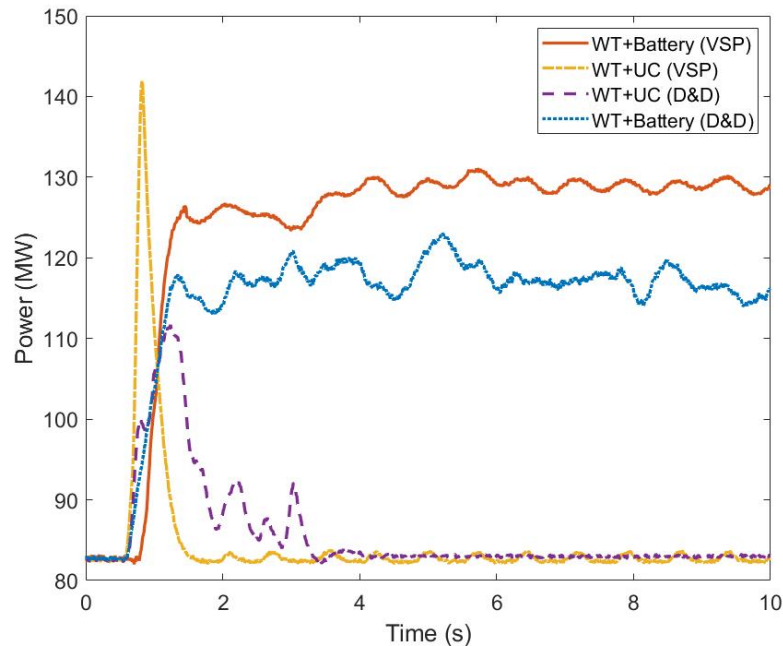


Figure 5.16: Battery and UC power output of droop and derivative control and VSP

As shown in figure 5.16, the battery power output gradually increases to replace the UC power. For droop control, battery power completely replace UC when frequency reached the set frequency around 4s. In contrast, VSP is trying to fill the power gap between FDWG generation and the power delivered from the FDWG connected bus. Corresponding to the frequency curve, VSP battery output gradually converges to the power reference. Comparing with final battery output power of droop control, battery output of VSP is around 10MW larger. Because power output of droop control is settled when frequency is stabilized. In contrast, after stabilising the system frequency, VSP still needs to catch up the changing of mentioned power difference. From swing equation point of view, droop control aims to achieve P_e equals to P_m at synchronous generators, while VSP aims to recover the P_e as the original value.

The power output difference between droop and derivative control and VSP can also explain the HESS sizing result of optimization. The HESS of VSP is sized larger than HESS of droop and derivative control, because VSP has a larger power demand.

As a result, VSP has a faster power-frequency response than droop and derivative control, and it can make a better use of the advantages of UC. The HESS of VSP also sized larger than droop and derivative control due to the higher power demand. However, VSP performance is influenced by locations, while droop and derivative control uses the global frequency reference as the control reference.

6

Conclusions and Future Work

6.1. Conclusions for Research Questions

This thesis focuses on the frequency response of FDWGs. UCs are proposed as ideal power sources to supply the fast active power-frequency response. Droop and derivative control and VSP are both implemented to improve the power system frequency stability. The optimal performance of the frequency stability control system is found by using MVMO algorithm. The research questions are answered during this study of this thesis.

Research question 1: What are the dynamic properties of an UC that should be taken into account for EMT modeling and simulation of interconnected power system?

The unique dynamics of an UC comes from its physical structure which is analyzed in section 3.1. Larger surface area of porous electrodes and microscope electric fields significantly increase the capacitance of an UC. Meanwhile this structure gives several aspects of dynamic phenomenons that are different from a normal parallel plate capacitor. Among them, three aspects of fast dynamics are considered during the frequency stability control, because UCs, as high power density sources, are going to supply fast active power frequency response in a time scope of few seconds. The considered UC dynamics in RTDS are listed below:

1. Distributed circuit elements: Charges distributed in porous electrodes form numerous particle-scale electric fields, which are considered as distributed capacitance. Electrolyte containing ions flows into these pores, and the ionic resistance of electrolyte forms distributed resistance. Therefore, the UC capacitance or resistance is not represented by one value but distributed values.
2. Charge redistribution phenomenon: This is a time scale phenomenon of an UC. An UC is only partially charged by a fast charging current. The charges' distribution are changing with time due to different traveling time.
3. Voltage dependence: UC capacitance and resistance are changing with its voltage. Especially its capacitance obviously increases with voltage value.

By comparing with a simple RC model by constant current charging and discharging, it shows the actual voltage value can vary a lot due to distributed elements and voltage dependence. After charging, RC model remain constant, but UC model voltage spontaneously changes due to charge redistribution phenomenon. Therefore, it is important to consider these dynamics during the real-time simulation to truly represent an UC storage system.

Research question 2: How can a generic UC model be designed in RTDS environment based on the capabilities of RSCAD?

The generic UC models can be categorised as equivalent electric circuit models and fractional-order models. Among equivalent electric circuit models, they can be further classified as RC ladder model, RC series branch model and RC parallel branch model. RC ladder model simulates the physical structure of an UC, and it represents the "transmission line" connecting two electrodes. RC series branch model is a circuit representation of measured UC EIS. The previous two models represent a general performance in a wide frequency range, and they do not emphasize the fast dynamic performance of an UC. In contrast, RC parallel branch model is derived considering UC performance in different time scales. The fast branch is estimated according to current charging in 20ms, and the only voltage dependent capacitance is considered on the fast branch. Therefore, RC parallel branch model has a relatively high high-frequency accuracy. Besides, it is easy to be implemented in RTDS, because each branch can be calculated independently during simulations. The fractional-order model is considered as a higher level model, because fractional-order elements also includes integer-order elements used in equivalent circuit models. The inevitable problem of fractional-order models are lack of fractional-order circuit technology to fully implement in power system simulations. The fractional-order models are eventually estimated by integer-order elements. As a result, RC parallel branch model is the most suitable UC model in this thesis.

The RC parallel branch model is implemented in RSCAD by using built-in c-builder. The UC element in RSCAD have two defined physical nodes to represent two electrodes. The conductance and current injections between two physical nodes are calculated according to voltages of two physical nodes in every simulation step, because RTDS solves the voltages of power system by representing elements as Norton equivalent form. Besides, the integral of current in one simulation step is estimated by the trapezoidal area formed by discrete values. The detailed procedures of building an UC model in RSCAD environment is illustrated in section 3.3. Finally, the created UC successfully represents the expected three UC dynamics.

Research question 3: Up to which extent can the fast active power-frequency control of a FDWG be enhanced by adding an UC in its DC link?

Question 3 focuses on using high-power density UCs to improve the fast active power-frequency control. This power system is tested in RTDS. The research question 3 can be further broken down into 3 sub-questions. Sub-question 1 is how to establish a HESS based on UC and battery. In order to search for the optimal solution with created HESS, sub-question 2 is how to formulate an optimization problem considering frequency stability control and HESS operation. The sub-question 3 is how to solve this optimization problem.

The HESS comprises high-power density UCs and high-energy density batteries. UCs can significantly improve the reacting speed and power capability of a HESS, and batteries supply a bulk amount

of energy in a longer time scope. The slower battery current can also extend batteries' lifetime. Batteries and UCs are connected on a DC-bus through DC-DC converters. This connection topology increase the control-ability of the HESS. The fast changing power demand is allocated to UCs, and slow power is allocated to batteries. A HESS is built based on these principles.

Frequency stability control and HESS sizing are considered two aspects in optimization formulation. The performance of frequency stability control is described by frequency nadir f_{nadir} and ROCOF defined in section 2.1, which are considered as optimization constraints with limit values. The HESS should be sized to supply sufficient power but also minimize the construction cost. A series tests show that the required HESS is highly related with the operation state of buck-boost converters. Meanwhile, testaments show that HESS efficiency is very low when HESS has a larger current. Therefore, HESS efficiency is considered as the third optimization constraint. The construction cost is calculated as the objective function. The forth constraint is on slow changing battery current, which protects batteries from high-frequency oscillations and extends batteries' lifetime.

This is a non-convex, mixed-integer optimization problem. The MVMO method as one of the evolutionary algorithms is used to solve this problem. The optimization variables are controller parameters and HESS sizes. MVMO starts from random initial variable values. In every iteration, simulation result is evaluated by a fitness value. The n-best solutions are stored in an archive, and the mean, variance and shape factors of n-best solutions influence the mapping of offspring generation. Hence, new variables converge to the optimal solution during iterations. The optimal solutions with minimal fitness values are found for droop and derivative control and VSP.

The improvement of droop and derivative control and VSP is shown in section 5.5. Frequency control performance in two cases are both improved by increase the fast power response. UCs are sized larger to increase the power capability of the HESSs. Meanwhile, controllers, especially for UC controllers, are tuned to react faster to power references. The parallel number of batteries are increased to meet the efficiency constraint.

Comparing the optimal performance of droop and derivative control and VSP, VSP supplies a faster active power response, because the power reference of VSP comes from a power difference which is faster than the frequency measurement and derivative calculation. Meanwhile, UCs are sized larger in VSP case to supply a larger magnitude of power. Finally, droop and derivative control stabilizes frequency at a new equilibrium point, and VSP tries to fill the power gap of P_{RES} and P_{BUS} . That is why frequency in VSP is stabilized at a higher value than droop and derivative control.

6.2. Suggestions for Future Work

In this thesis, the application of fast active power-frequency response starts from UC modeling to optimization of the entire system. Many interesting technical details have been studied. Some aspects can be further extended in future researches.

- **More accurate UC models:**

In this thesis, the data used for UC modeling comes from previous references, and different models are qualitatively compared. If equipment satisfied, the parameters of a selected commercial UC can be estimated, and different UC models can be compared under the same situation. Moreover, a fractional-order model can be studied to implemented in power system simulations.

- **High power-rate DC-DC converters:**

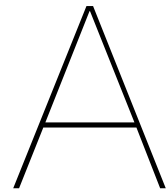
This thesis uses buck-boost converters to connect HESSs as in many references. In future work, power electronic converters with high power-rate can be considered to supply the fast active power response. Meanwhile, the economy of DC-DC converters can also be considered. The cost of high power-rate converters is larger, but the HESS is in silence for most of time. So considering the cost of power electronic converters, the power demands of frequency stability control need to be compromised. Besides, considering switching losses, the efficiency of DC-DC converter can also be improved.

- **Protection and maintenance of HESS:**

Although current limiters and power limiters are used in the controller loops, HESS needs a more complicate protection system in reality. Power controllers and voltage controllers should be designed to control the charging states of HESS. Power ramp controller can also be considered for batteries to mitigate the changing rate of battery current. The charging strategy should also be planned for the HESS. Besides, the power switching from UC to battery is very fast in this thesis. Extra methods can be derived to smooth the power allocation between battery and UC.

- **Application with other types of RES:**

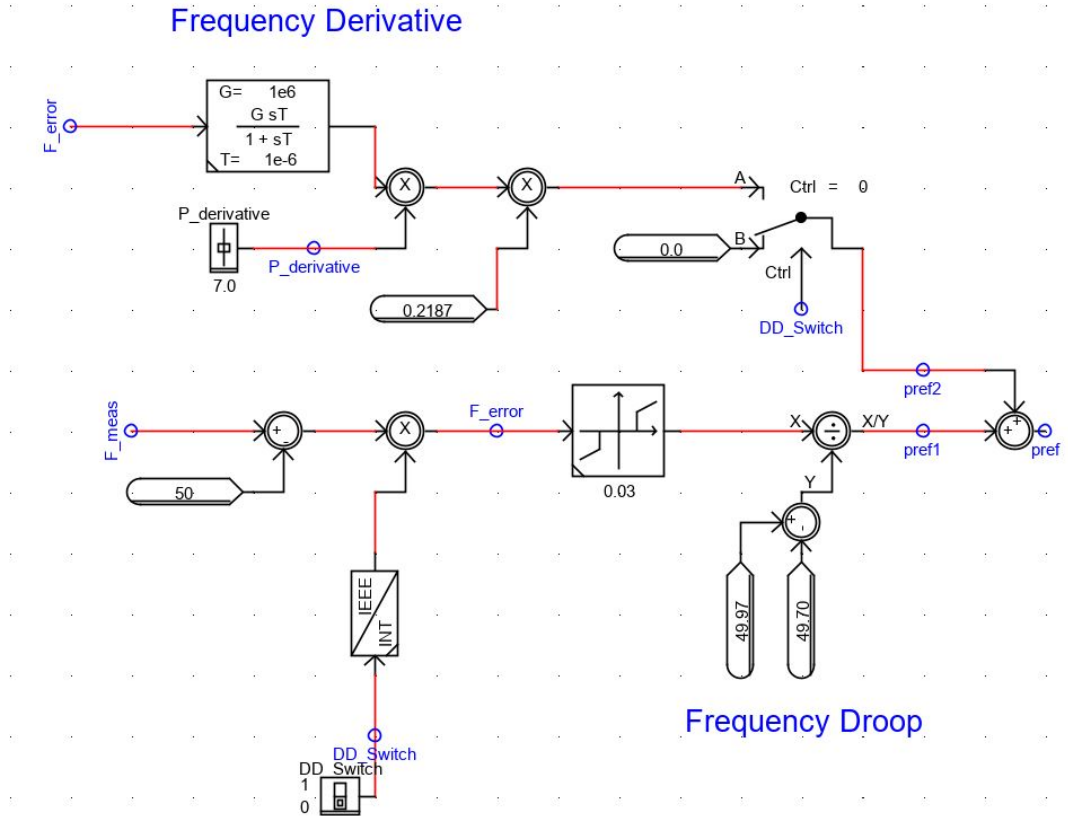
FDWGs are considered as one converter decoupled RES in this thesis. The HESS can also be installed on DC-link of other types of RES like solar panels. Besides, the power generation of these RES can change in different operational condition, hence the changing power flows may influence the power demands of frequency stability control. The grid-side converter should also be designed according to the application of HESS. The power reserve of grid-side converters should be able to supply the power demands of frequency stability control. [38]



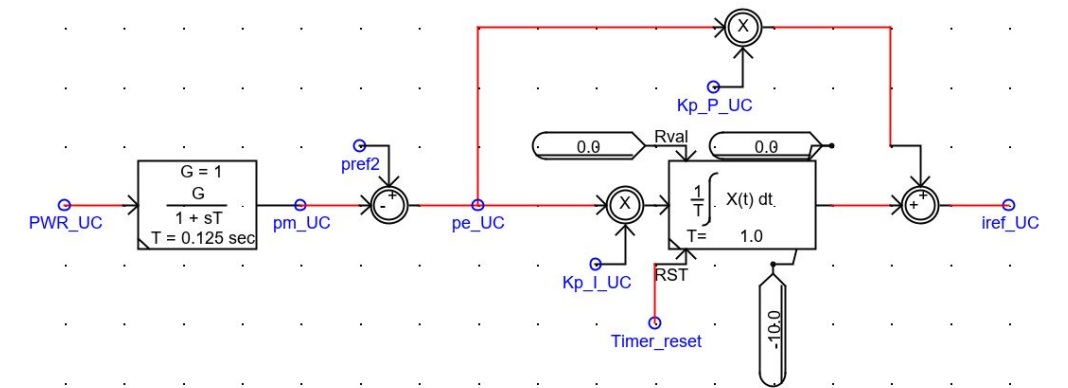
Control Loops in RSCAD

A.1. Droop and Derivative Controllers in RSCAD

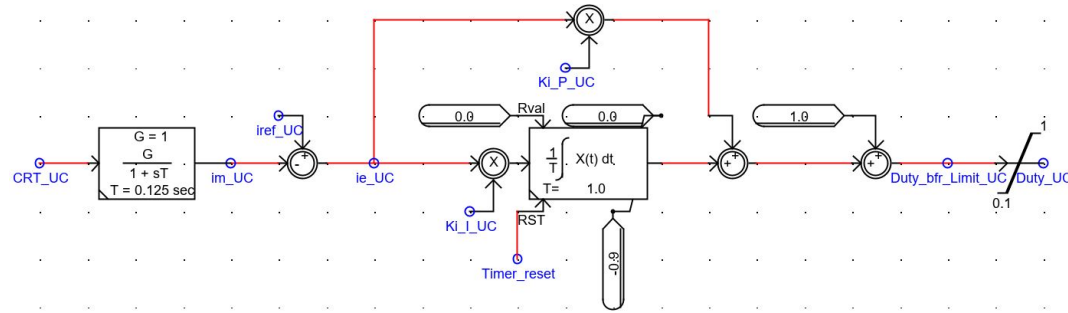
Figure A.1 shows the droop and derivative controllers implemented in RSCAD environment, which is based on previous block diagrams. In (a), the frequency measurement F_{meas} comes from the output of a power measurement unit. A gain 0.2187 used to transfer system inertia to the virtual inertia of UCs at a FDWG. Signal DD_Switch switching on droop and derivative control mode. The frequency droop is set by using frequency drop of 1MW. A dead band blocks disturbance. The outer power controller and inner current controller are both PI controllers. The integral blocks are defined in an anti-windup mode.



(a)



(b)



(c)

Figure A.1: (a) Droop and derivative controller, (b) Outer power controller, (c) Inner current controller.

A.2. VSP Controllers in RSCAD

Figure A.2, shows the VSP implemented in RSCAD. The power difference is generated by deducting the measured RES generation and delivered power flow. A dead-band is used to block the disturbance of power measurement. A high-pass filter is used to allocate the total power difference to UCs and batteries. The cut-off frequency T_{HPF} is a variable parameter which needs to be optimized. Two separate second-order control loops are used to generate the duty cycle for DC-DC converters. Both controllers have variable natural frequency ω_n and damp factors ζ . Limiters are used to avoid invalid output of duty cycle.

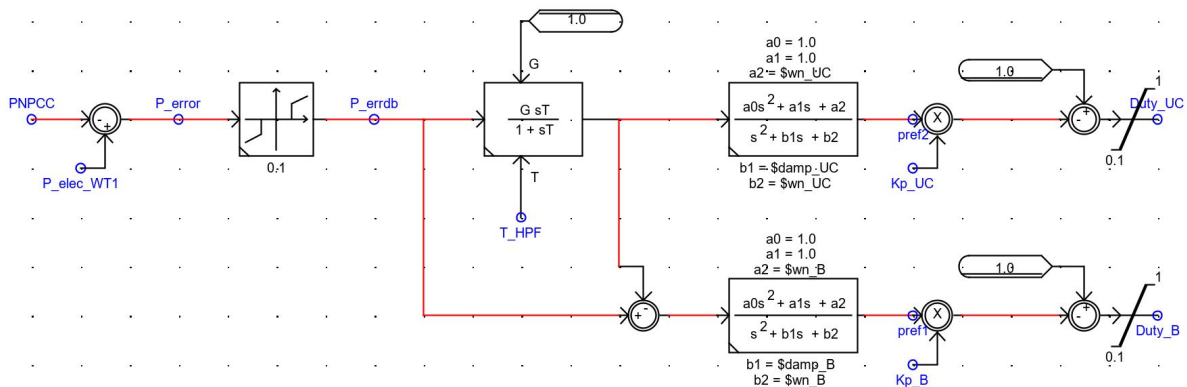


Figure A.2: VSP controllers in RSCAD

A.3. RSCAD Embedded Li-ion Battery Model

The structure of Li-ion model in RSCAD (`_rtds_libat.def`) is shown in figure A.3. This Li-ion battery model is simulated with UC model to represent the HESS. Equation A.1 shows the parameter setting of the battery model [4].

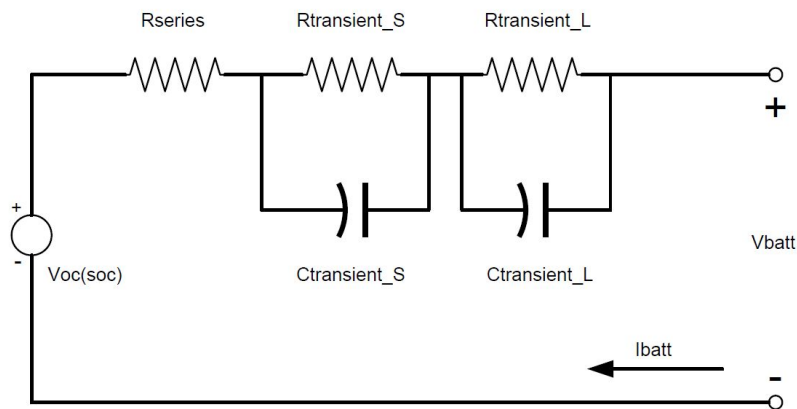


Figure A.3: RSCAD embedded Li-ion battery model [4]

$$\begin{aligned}V_{OC}(SOC) &= -1.031 \cdot e^{-35 \cdot SOC} + 3.685 + 0.2156 \cdot SOC - 0.1178 \cdot SOC^2 + 0.3201 \cdot SOC^3 \\R_{Series}(SOC) &= 0.1562 \cdot e^{-24.37 \cdot SOC} + 0.07446 \\R_{Transient_S}(SOC) &= 0.3208 \cdot e^{-29.14 \cdot SOC} + 0.04669 \\C_{Transient_S}(SOC) &= -752.9 \cdot SOC + 703.6 \\R_{Transient_L}(SOC) &= 6.603 \cdot e^{-155.2 \cdot SOC} + 0.04984 \\C_{Transient_L}(SOC) &= -6056 \cdot e^{-27.12 \cdot SOC} + 4475\end{aligned}\tag{A.1}$$

Bibliography

- [1] Elyas Rakhshani and Pedro Rodriguez. Inertia emulation in ac/dc interconnected power systems using derivative technique considering frequency measurement effects. *IEEE Transactions on Power Systems*, 32(5):3338–3351, 2016.
- [2] Stanley Atcity. *Electrochemical capacitor characterization for electric utility applications*. PhD thesis, Virginia Tech, 2006.
- [3] Nidarshan Veera Kumar. Real-time simulation based analysis of fast active power regulation strategies to enhance frequency support from pe interfaced multi-energy system. 2019.
- [4] RTDS Technologies. In *RTDS Manuals and Documentation*, 2012.
- [5] Samir M Alhejaj and Francisco M Gonzalez-Longatt. Investigation on grid-scale bess providing inertial response support. In *2016 IEEE International Conference on Power System Technology (POWERCON)*, pages 1–6. IEEE, 2016.
- [6] Jiebei Zhu, Jiabing Hu, William Hung, Chengshan Wang, Xin Zhang, Siqi Bu, Qi Li, Helge Urdal, and Campbell David Booth. Synthetic inertia control strategy for doubly fed induction generator wind turbine generators using lithium-ion supercapacitors. *IEEE Transactions on Energy Conversion*, 33(2):773–783, 2017.
- [7] I Egado, L Sigrist, E Lobato, L Rouco, and A Barrado. An ultra-capacitor for frequency stability enhancement in small-isolated power systems: Models, simulation and field tests. *Applied Energy*, 137:670–676, 2015.
- [8] Abbas A Akhil, Georgianne Huff, Aileen B Currier, Benjamin C Kaun, Dan M Rastler, Stella Bingqing Chen, Andrew L Cotter, Dale T Bradshaw, and William D Gauntlett. *DOE/EPRI 2013 electricity storage handbook in collaboration with NRECA*. Sandia National Laboratories Albuquerque, NM, 2013.
- [9] Xiang Hao, Tianpei Zhou, Jin Wang, and Xu Yang. A hybrid adaptive fuzzy control strategy for dfig-based wind turbines with super-capacitor energy storage to realize short-term grid frequency support. In *2015 IEEE Energy Conversion Congress and Exposition (ECCE)*, pages 1914–1918. IEEE, 2015.
- [10] Ujjwol Tamrakar, Dipesh Shrestha, Manisha Maharjan, Bishnu P Bhattarai, Timothy M Hansen, and Reinaldo Tonkoski. Virtual inertia: Current trends and future directions. *Applied Sciences*, 7(7):654, 2017.
- [11] Jingyang Fang, Yi Tang, Hongchang Li, and Xiaoqiang Li. A battery/ultracapacitor hybrid energy storage system for implementing the power management of virtual synchronous generators. *IEEE Transactions on Power Electronics*, 33(4):2820–2824, 2017.

- [12] MPN Van Wesenbeeck, SWH De Haan, Pablo Varela, and Klaas Visscher. Grid tied converter with virtual kinetic storage. In *2009 IEEE Bucharest PowerTech*, pages 1–7. IEEE, 2009.
- [13] Elyas Rakhshani, Daniel Remon, Antoni Mir Cantarellas, Jorge Martinez Garcia, and Pedro Rodriguez. Virtual synchronous power strategy for multiple hvdc interconnections of multi-area ac power systems. *IEEE Transactions on Power Systems*, 32(3):1665–1677, 2016.
- [14] Joan Rocabert, Ruben Capó-Misut, Raúl Santiago Muñoz-Aguilar, José Ignacio Candela, and Pedro Rodriguez. Control of energy storage system integrating electrochemical batteries and supercapacitors for grid-connected applications. *IEEE Transactions on Industry Applications*, 55(2):1853–1862, 2018.
- [15] Ioan Serban, Remus Teodorescu, and Corneliu Marinescu. Energy storage systems impact on the short-term frequency stability of distributed autonomous microgrids, an analysis using aggregate models. *IET Renewable Power Generation*, 7(5):531–539, 2013.
- [16] Vladimir Yuhimenko, Chaim Lerman, and Alon Kuperman. Dc active power filter-based hybrid energy source for pulsed power loads. *IEEE Journal of Emerging and Selected Topics in Power Electronics*, 3(4):1001–1010, 2015.
- [17] Masoud Hajiakbari Fini and Mohamad Esmail Hamedani Golshan. Determining optimal virtual inertia and frequency control parameters to preserve the frequency stability in islanded microgrids with high penetration of renewables. *Electric Power Systems Research*, 154:13–22, 2018.
- [18] Netra Gyawali and Yasuharu Ohsawa. Effective voltage and frequency control strategy for a stand-alone system with induction generator/fuel cell/ultracapacitor. In *2009 CIGRE/IEEE PES Joint Symposium Integration of Wide-Scale Renewable Resources Into the Power Delivery System*, pages 1–11. IEEE, 2009.
- [19] Chen Zhao, He Yin, and Chengbin Ma. Equivalent series resistance-based real-time control of battery-ultracapacitor hybrid energy storage systems. *IEEE Transactions on Industrial Electronics*, 67(3):1999–2008, 2019.
- [20] Lisheng Shi and ML Crow. Comparison of ultracapacitor electric circuit models. In *2008 IEEE Power and Energy Society General Meeting-Conversion and Delivery of Electrical Energy in the 21st Century*, pages 1–6. IEEE, 2008.
- [21] Andrew Nadeau, Moeen Hassanali, Gaurav Sharma, and Tolga Soyata. Energy awareness for supercapacitors using kalman filter state-of-charge tracking. *Journal of Power Sources*, 296:383–391, 2015.
- [22] Yang Wang, Joan E Carletta, Tom T Hartley, and Robert J Veillette. An ultracapacitor model derived using time-dependent current profiles. In *2008 51st Midwest Symposium on Circuits and Systems*, pages 726–729. IEEE, 2008.
- [23] Chia-Jui Chiang, Jing-Long Yang, and Wen-Chin Cheng. Temperature and state-of-charge estimation in ultracapacitors based on extended kalman filter. *Journal of Power Sources*, 234:234–243, 2013.

- [24] Stephan Buller, E Karden, D Kok, and RW De Doncker. Modeling the dynamic behavior of supercapacitors using impedance spectroscopy. *IEEE transactions on Industry Applications*, 38(6):1622–1626, 2002.
- [25] Lei Zhang, Xiaosong Hu, Zhenpo Wang, Fengchun Sun, and David G Dorrell. Fractional-order modeling and state-of-charge estimation for ultracapacitors. *Journal of Power Sources*, 314:28–34, 2016.
- [26] Luis Zubieta and Richard Bonert. Characterization of double-layer capacitors for power electronics applications. *IEEE Transactions on industry applications*, 36(1):199–205, 2000.
- [27] Petar J Grbović, Philippe Delarue, and Philippe Le Moigne. Modeling and control of ultra-capacitor based energy storage and power conversion system. In *2014 IEEE 15th Workshop on Control and Modeling for Power Electronics (COMPEL)*, pages 1–9. IEEE, 2014.
- [28] Eckhard Karden. *Using Low Frequency Impedance Spectroscopy for Characterization, Monitoring, and Modeling of Industrial Batteries*. PhD thesis, Verlag nicht ermittelbar, 2001.
- [29] Lei Zhang, Xiaosong Hu, Zhenpo Wang, Fengchun Sun, and David G Dorrell. A review of supercapacitor modeling, estimation, and applications: A control/management perspective. *Renewable and Sustainable Energy Reviews*, 81:1868–1878, 2018.
- [30] Ahmed S Elwakil. Fractional-order circuits and systems: An emerging interdisciplinary research area. *IEEE Circuits and Systems Magazine*, 10(4):40–50, 2010.
- [31] Branislav Hredzak, Vassilios G Agelidis, and Georgios D Demetriades. A low complexity control system for a hybrid dc power source based on ultracapacitor–lead–acid battery configuration. *IEEE transactions on Power Electronics*, 29(6):2882–2891, 2013.
- [32] CF Ten and PA Crossley. Evaluation of rocof relay performances on networks with distributed generation. 2008.
- [33] Ian Mathews, Bolun Xu, Wei He, Vanessa Barreto, Tonio Buonassisi, and Ian Marius Peters. Techno-economic model of a second-life energy storage system for utility-scale solar power considering li-ion calendar and cycle aging. *arXiv preprint arXiv:2003.03216*, 2020.
- [34] Vaclav Knap, Rakesh Sinha, Maciej Swierczynski, Daniel-Ioan Stroe, and Sanjay Chaudhary. Grid inertial response with lithium-ion battery energy storage systems. In *2014 IEEE 23rd International Symposium on Industrial Electronics (ISIE)*, pages 1817–1822. IEEE, 2014.
- [35] Müfit Altin, Remus Teodorescu, BB Jensen, UD Annakkage, Florin Iov, and PC Kjaer. Methodology for assessment of inertial response from wind power plants. In *2012 IEEE Power and Energy Society General Meeting*, pages 1–8. IEEE, 2012.
- [36] Damith Buddika Wickramasinghe Abeywardana, Branislav Hredzak, Vassilios G Agelidis, and Georgios D Demetriades. Supercapacitor sizing method for energy-controlled filter-based hybrid energy storage systems. *IEEE Transactions on Power Electronics*, 32(2):1626–1637, 2016.
- [37] Daniel Dotta, Aguinaldo S e Silva, and Ildemar C Decker. Design of power system controllers by nonsmooth, nonconvex optimization. In *2009 IEEE Power & Energy Society General Meeting*, pages 1–7. IEEE, 2009.

-
- [38] István Erlich, Ganesh K Venayagamoorthy, and Nakawiro Worawat. A mean-variance optimization algorithm. In *IEEE Congress on Evolutionary Computation*, pages 1–6. IEEE, 2010.